THE UNIVERSITY OF READING
DEPARTMENT OF MATHEMATICS

Numerical Methods For Macroscopic Traffic Models

by

Joanne V. Morgan

Thesis submitted for the degree of
Doctor of Philosophy

August 2002

Declaration: I confirm that this is my own work and the use of all material from other sources has been properly and fully acknowledged.

Joanne Morgan

August 29, 2002

Acknowledgements

Firstly, I would like to thank the Highways Agency, in particular Brian Harbord from TSS division for the data analysed in this thesis, provided through Jo White from TRL. My thanks also go to the E.P.S.R.C. for supporting this research and to all drivers everywhere.

I would like to thank Jo White on a personal level for her help, discussions and encouragement. My thanks also go to Eddie Wilson for sharing his enthusiasm for the subject.

My apologies go out to all my friends and family whom I've shamelessly neglected these last few months and yet have still been there to keep me relatively sane. Of these I would especially like to thank Pete for letting me win at pool now and again, Kev for his generous offer, Marek for his inflammatory yet delicious cooking and for always listening, Jayne for always being there, my sister Sue for having the ability to make me laugh no matter how evil I'm being and Ray for putting up with me. I couldn't have asked for a better roomie or friend. Extra special thanks go to Louise for so many things particularly my sanity. Big hugs to everyone else too numerous to mention but still very much appreciated.

I'd like to thank Sue Davis from the Maths department for knowing the right thing to say (and when) and Dave Porter for his encouragement.

Finally, I guess I should mention my supervisors Mike Baines and Pete Sweby. I would like to thank you both for not letting me know what I was getting into until it was too late. Thanks for believing in me and making it such an enjoyable four years. Thanks to Mike for giving me the chance in the first place.

This thesis is for you mum.

No, I'm not a professor just yet!

Abstract

In this thesis a number of macroscopic models and numerical methods are considered for simulating the flow of vehicular traffic on a single lane highway. The results are compared with averaged real data obtained from the Highways Agency via TRL.

The original one-equation model requires a velocity-density function which was obtained by fitting a curve through the data. The resulting model is a conservation of mass equation with a non-convex flux function. Two test cases are considered which resemble a simplified cluster of traffic in an otherwise free flowing highway. Analytic solutions are found and compared to the numerical solutions obtained from applying four state-of-the-art numerical shock capturing schemes. The second order scheme with a flux limiter produced the best results.

Four two-equation models are also considered. A Riemann test problem is used to test three of the models and to compare with the numerical solutions obtained using the same second order scheme with a flux limiter. For each of these models a Roe decomposition is constructed which gives approximate wave descriptions of the models. Special procedures, using real data, are proposed for overcoming the difficulties encountered when dealing with the boundaries. The effects of adding non homogeneous terms to these models are also investigated.

The real data provides initial conditions and boundary data which are used for numerical simulations with the five models. These are compared to the real data at a later time. No clear winner is found but the models provide useful insights into the mechanisms at work.

Contents

Chapter 1

Introduction

Interest in modelling traffic flow has been around since the appearance of traffic jams. The idea of modelling is that, if you can correctly predict the behaviour of vehicular flow given an initial set of data then in theory by adjusting the flow in crucial areas the overall throughput of traffic along a stretch of road can be maximised. This is of particular interest in regions of high density, which may be caused by high volume peak time traffic or even as a result of an accident or blockage of one or more lanes of the carriageway. It is one of the aims of the variable speed limit signs on the M25 motorway. These are mounted on regularly spaced posts that measure certain features of the traffic, so that the overhead speed limit signs may be adjusted to improve conditions. However, in order to achieve these goals we first need a good model of traffic flow and reliable numerical methods for solving the equations. This thesis aims to survey existing models and apply state-of-the-art numerical techniques for their solution.

Chapter 2 is an introduction to some of the different models that have been suggested. There are two main approaches to modelling. One way is to consider each individual vehicle and express its behaviour by a set of rules or an equation involving adjacent vehicles. These are referred to as microscopic models. Another approach (the one considered in this thesis) is to consider the overall average behaviour of traffic and treat the road as a series of sections (small compared to the total length of the road) within each of which the density and average velocity of traffic can be measured for a given time. The changes in these variables (for example) may then be described using

partial differential equations. These models are referred to as macroscopic models and form the basis of this study.

In Chapter 3 we look at data from the M25 motorway which was made available to us from the Highways Agency via TRL. We describe how the raw data is averaged into a format suitable for use with the models (since the models we consider describe only single lane carriageways with no on or off ramps). In this chapter we also look at the relationship between the velocity and density of the flow, and also between the flux and density which are crucial functions present in many of the models studied here. The latter is often called the *fundamental diagram* as it appears in many models and much effort has been given into fitting functions to obtain this diagram. Five such functions have been chosen for comparison. A significant feature of the fitted functions is that the flux function is non-convex. This has considerable significance in its effect on the evolution of the density.

In Chapter 4 we consider the classical Lighthill-Whitham-Richards model (LWR), which consists of a single conservation of mass equation with a prescribed velocity-density relationship. We derive analytic solutions obtained from this model for two test problems when a generic non-convex flux function is used. The test cases were chosen as simplifications of real flows where a platoon, or high density region of vehicles, is travelling within otherwise free flowing traffic. The aim of this chapter is to give insight into the behaviour of traffic using this model, which is still surprisingly competitive.

Since the appearance of the LWR model several other models have appeared involving two equations in which the velocity is now independent of the density. In Chapter 5 we discuss four models of this kind that have been proposed. Firstly the Payne-Whitham model which is inspired by the similarities between traffic flow and fluid dynamics. This is a much studied model, and many variations to it have been suggested. One such variation is the recent Berg-Mason-Woods model, also investigated here, which has been derived from a microscopic car-following model. A criticism of these fluid-like models is the problem of anisotropic behaviour of drivers. Hence the next model studied, by Aw and Rascle, has moved away completely from fluid flow and they suggest a model which would be more traffic-like. Zhang, again moving away from fluids, proposed a model derived from microscopic principles and is the final

model in this study. Analytic solutions to a Riemann test problem are found to three of the models and compared to analytic solutions in this section.

Chapter 6 describes four numerical schemes used with the one-equation model. These are shock-capturing entropy satisfying finite difference schemes. The numerical results of the schemes are compared for the test problems in Chapter 4 and the best scheme chosen, which was the second order scheme with a flux limiter.

The treatment of systems of equations is a little more involved, hence Chapter 7 describes two different schemes. The first is Lax-Friedrichs which is cheap and easy to implement and is therefore useful for giving a rough idea of the behaviour. It is very diffusive however, hence for a more accurate solution more sophisticated schemes are required. We therefore also construct a Roe decomposition for each model and then apply the second order upwind scheme with a flux limiter. Characteristic Variables are required at the boundaries when the two component waves of any system are travelling in opposite directions there, hence this chapter also presents the Characteristic Variables for the models in Chapter 5. Due to the complex nature of the Berg-Mason-Woods Characteristic Variables an alternative approach at the boundaries is described.

In order to see how realistic these models are, we use in Chapter 8 the real data as initial conditions and boundary data where required for each of the five models. Firstly the results from the different velocity functions with the Lighthill-Whitham-Richards model are compared and the best one chosen. This is then compared to the results from the four other models. A second set of initial data is chosen for study from a different day and time, and the results from all models compared to verify these are typical results from the models.

In Chapter 9 we investigate the effects of the non-homogeneous terms of the two-equation models. Some models suggest the inclusion of a relaxation term in order to mimic the adjustment of drivers' velocity towards a maximal desired safe velocity. This term has the effect of speeding up vehicles that are currently driving slower than they would like, and slowing down vehicles travelling faster than they should be. Another type of source term suggested are viscosity terms in the form of second spatial derivatives of either density or velocity. These terms have the effect of smoothing out

sharp changes in the variables. We discuss the implementation of these source terms, their benefits and their drawbacks.

Finally, in Chapter 10 we discuss the findings of this study and suggest further work.

Chapter 2

Background

This chapter contains a review of the existing state of mathematical and numerical modelling of single lane traffic flow.

Interest in modelling traffic flow began around the 1950's with one of the first papers to discuss the problem being [23], written by Lighthill and Whitham. These authors wrote two important papers at that time on *Kinematic Waves*, the first on *Flood Movement in Long Rivers* and the second *A Theory of Traffic Flow on Long Crowded Roads*, the papers drawing similarities between the two types of flow. A similar discussion on traffic flow was published by Richards around the same time, [29], independently of Lighthill and Whitham. The common mathematical model is referred to as the LWR model. Its basic principle is the one-dimensional conservation equation,

$$\rho_t + (\rho v)_x = 0, \tag{2.1}$$

where $\rho(x,t)$ is the density (in number of vehicles per km at time t for example), and v is the velocity (in km per hour). This states that vehicles do not appear or disappear, therefore the number of vehicles will depend only on the number already present in the system and the flow of vehicles into and out of the system. The assumption was then made that the velocity is a linearly decreasing function of the density of the traffic, e.g.,

$$v = V(\rho) = v_{max}\left(1 - \frac{\rho}{\rho_{max}}\right), \tag{2.2}$$

where v_{max} is some maximal velocity of the road and ρ_{max} is the maximal bumper to bumper density. The flux diagram, or $\rho V(\rho)$ plotted against ρ, is often referred to as

the *Fundamental Diagram* as it is an integral part of many traffic flow models.

The LWR model, consisting of (2.1) and (2.2), is an example of a non-linear first order partial differential equation. More specifically it is a hyperbolic conservation law where *mass*, in this case *density* of traffic, is conserved. This means that although the distribution of vehicles will vary with time, the overall amount of traffic in the system will depend on the *flux*, or flow, into and out of the domain. Here the flux function is given by $\rho V(\rho)$ and can be considered as the momentum of the flow. One property of this type of equation is that given smooth initial data there is the possibility of spontaneous generation of shocks, i.e. a discontinuity in the density (and velocity) in space. This is an example of a weak solution since the partial differential equation only holds for continuous solutions. Another type of wave possible from a discontinuity is a contact discontinuity where again there is a jump in the density, but the velocity is constant across it. A third type of wave is a rarefraction fan where, for example, a discontinuity in the density spreads out in time giving a smooth transition between the left and right states. Since the wavespeeds are real and finite for a well posed problem, initial data is required, indeed the solution at a later time t depends on this initial data. Boundary conditions are also required on a bounded spatial domain when the waves are moving away from the boundaries and into the domain, as we will see later (Chapter 4). We will also be considering systems of two equations of hyperbolic conservation laws, which means that the eigenvalues of the flux jacobian matrix, $\mathbf{f}'(\mathbf{u})$, are real and there are two linearly independent eigenvectors, hence the matrix is invertible.

In the case of shocks Zhang, [38], describes the behaviour of the LWR model for Riemann initial conditions. When the traffic concentration is heavy downstream and light upstream a shockwave forms and travels at speed given by the Rankine-Hugoniot jump condition

$$s = \frac{[f(\rho)]}{[\rho]} = \frac{f(\rho_L) - f(\rho_R)}{\rho_L - \rho_R},$$

where ρ_L and ρ_R are the traffic concentrations upstream and downstream of the shock respectively, as would be experienced by drivers approaching a jam or region of high density. When the concentration is light downstream and heavy upstream a rarefaction wave arises and the heavy traffic disperses, just as would be observed in traffic queued

at a traffic light when the light turns green.

This model does however have some drawbacks, as discussed in [5] and [13] for example, due to the assumption that the traffic is in "equilibrium", i.e. given a particular density the velocity will be a fixed value. The model is therefore unable to describe observed behaviour at *ramps* and *bottlenecks* or the self organisation of *stop-and-go* waves, nor does it recognise a spread of acceptable velocities for a given density by drivers, [13]. The model also doesn't allow a *platoon* of vehicles (a cluster of vehicles in otherwise low density traffic) to disperse from the front and the rear in a manner observed in reality, [5]. Nevertheless the LWR model agrees fairly well with predictions from *car-following models* (discussed in the section below on microscopic models) and with some adjustment to the velocity function this turns out to be a robust model.

The LWR model is an example of a *macroscopic model*. This type of model is concerned only with average behaviour on a large scale. A second class of models also exists based on individual vehicle behaviour and are thus referred to as *microscopic* models.

In this thesis we are concerned with macroscopic models. The LWR model is discussed in more detail in Chapters 4, 6 and 8. However, for completeness we begin with a discussion of microscopic models.

2.1 Microscopic Models

This type of model concentrates on the behaviour of each individual vehicle. The driver will adjust his or her velocity and acceleration according to the conditions ahead. These models are often called *Car-Following* models. Holland [15] describes this approach as providing a natural way to model traffic. In these models each vehicle is influenced directly by the one in front, as often happens in real traffic flow. Thus, vehicle position is treated as a continuous function and each vehicle moves according to an ordinary differential equation normally dependent on its speed and the distance to the next vehicle. The vehicle's progress can be calculated by solving these ordinary differential equations simultaneously. Usually the number of vehicles to be modelled has to be small enough for the approach to be useful. This situation

sets traffic modelling apart from other fields, for example fluid mechanics and granular flow, because in these subjects the number of particles to be considered is typically too great for microscopic modelling. We can therefore consider car-following models as an alternative to a continuum approach. There are a number of different assumptions made for the various models of this type about what factors affect drivers' decisions to change their behaviour, such as the *headway*, which is defined as the distance in front of a vehicle before the next vehicle, (see e.g. [26]). To make the model more realistic [26] also incorporates a time lag of the drivers' responses. Bando, in [2] made the alternative assumption that drivers wish to drive at a *legal velocity* which is a function of the headway, therefore their acceleration will be governed by the difference between the vehicle's velocity and this maximal safe velocity.

Chandler *et al.* [4] suggested the first important model of this type. This took the form

$$\ddot{x}_n(t+T) = \lambda(\dot{x}_{n+1} - \dot{x}_n),$$

where x_n represents the position of the nth vehicle, which follows vehicle $n+1$, and $\ddot{x}$ is the second time derivative, i.e. acceleration. They then incorporated into the model the California Code that states that a good rule for following another vehicle at a safe distance is to allow one length of a car (about 15 feet) for every ten miles per hour you are travelling. They therefore suggested an alternative law stating

$$\ddot{x}_n(t+T) = \lambda(x_{n+1} - x_n - c - T_1\dot{x}_n),$$

where T is the time delay, λ a sensitivity parameter, c the average length of a vehicle and T_1 the time headway given by the California Code.

Numerous alternative models have since been proposed, e.g. Newell [26] used the velocity-headway function alone to describe the dynamics of the flow. He proposed the law

$$\dot{x}_n(t+T) = V\left(1 - exp\left(-\frac{\lambda}{V}(x_{n+1} - x_n) - d\right)\right),$$

where again T is a time delay, V is a maximal velocity and λ, d are constants. More recently Bando *et al.*, [2] has suggested the law

$$\ddot{x}_n = a(V(x_{n+1} - x_n) - \dot{x}_n), \tag{2.3}$$

where a is an acceleration constant and $V(b)$ a velocity-headway function given by

$$V(b) = tanh(b-2) + tanh(2),$$

$b = x_{n+1} - x_n$ representing the headway.

Nagel, [25], summarised car-following models by noting that many such models are of the form

$$a(t+T) \propto \frac{v(t)^m}{[\Delta x(t)]^l} \Delta v(t),$$

where a and v are the acceleration and velocity, respectively of the car under consideration, Δx is the distance to the car ahead, Δv is the velocity difference to that car, and m and l are constants. T is a delay time between stimulus and response, which summarises all delay effects such as human reaction time.

Nagel, [25], then described a new model that he referred to as *Particle Hopping*, which differs from car-following in that it is a fully discrete model. It considers the road as being represented as a string of cells which are either empty or occupied by exactly one particle. Movement takes place by hopping between cells, and can only take place in one direction. These cells are then updated simultaneously. The number N of particles in the system is conserved, except at the boundaries. This type of model belongs to a group of models known as *Cellular Automata*, or CA. An example is the *Stochastic Traffic Cellular Automaton*, or STCA model, as quoted in [25], which is defined as follows. Each particle (car) can have an integer velocity between 0 and v_{max}. The complete configuration at time step t is stored and the configuration at time step $t+1$ is computed from that, using a parallel or synchronous update. All cars execute the following steps.

(i). Let g (gap) equal the number of empty sites ahead.

(ii). If $v > g$ (too fast), then slow down to $v := g$ (rule 1); otherwise if ($v < g$) (enough headway) *and* $v < v_{max}$, then accelerate by one: $v := v + 1$ (rule 2).

(iii). Randomization: If after the above steps the velocity is larger than zero ($v > 0$), then, with probability p, reduce v by one (rule 3).

(iv). Particle propagation: Each particle moves v sites ahead (rule 4).

Nagel also notes that the randomization incorporates three different properties of human driving into one computational operation: fluctuations at maximum speed, overreactions at breaking, and retarded (noisy) acceleration.

A *Cruise Control* limit version was then suggested by Nagel, [24], whereby fluctuations at free driving, i.e., at maximum speed and undisturbed by other drivers, are set to zero. Algorithmically, the velocity update (rules 1-3) of the STCA are replaced by the following. For all cars, do the following simultaneously:

(i). A vehicle travelling at maximum velocity v_{max} with free headway $g > v_{max}$ just maintains its velocity.

(ii). Otherwise the standard rules 1-3 of the STCA are applied.

Nagel noted that both acceleration and braking still have a stochastic component in this STCA-CC model.

By setting the randomization probability p equal to zero, which just amounts to skipping the randomization step, the deterministic limit of the STCA is taken, and is referred to as the CA-184 model when $v_{max} = 1$. Various authors have considered this model, and also with $v_{max} > 1$, with much work in this field being based on this approach. Two dimensional CA models for traffic also incorporate these ideas.

According to Nagel, the most-investigated particle hopping model is the asymmetric stochastic exclusion process (ASEP). Its behaviour is defined as follows:

(i). Pick one particle randomly (rule 1).

(ii). If the site to the right is free, move the particle to that site (rule 2).

On average, therefore, each particle is updated once after N single-particle updates, and a time step is completed after N attempted hops.

As demonstrated in [19], Nagel states that it can be shown that the classic ASEP corresponds to the noisy Burgers' equation. This means that by taking the limit of the particle process a continuous model is obtained which is given by

$$\rho_t + (\rho(1-\rho))_x = D\rho_{xx} + \eta,$$

where D is the diffusion coefficient and η is a Gaussian noise term. This is equvalent to the LWR model with noise and diffusion. Hence LWR (with noise and diffusion)

and ASEP particle hopping process describe the *same* behaviour. The CA-184 model, however, corresponds to the nondiffusive, non-noisy equation of continuity

$$\rho_t + j'\rho_x = 0,$$

with the linear flow (except at $\rho = \rho_{j_{max}}$)

$$j' = \frac{dj}{d\rho} = \begin{cases} v_{max} \text{ for } \rho < \rho_{j_{max}} \\ -1 \text{ for } \rho > \rho_{j_{max}}. \end{cases} \tag{2.4}$$

The intersection point of the fundamental diagram obtained from (2.4) divides two phenomenological regimes: light traffic ($\rho < \rho_{j_{max}}$) and dense traffic ($\rho > \rho_{j_{max}}$).

However, microscopic methods are computationally expensive, as each vehicle has a differential equation to be solved at each time step governing its behaviour, so as the number of vehicles increases so does the size of the (coupled) system. Macroscopic models are therefore preferable if a suitable equation or system which satisfactorily describes the flow can be found. In this thesis we concentrate solely on macroscopic models.

2.2 Macroscopic Models

Due to the simplistic nature of the LWR model ((2.1),(2.2)) it is unable to capture all of the complex interactions desirable for a realistic traffic flow model. For this reason modifications to the LWR model have been suggested. The conservation equation itself (2.1) is the basis for all subsequent models,

$$\rho_t + (\rho v)_x = 0, \tag{2.5}$$

with velocity v now independent of ρ, i.e. the flow is no longer in equilibrium. Modifications attempting to improve on the failings of the LWR model haven't always been successful. Most adaptations involve coupling the conservation equation with a second equation that attempts to mimic traffic more convincingly. Payne and Whitham [36] continued the discussion on the basis that traffic was rather like a fluid and coupled the continuity equation with a variation to the Navier-Stokes equation of motion for

an incompressible flow, with the addition of a *traffic-like* relaxation term $\frac{V(\rho)-v}{\tau}$. This PW model is given (in non-conservative) form by (2.5) and

$$v_t + vv_x = \frac{V(\rho) - v}{\tau} - \frac{C(\rho)}{\rho}\rho_x, \tag{2.6}$$

where τ is the relaxation time and $V(\rho)$ is a velocity function, e.g. (2.2). $C(\rho)$ is an *anticipation term*, which Payne [27] suggested should be of the form $C(\rho) = \frac{\partial}{\partial\rho}(\rho\Theta(\rho))$. Later Kühne [20] proposed $\Theta(\rho) = C_o^2$ and included a *viscosity term* μv_{xx} to smooth out sudden density and velocity changes deemed unrealistic. The PW momentum equation is typical of higher-order models in that it has a relaxation term that contains the equilibrium speed-concentration relation and an anticipation term that contains the space gradient of the vehicle concentration. This model has been studied at length, see e.g. [12, 40], and variations to it made in an attempt to tune it to traffic flow. Kerner and Konhäuser (KK) for example, [16, 17, 18], used Kühne's variations but altered the viscosity term to make it compatible with the Navier-Stokes equations to give

$$v_t + vv_x = \frac{V(\rho) - v}{\tau} - \frac{C_o^2}{\rho}\rho_x + \mu\frac{v_{xx}}{\rho}, \tag{2.7}$$

with μ the viscosity or dissipative constant. They demonstrated the spontaneous appearance of clusters forming in densities above a critical value.

One criticism of the PW model is that under certain conditions it allows vehicles to move with negative velocity, i.e. against the flow of the traffic. Numerous choices of $C(\rho)$ have been proposed to alleviate this but these PW-type models have been heavily criticised for sticking too closely to fluid flow, and for not allowing for the major differences between the two types of medium, see e.g. [1, 5]. The main difference is identified as the anisotropic nature of traffic compared to fluids. Aw and Rascle [1] describe this as follows:

> "A fluid particle responds to stimuli from the front and from behind, but a car is an anisotropic particle that mostly responds to frontal stimuli."

In fact the motion of fluids is governed by the motion of particles all around a given particle, whereas traffic *particles* or vehicles are affected mainly by the vehicles in front, and how much headway there is when considering single lane traffic. The PW

and PW-type models, however, contain wave propagation speeds given by

$$\lambda_1 = v + C(\rho), \quad \lambda_2 = v - C(\rho),$$

one of which will always be greater than v the velocity of the traffic, therefore the model allows information to travel faster than the flow of traffic. Thus the behaviour of vehicles is too strongly dictated by the behaviour behind it, therefore contradicting the anisotropic nature observed in traffic flow. It is interesting to note that the LWR model is itself anisotropic, even though it has only one eigenvalue, since the wavespeed, given by $f'(\rho) = \rho V'(\rho) + V(\rho)$, satisfies $0 < f'(\rho) < V(\rho)$ (since $V(\rho)$ is a decreasing function).

The PW model has also been criticised for allowing unphysical flow by allowing densities greater than the bumper to bumper maximum density. Some of the major differences between vehicular flow and fluid flow that have been highlighted are (a) that the width of a shock only encompasses a few vehicles, (b) that vehicles have personalities that remain unchanged by motion and (c) that the models don't allow for the vehicles not being particles, [5]. The PW-like models are also unable to completely remove the inconsistencies with observed physical behaviour. Helbing [12] attempted to improve the model by adding a third equation analogous to the equation for thermal conduction where *heat* is represented by *velocity variance*. To further tackle some of the criticisms he then continued by incorporating various terms to allow for "finite space requirements of vehicles" and not allowing unphysical densities greater than the maximum capacity of the road. The model claims to be anisotropic and allows for the different driver styles. It does however allow waves to travel faster than the velocity v of the traffic, claiming that v is only an average value and that in reality some vehicles are travelling faster than this average velocity.

For a hyperbolic system, the eigenvalues of the Jacobian matrix are the speeds of the waves of the system. For a realistic anisotropic model therefore the fastest wave should be, at most, equal to the velocity of the flow. If it is not then the wave is moving faster than the vehicles, therefore drivers are being affected by conditions behind and the anisotropic nature of single lane motorway driving is lost.

Daganzo, [5], argued that the PW approximation to the difference-differential equations of car-following is poor since it is based on the assumption that velocity and

density are smooth. At discontinuities and sharp variations, however, the second and higher derivatives previously ignored are significant. This, Daganzo states, is one reason why the car-following model doesn't violate the physical restrictions that the density must not exceed some maximum bumper to bumper density, and that the velocity of the vehicles should always be positive.

Berg et al [3] discuss a model (BMW) that includes higher order terms derived from the Bando model, (2.3), and attempts to further bridge the gap between car-following theory and continuum models. They start by distinguishing between the quantities *headway* and *density*, commonly used in car-following and continuum models respectively. First the density ρ is usually given in car-following models by

$$\rho = \frac{1}{b}, \tag{2.8}$$

where b is the headway, i.e., the density ρ is usually defined as the inverse of headway. Berg et al state that there is a problem with this definition. For instance, suppose a set of cars are positioned at $x = 1, 2, 4, 8, ...$ The headway of the car at position x is given by $b = x$. Using formula (2.8), we obtain $\rho = \frac{1}{x}$, which is extended into the continuum domain by permitting x to take any positive, real value. According to this, the number of cars on the open interval $(1, y)$ is $\int_1^y \frac{1}{x} = log_e y$. However according to Berg et al this is consistently a factor of $log_e 2$ wrong as the actual answer is $log_2 y$ (the density between 1 and y is given by 2^n, therefore there are $n = log_2 y$ vehicles).

In the BMW model they then proceed to set up a consistent mapping between vehicle positions and the density, where $\{x_i\}$ represents the positions of the vehicles at a given instant in time, and $\rho(x)$ is the associated density function from which the positions of the vehicles can be found. To do this they require that

$$\int_{x_i}^{x_{i+1}} \rho(x)dx = 1, \tag{2.9}$$

for all i. In addition to their density function, they require the position of car 1. The mapping is not unique, given condition (2.9) only. The inverse mapping however is unique, and it is the inverse map that is used in constructing a continuum equation of motion from a car-following law. They use the definition of headway $b = x_{i+1} - x_i$ to arrive at an equation involving the continuum variable ρ by extending (2.9) to all

points along the road

$$\int_x^{x+b(x,t)} \rho(x',t)dx' = \int_0^{b(x,t)} \rho(x+y,t)dy \equiv 1.$$

The second integral can be expanded in powers of y and integrated to obtain the asymptotic series

$$b\rho + \frac{1}{2!}b^2\rho_x + \frac{1}{3!}b^3\rho_{xx} + \ldots = 1.$$

The first term corresponds to the usual definition of the density (2.8). Berg et al expanded the series to this order for two reasons. First, they wanted to obtain a continuum model that is capable of describing certain characteristic traffic parameters mentioned by Kerner and Konhäuser [17], who showed that a diffusive term has to be incorporated in the equation to do so. Second, these higher order terms are needed to maintain the same stability criterion for equilibrium flow for the continuum model as for the car-following model (see [3]).

Berg et al assume that each term is of smaller magnitude than the one preceding it, which amounts to saying that changes in the flow occur over a length scale of many vehicles.

By considering the cubic term to be much smaller than the linear and quadratic terms, the quadratic equation is solved for b obtaining

$$b \approx \frac{1}{\rho} - \frac{\rho_x}{2\rho^3}.$$

Regarding the cubic term as a perturbation, b is expanded in a perturbation series and the solution is approximated as

$$b \sim \frac{1}{\rho} - \frac{\rho_x}{2\rho^3} - \frac{\rho_{xx}}{6\rho^4} + \frac{\rho_x^2}{2\rho^5} + \ldots. \tag{2.10}$$

The first term represents the classic transformation for relating the headway and the density. The second term is similar to a *pressure term* in gas kinetics and acts to destabilize the traffic flow. If only this term is retained, then the continuum model is always unstable unlike real traffic flow. The diffusive term ρ_{xx} smoothes variations in traffic density and has a stabilizing effect on traffic flow, which counteracts the pressure term. They therefore retain terms up to this order.

Berg continues by establishing that the definition of v is consistent in both continuum and car-following models using the conservation of mass equation (2.5). With

this assumed true, equation (2.10) can then be substituted into car-following models to yield equations for ρ instead of b. The Bando model (2.3) thus gives

$$v_t + vv_x = a\left[\bar{V}(\rho) - v\right] + a\bar{V}'(\rho)\left[\frac{\rho_x}{2\rho} + \frac{\rho_{xx}}{6\rho^2} - \frac{\rho_x^2}{2\rho^3}\right] \tag{2.11}$$

and is coupled with (2.5), where

$$\bar{V}(\rho) = V_B(1/\rho),$$

$$0 < \frac{\partial V_B(b)}{\partial b}|_{b=1/\rho} = -\rho^2\frac{\partial \bar{V}(\rho)}{\partial \rho} = -\rho^2\bar{V}'(\rho).$$

Equation (2.11) is analogous to the Kerner-Konhäuser model (2.7) where $a = \frac{1}{\tau}$. However an important difference between that model and the new model (2.11) lies in the coefficients of the higher order terms. Expression (2.11) reveals that the coefficients depend on ρ, whereas the Kerner-Konhäuser model assumes them to be constant. C_o^2 is now analogous to the term $\left[-a\bar{V}'(\rho)/2\right]$. By comparison with the discrete Bando model numerical simulations show that the dependence of these coefficients on the density ρ is necessary to match the length scale and qualitative behaviour of shock wave solutions. With further terms of the asymptotic series the accuracy increases.

Nagel [25] argues that the diffusion term can be regarded as a stochasticity added high-frequency correction to density, which is supposed to be slowly varying in space and time. However, the analysis by Berg revealed that the transformation from a car-following to a continuum model also produces a diffusive or smoothing effect, without the need to introduce stochasticity.

Wilson and Berg, [37] attempt to develop a universal mathematical theory explaining the qualitative types of wave solution exhibited by optimal velocity highway traffic models. They concentrate on models using the conservation of mass equation (2.1), coupled with a second equation describing momentum, of the form

$$v_t + vv_x = \alpha\left(V(\rho) - v\right) + N\left(\rho, \rho_x, \rho_{xx}, v, v_x, v_{xx}\right), \tag{2.12}$$

where the sensitivity parameter $\alpha > 0$ and N represents anticipation and dispersive effects, and includes nontrivial dependence on at least one of the second derivatives ρ_{xx} or v_{xx}. In the paper they consider only models and parameter choices for which uniform flows are linearly stable, hence they focus on the KK version of the PW model,

(2.7) and the Berg, Mason and Woods model, (2.11), where

$$N = \begin{cases} -\beta\frac{\rho_x}{\rho} + \mu\frac{v_{xx}}{\rho}, & \text{for KK,} \\ \alpha V'(\rho)\left(\frac{\rho_x}{2\rho} - \frac{\rho_x^2}{2\rho^3} + \frac{\rho_{xx}}{6\rho^2}\right) & \text{for BMW.} \end{cases} \tag{2.13}$$

They seek travelling wave solutions of speed c and their classification, where

$$v = W(z), \quad \rho = X(z) \quad z = x - ct, \tag{2.14}$$

on an infinite road, with uniform flow conditions

$$X(\pm\infty) = \rho_\pm, \quad W(\pm\infty) = V(\rho_\pm), \tag{2.15}$$

at its ends. Equation (2.1) thus becomes $-c\frac{dX}{dz} + \frac{d(WX)}{dz} = 0$, which is integrated directly to obtain $X(W-c) = q$, where q is a constant of integration. Thus they show that

$$W = \frac{q}{X} + c. \tag{2.16}$$

The application of the boundary conditions at $z = \pm\infty$ gives $V(\rho_\pm) = q/\rho_\pm + c$, and eliminations yields

$$c = \frac{\rho_+ V(\rho_+) - \rho_- V(\rho_-)}{\rho_+ - \rho_-}, \tag{2.17}$$

and

$$q = \rho_- V(\rho_-) - c\rho_-. \tag{2.18}$$

Hence, if a wave exists, then its speed c is the gradient of the chord cutting the fundamental diagram $Q(\rho) = \rho V(\rho)$ at $(\rho_-, Q(\rho_-))$ and $(\rho_+, Q(\rho_+))$. Also q is the intercept on the $\rho = 0$ axis.

The paper then applies (2.14) to (2.12), and eliminates the velocity variable W using (2.16). The systems therefore reduce to a pair of first order ODE's, where

$$\frac{dX}{dz} = Y, \tag{2.19}$$

$$\frac{dY}{dz} = h_1(X)\left(\frac{q^2 Y}{X^3} + \frac{\alpha}{X}\left(Q(X) - (q + cX)\right)\right) + Y h_2(X, Y), \tag{2.20}$$

with the pressure and diffusion terms h_1 and h_2 being given by

$$h_1(X) = \begin{cases} \frac{X^3}{\mu q} \\ -\frac{6X^2}{\alpha V'(X)} \end{cases} \quad \text{and} \quad h_2(X, Y) = \begin{cases} -\frac{\beta X^2}{\mu q} + \frac{2Y}{X} \\ -3X + \frac{3Y}{X} \end{cases}, \tag{2.21}$$

for KK and BMW respectively. By analysing the geometrical structure of the fundamental diagram and its chords they then build up phase diagrams describing wave types.

More recently, in an attempt to incorporate the anisotropic property and move away from the fluid-type inconsistencies of previous models, Aw and Rascle [1] suggested an alternative second equation to couple with the continuity equation, referred to here as the AR model. The PW and PW-type models are based on the momentum being conserved in the system, as with fluids, but they argue this is an unreasonable assumption for traffic and that simply replacing the *pressure* term with an *anticipation factor* describing how the *average driver* behaves is not a suffient fix for the differences between the two types of flow. They observe that intermediate states with negative velocities can be produced when solving the Riemann Problem:

$$U(x,0) = \begin{cases} U_- & \text{if} \quad x < 0, \\ U_+ & \text{if} \quad x > 0, \end{cases}$$

where $U := (\rho, v)$, which represents a jump in the traffic conditions. With these models they also point out that, with the same kind of initial data, adding a diffusion term in the acceleration equation would make things still worse, whereas adding a relaxation term would be harmless. However this would not prevent the same kind of paradox, at least for a short time, where at times the vehicles travel with negative velocities. They explain that the reason for the "unacceptable drawback" of the models that allow information to travel faster than the flow is due to the incorrect *anticipation factor*, $\frac{1}{\rho}p'(\rho)\rho_x$, involving the derivative of the pressure with respect to x. They further argue: "Assume that in front of a driver travelling with speed v the density is increasing with respect to x, but decreasing with respect to $(x - vt)$. Then the PW type of models predict that this driver would slow down, since the density ahead is increasing with respect to x! On the contrary, any reasonable driver would accelerate, since this denser traffic travels *faster* than him." They therefore conclude that the correct dependence must involve the *convective derivative*

$$\partial_t + v\partial_x$$

of the *pressure* P, which they still take as an *increasing* function of the density. They

consider p of the form

$$p = p(\rho) = \rho^\gamma, \quad \gamma > 0$$

where, in their words, the only qualitatively important conditions are the behaviour of this function p near a vacuum and the (strict) convexity of the function $\rho p(\rho)$. They therefore make the following assumptions:

$$\begin{array}{cc} p(\rho) \sim \rho^\gamma, & \text{near } \rho = 0, \\ \gamma > 0 & \text{and} \\ \forall \rho, & \rho p''(\rho) + 2p'(\rho) > 0. \end{array}$$

Finally they arrive at their model by assuming no diffusion and relaxation, which is given by the following system:

$$\rho_t + (\rho v)_x = 0,$$

$$(v + p(\rho))_t + v(v + p(\rho))_x = 0.$$

They comment that the above class of models (with a suitable choice of function p) satisfies the following Principles, that any reasonable model should satisfy:

Principles:

A. The system must be hyperbolic

B. When solving the Riemann Problem with *arbitrary* bounded nonnegative Riemann data (ρ, v) in a suitable region $\mathcal{R}$ of the plane, the density and velocity must remain nonnegative, and bounded from above.

C. In solving the same Riemann Problem with arbitrary data $U_\pm := (\rho_\pm, v_\pm)$, all waves connecting any state $U := (\rho, v)$ to its left (i.e. behind it) must have a propagation speed (eigenvalue or shock speed), at *most* equal to the velocity v.

D. The solution to the Riemann Problem must agree with the qualitative properties that each driver practically observes every day. In particular, braking produces shock waves, whose propagation speed can be either negative or nonnegative, whereas accelerating produces rarefaction waves which in any case satisfy Principle **C**.

E. Near a vacuum, the solution to the Riemann Problem must be very sensitive to the data. In other words, there must be no continuous dependence with respect to the initial data at $\rho = 0$.

They point out that Principle C is equivalent to their earlier point that a car travelling at a velocity v receives no information from the rear.

Their paper then demonstrates that the AR model does satisfy these principles. The eigenvalues, for example, are real and distinct, namely

$$\lambda_1 = v - \rho p'(\rho), \quad \lambda_2 = v,$$

thus the system is strictly hyperbolic, except when $\rho = 0$. Principle **A** is therefore satisfied. The fact that $p(\rho)$ is an increasing function means that $\lambda_1 < \lambda_2$, thus Principle **C** is satisfied since the faster wave will move at speed equal to the velocity of the vehicles, no faster.

They also point out that the spirit of their model is perfectly consistent with discrete car following models, see e.g. [7, 26], since, assuming a reaction of each driver to the distance to the previous car means (at the macroscopic level) that the correct modelling involves the convective derivative of the density, and not its derivative with respect to x.

Aw and Rascle claim their model might explain instabilities in car traffic flow, especially near a vacuum, in other words for very light traffic with few slow drivers. The maximum wave speed equals the flow of the traffic, hence giving it its anisotropic property. It also has an "anticipatory nature" as pointed out by Greenberg, [9], in that v and ρ behind a contact are determined by v and ρ ahead of it.

In a recent paper, Zhang, [40], has suggested another variation to the PW model to remove some of the failings of the original version. He concentrated on the wavespeeds and used these to suggest a suitable fix to the model, making it anisotropic as required, with its maximum wavespeed also equalling the velocity of the flow. Along with its ability to correctly describe "queue-end behaviour", the Zhang model claims to have eliminated the fluid-like properties that have made previous models unsuitable for describing traffic behaviour. His model is given by the conservation of mass equation

(2.5) coupled with the equation

$$v_t + vv_x = -C(\rho)v_x, \tag{2.22}$$

(using a convective derivative) and can be derived from a car-following model of the form

$$\tau(s_n(t))\ddot{x}_n(t) = \dot{x}_{n-1}(t) - \dot{x}_n(t), \quad s_n(t) = x_{n-1}(t) - x_n(t). \tag{2.23}$$

Here $C(\rho) = \rho V'(\rho)$ is the traffic sound speed at which small traffic disturbances are propagated relative to a moving traffic stream, $\ddot{x}_n(t)$ and $\dot{x}_n(t)$ are the acceleration and speed of the nth car respectively, and $\tau(s_n(t))$ is the driver response time, which is a function of local spacing $s_n(t)$. This model is studied in greater detail later, (see Chapters 5 and 7).

The derivation of (2.22) starts from the introduction of a velocity field $v(x,t)$: $\dot{x}_n(t) = v(x_n(t),t)$ and a vehicle spacing function $s(x,t) : s_n(t) = s(x_n(t),t)$; both are assumed sufficiently smooth. Next (2.23) is expressed in the new field variables

$$\tau(s(x(t),t))\frac{dv(x(t),t)}{dt} = \frac{ds(x(t),t)}{dt},$$

and further expanded to obtain

$$\tau(s)(v_t + vv_x) = s_t + vs_x, \tag{2.24}$$

where, for ease of notation $v(x(t),t) \equiv v$ etc.. Moreover, the conservation of vehicles implies that

$$s_t + vs_x = sv_x. \tag{2.25}$$

Substituting (2.25) into (2.24) one obtains

$$\tau(s)(v_t + vv_x) = sv_x,$$

which becomes (2.22) through the introduction of a traffic sound speed

$$\frac{s}{\tau(s)} = -\rho V'(\rho) \equiv -C(\rho) \geq 0,$$

as in Zhang [38].

Alternatively, (2.22) can be obtained by first expressing the right-hand side of (2.23) as $v(x(t) + s(x(t),t),t) - v(x(t),t)$ and then expanding $v(x(t) + s(x(t),t),t)$

about (x, t) up to first order. This derivation, however, is not exact because higher-order terms in the expansion are neglected, cf. Berg [3]. The benefit of taking this approach is that it can lead to a viscosity term v_{xx} if the second-order approximation is kept. The properties of the resulting newly derived viscous model are discussed in Zhang [39]. Why one derivation leads to (2.22) exactly and the other approximately is at present not fully understood. Although expressions $\dot{x}_{n-1}(t) - \dot{x}_n(t)$, $\dot{s}_n(t)$, $v_{n-1}(t) - v_n(t)$ are fully equivalent in the microscopic description, their counterparts in the macroscopic description, $\dot{s}(x(t), t)$ and $v(x(t) + s(x, t), t) - v(x(t), t)$ appear not to be so. Zhang believed that the definition and physical interpretation of the macroscopic field variables plays a subtle role in this discrepancy.

The PW, BMW, AR and Zhang macroscopic models are discussed in more detail in Chapter 5, as they form the basis of the study in this thesis along with the LWR model. We next describe the data to which we shall later apply the models.

Chapter 3

The Data

This chapter discusses the type of traffic data made available for this study and the procedures used to transfer it to a format suitable for use with the models discussed in Chapters 4 to 8. This is necessary since the models are for a single lane carriageway rather than a three or four lane motorway. Unfortunately no data is available from a stretch of a single carriageway. The velocity function and fundamental diagram obtained from the data and various functions fitted to these are then discussed.

3.1 Formatting The Data

The data available was collected (by the Highways Agency) from a stretch of the M25 Motorway during July 1999. There are a number of *loops* (posts) at approximately 500m intervals that record the number of vehicles passing, the average velocity and the occupancy at 1 minute intervals for each lane. The number of lanes varies between three and four depending on the position of the post relative to the on/off ramps. The innermost lane (lane 1 in Figure 3.1) serves as a slip lane close to on/off ramps (regions (a) and (c)), hence the road is reduced to three lanes in between the off and on ramp at a junction (region (b)).

The data supplied is the number of vehicles that passed each post per minute, or *count data*, the average velocity per lane over that minute and the *occupancy* or the percentage of time a vehicle was present at the loop over the minute, again for each lane. The count data can be thought of as a *flux* measurement. The density (in

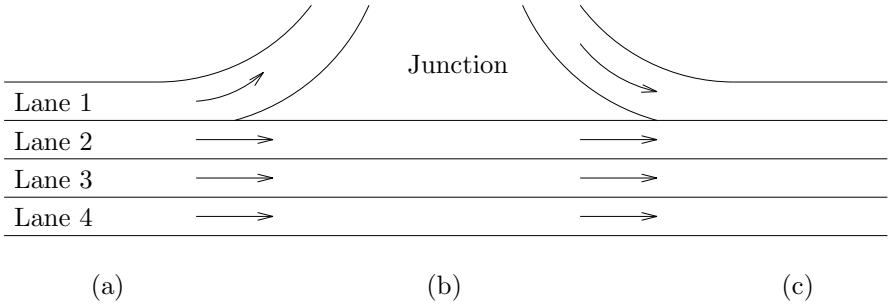

Figure 3.1: Displaying the road layout at a typical junction in the section of the M25 being considered.

vehicles per km) can then be calculated by multiplying the count by 60 and dividing by velocity. Count data doesn't take into account the size of the vehicles however, and so will not give a true representation of the headway available to vehicles which will ultimately affect the velocity at which the vehicle will choose to travel. A more representative choice for density is from the *occupancy data*. The data is given as temporal averages, so certain approximations have to be made. We know that the *distance covered by the average vehicle in 1 min=velocity/60=D* (Figure 3.2) and that the *flux=length in km of vehicles passing the post per minute*. Now, the amount of D taken up by vehicles can be approximated by $occupancy * D$ (an approximation since velocity is an average over the minute). This is therefore the flux, or kilometer of vehicles ($\times$ 100 since occupancy is a percentage) passing the post per minute.

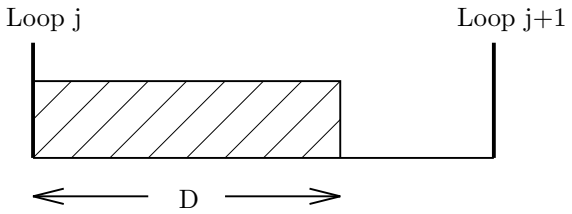

Figure 3.2: Diagram showing the approximation of vehicular flux between loops.

Similarly, occupancy is the percentage of time a vehicle is at the loop, and we can approximate the percentage taken up by vehicles per km by

$$density = \frac{flux}{velocity} \approx occupancy.$$

Occupancy is left as a percentage to keep the variables, density and flux, of the same order of magnitude as required by the models. The models were based on density

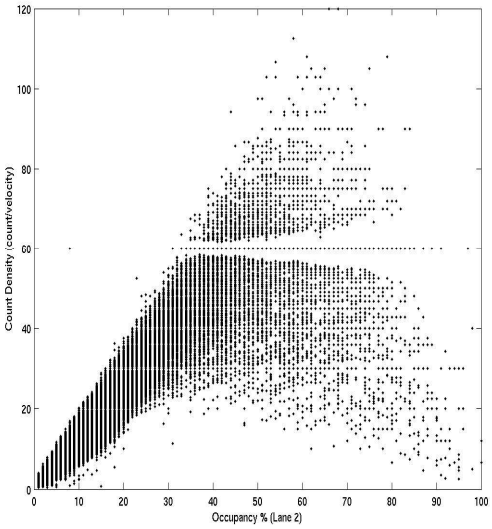

Figure 3.3: Plot of occupancy data versus count density data for Lane 2 from all posts. Data is taken at one minute intervals for a period of one week.

from the count data, i.e. number of vehicles per km. This however doesn't allow for the difference in vehicle length, and makes a further assumption that vehicle composition is constant. In reality vehicle lengths vary dramatically from the average car length (4m approx.) to lorries of length 11m+, with the proportions varying not only according to time of day, but minute by minute due to the relative speeds of the different types of vehicles.

Figure 3.3 is a plot of the occupancy data against the count density. It demonstrates the different occupancies for a given count density. This shows the varying vehicle composition. For a given count density, if those vehicles are small cars then the occupancy will be low: if, however, they are large lorries then the same number of vehicles will take up a larger proportion of the road, hence the occupancy will be much higher, and hence the traffic will behave differently, e.g. vehicles will drive more slowly due to the reduced space available.

To see if the two quantities, occupancy and count density, are interchangeable in the models, we now consider

$$occupancy = \frac{time\ \ vehicle\ \ present}{total\ \ time} \times 100.$$

Multiplying this by $velocity/velocity$ gives an approximation to

$$\frac{distance\ \ with\ \ vehicles\ \ present}{total\ \ distance} \times 100,$$

whereas

$$count\ \ density = \frac{number\ \ of\ \ vehicles}{total\ \ distance},$$

therefore, dividing by 100

$$\frac{occupancy/100}{count\ \ density} = \frac{distance\ \ with\ \ vehicles}{number\ \ of\ \ vehicles} = typical\ \ vehicle\ \ length.$$

Taking an average of these typical vehicle lengths gave a value $\approx 10m$, demonstrating that occupancy as a percentage is the correct order of magnitude as count density. We therefore use occupancy henceforth to represent density, believing it to be a more accurate representation of available space, or headway, that will affect drivers' behaviour. There is also an issue here about averaged data. The average of the quotient of two quantities is not equal to the quotient of the average of the two quantities. For this reason the spread of Figure 3.3 cannot be completely explained by the difference in occupancy and count density. Part of the spread will be due to the difference between the two average quotients. Individual vehicle data would eliminate the discrepancy between the two and show categorically the importance of taking into account the vehicle lengths. The feature which is present most prominently at count density of 60 veh/km remains unexplained but may be due to the measurements at the posts being integer values. Adding *noise* in the form of small rounding errors would most likely eliminate the *gaps* in the graph.

Two important features of the data can be observed from Figure 3.4, which is a plot of data from a typical lane (in this case lane 2). The left hand plot is occupancy against velocity of data collected from 1st-7th July 1999 at every post (1-61) at 1 minute intervals. The right hand plot is the corresponding *Fundamental Diagram* which is a plot of occupancy against flux. Both demonstrate a general shape, but also a wide spread. However, if we take thin strips in the vertical direction, then for each strip we take an average occupancy and corresponding average velocity (or flux), we obtain an average velocity and flux plot for each lane (Figure 3.5).

We now discuss the issue of the data being for a multi-lane carriageway, whereas the models we are considering are for single lane roads. The conservation of mass equation (see Chapter 4) for a single lane, common to all models, is given by

$$\rho_t + (\rho v)_x = 0.$$

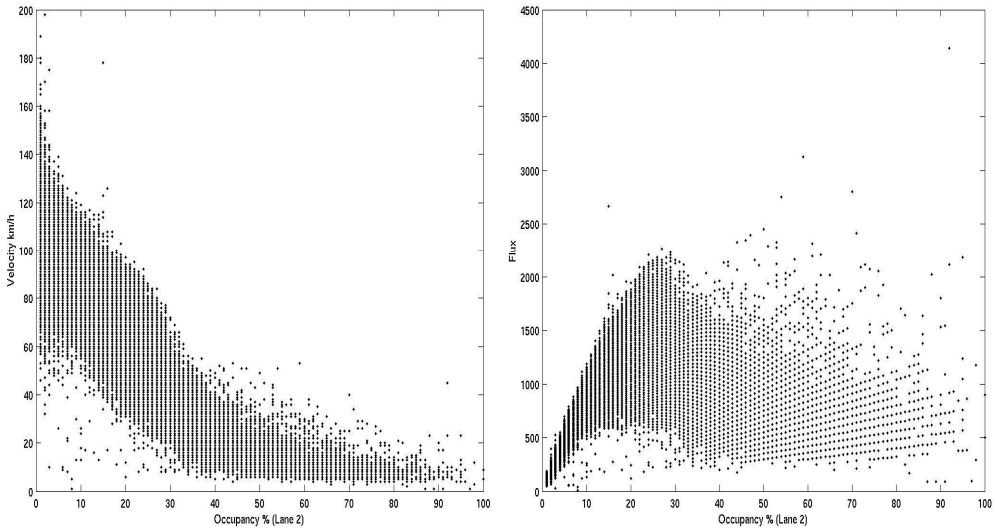

Figure 3.4: An example of the total data for one lane (in this case lane 2)

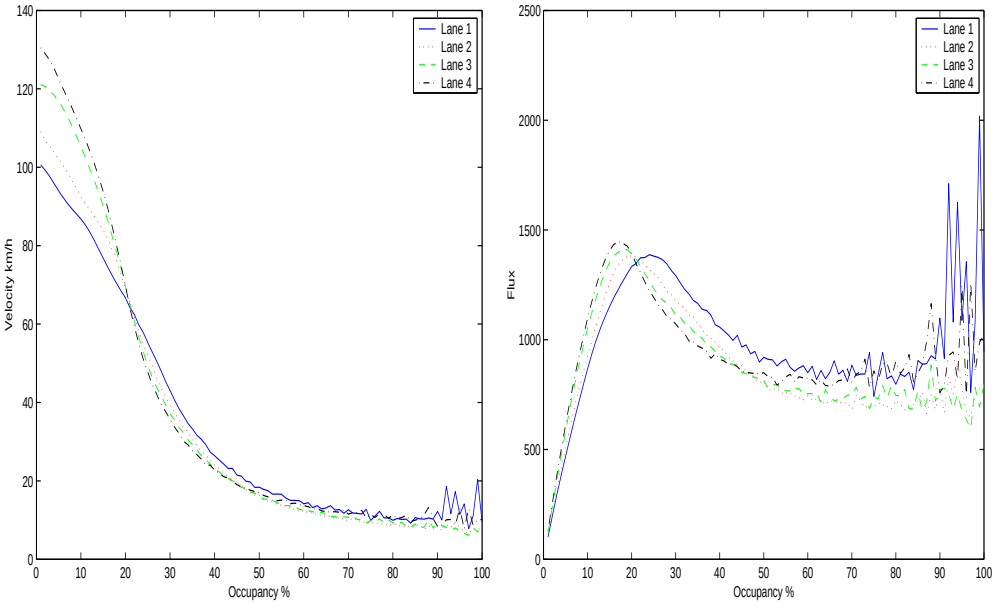

Figure 3.5: Average velocities and fluxes for given occupancies, for each lane.

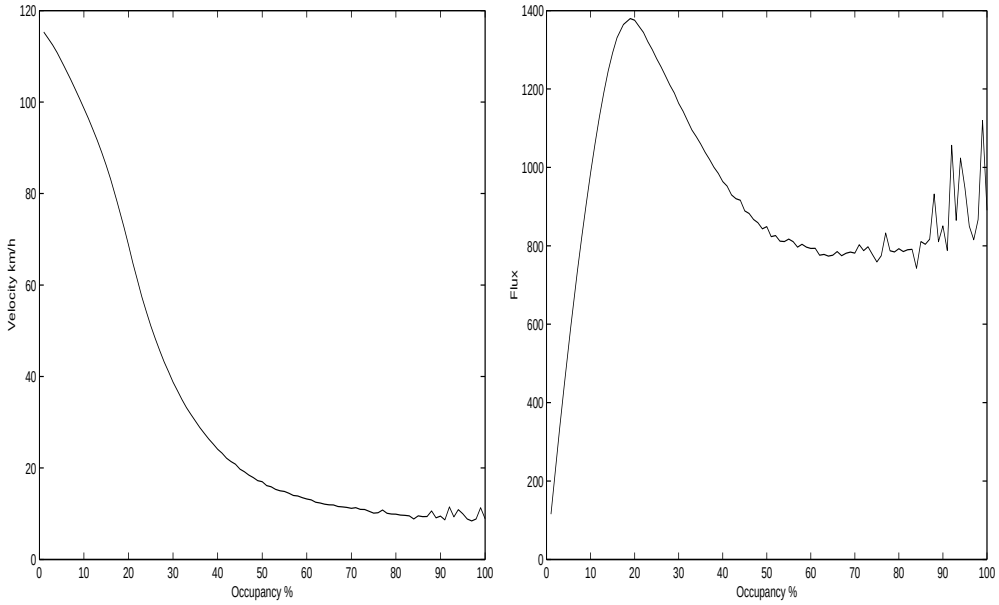

Figure 3.6: Average velocity and flux diagrams

Now consider multiple lanes and apply a conservation equation to each lane. To allow for lane changing between adjoining lanes i and $i+1$ there is an added transfer function $T_{i,i+1}$ which is a function of ρ_i, ρ_{i+1} in the simplest case. Therefore for lane i we have

$$\rho_{i,t} + (\rho v)_{i,x} - T_{i-1,i}(\rho_{i-1}, \rho_i) + T_{i,i+1}(\rho_i, \rho_{i+1}) = 0, \tag{3.1}$$

for $i = 1, 4$ where $T_{0,1} = T_{4,5} \equiv 0$. Adding the equations (3.1) we have

$$\left(\sum_{i=1}^{4} \rho_i \right)_t + \left(\sum_{i=1}^{4} \rho_i v_i \right)_x = 0. \tag{3.2}$$

Dividing (3.2) by 4 and hence taking an average mean value we have

$$\overline{\rho}_t + (\overline{\rho v})_x = 0,$$

where $\overline{\rho}$ is the average density over all lanes and $\overline{\rho v}$ is the average flux. From Figure 3.5 we see that the flux and velocity diagrams are qualitatively the same, so the flux and velocity diagram we will be using for our models from the data will be taken to be the average of these velocities and fluxes. Figure 3.6 is a representation of the *Velocity Function* from the real data together with the *Fundamental Diagram*.

3.2 Fitting Functions and the Fundamental Diagram

The Velocity Function and Fundamental Diagram in Figure 3.6 are key functions used in many different types of models, see discussions in Chapter 2. The shape of the functions will affect the behaviour of the models, therefore much effort has been spent finding accurate representations of these. There are many options for the choice of $V(\rho)$. The original choice in [36] was of the form

$$V_1(\rho) = v_{max}\left(1 - \frac{\rho}{100}\right) \tag{3.3}$$

(see (2.2)) where v_{max} is a given maximum speed on the road (typically 117km/h, chosen here as it is an average velocity in near zero density).

By considering the averaged real data in Figure 3.6 the velocity function,

$$V_2(\rho) = ae^{-b\rho} \tag{3.4}$$

captures many of the properties observed, although not all, (see f_R in Figure 3.8 (right), where $a = 195$ and $b = 0.05263$).

Another velocity function, similar to the one used by Kerner and Konhäuser in [16], [17] and [18], is

$$V_3(\rho) = \left(\frac{a}{b + e^{\frac{\rho - c}{d}}} + f\right), \tag{3.5}$$

where $a = 100$, $b = 0.8142$, $c = 23.35$, $d = 7.789$ and $f = 0.4972$ are found to be good choices for approximating the observed data.

In an attempt to approximate the flux function even more accurately the following two velocity functions were also considered. Firstly

$$V_4 = ae^{-b\rho} + \frac{c}{d + e^{\frac{\rho - f}{g}}} \tag{3.6}$$

where $a = 13$, $b = 0.007$, $c = 280$, $d = 0.8$, $f = 1.0$ and $g = 13.5$, which is a combination of V_2 and V_3. Secondly we considered

$$V_5 = a - b\left(\frac{e^{c(\rho-d)/f} - e^{g(\rho-d)/f}}{e^{(\rho-d)/f} + e^{-(\rho-d)/f}}\right) \tag{3.7}$$

where good choices of the coefficients are $a = 99.203$, $b = 83.872$, $c = 1.0137$, $d = 11.826$, $f = 13.395$ and $g = -0.011513$. Tha values of the constants in V_4 and V_5 were

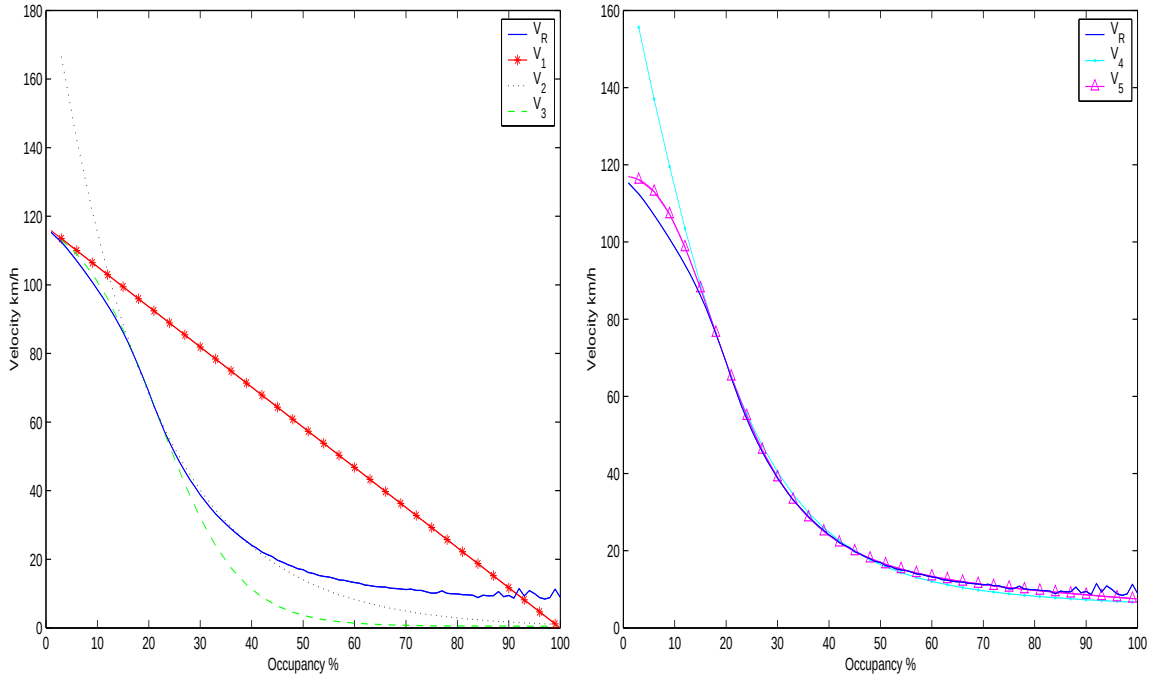

Figure 3.7: V_R is the real averaged data, V_1, V_2, V_3, V_4 and V_5 are velocity functions (note the different scales on the velocity axis for clarity).

found using *Mathematica*, fitting the functions to the key desirable features of the real data.

Figure 3.7 (left) shows the first three velocity functions (V_1, V_2 and V_3), and (right) shows V_4 and V_5, plotted against ρ, compared to the real velocity data V_R. Figure 3.8 shows the corresponding flux functions (f_1, f_2, f_3, f_4 and f_5) plotted against ρ, compared to the real flux data f_R.

It can be seen that f_4 and f_5 mimic the real data most closely. Chapter 4 uses f_2 to find the analytic solution to two test cases for the LWR model due to its simple form. Chapter 6 compares the analytic solution to the numerical solution. In Chapter 8 the five different flux functions described here are compared against the real data, and the best one chosen.

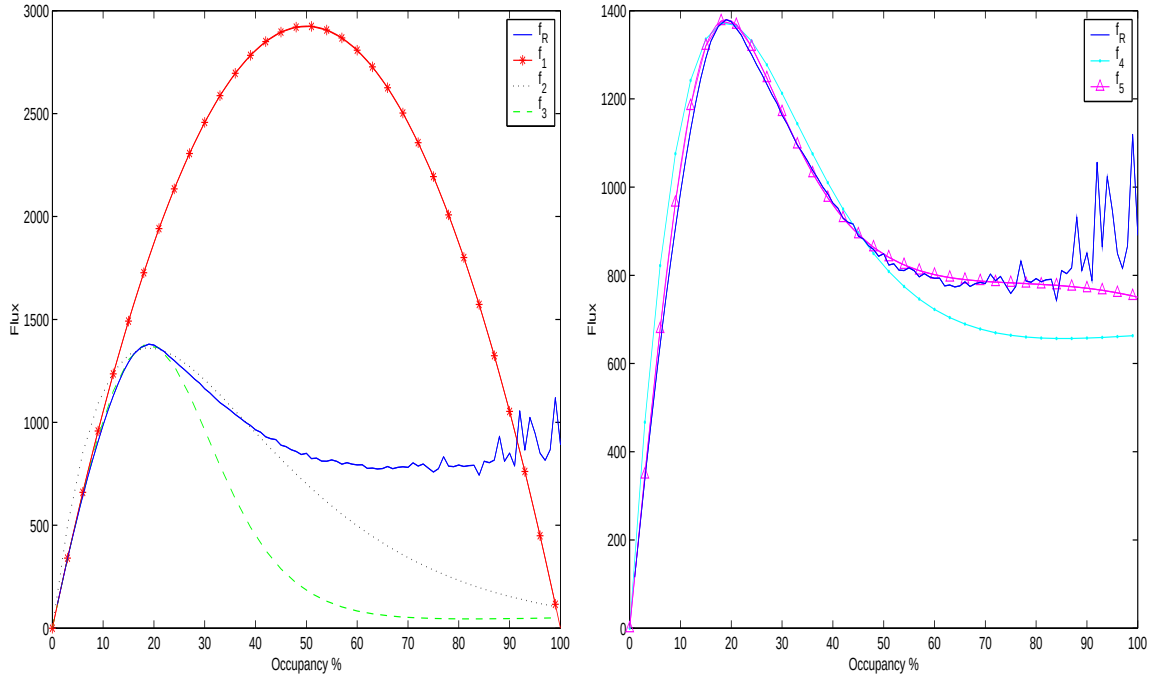

Figure 3.8: The Fundamental Diagram. f_R is the real data averaged for the momentum (ρv), and f_1, f_2, f_3, f_4 and f_5 are the flux functions. Note the different scales on the flux axis for clarity

Chapter 4

One-Equation Model

Traffic flow can be modelled either by using microscopic car-following theory, macroscopic fluid dynamic based models, or a combination of both (see e.g. Daganzo [5], Nagel [25] and Helbing [13]). This chapter considers the application of the early Lighthill-Whitham-Richards (LWR) model of traffic flow, proposed in the 1950's [23, 29], using functions fitted to averaged actual data gathered from the M25 motorway (supplied by TRL/Highways Agency), as discussed in Chapter 3. Analytic solutions to two particular test cases are then derived and compared to the numerical solutions from four different numerical schemes. The model studied is based on a single carriageway with no on or off ramps, and data is averaged over all available lanes.

4.1 The LWR Model

The LWR model,

$$\frac{\partial \rho}{\partial t} + \frac{\partial \left(\rho V\left(\rho\right)\right)}{\partial x} = 0, \tag{4.1}$$

is a single equation model, in effect a conservation of mass equation, where ρ is used to represent the traffic density (given as a percentage occupancy-see discussion in Chapter 3) and $V\left(\rho\right)$ is the velocity associated with that density. One of the basic assumptions about this model is that the velocity is a function of density alone, and that consequently any changes in density are immediately reflected in changes in the velocity. Obviously this argument has some flaws: for example, in practice reactions to changes in density do not happen instantaneously.

The velocity $V(\rho)$ and flux $f(\rho) = \rho V(\rho)$ for a given density are crucial in modelling the flow. The overall shape of the graph of $V(\rho)$ is still under debate, particularly for congested traffic flow. We have used velocity function V_2 here due to its simplistic form, however it is still a reasonable fit to the real data curve and the resulting flux function has lots of desirable features such as a maximum value and a point of inflection.

4.2 Method of Characteristics

The exact solutions are obtained using the method of characteristics. Using equation (4.1) with the normalised velocity function (3.4), i.e.

$$V(\rho) = e^{-9\rho}, \tag{4.2}$$

so that

$$f(\rho) = \rho e^{-9\rho} \tag{4.3}$$

(see Figure 4.3). We have from

$$\frac{\partial \rho}{\partial t} + \frac{\partial f\,(\rho)}{\partial x} = \frac{\partial \rho}{\partial t} + a(\rho)\frac{\partial \rho}{\partial x} = 0 \tag{4.4}$$

that

$$a(\rho) = \frac{df}{d\rho} = (1 - 9\rho)e^{-9\rho}. \tag{4.5}$$

Now, using the chain rule, we know that

$$\frac{d\rho}{dt} = \frac{\partial \rho}{\partial x}\frac{dx}{dt} + \frac{\partial \rho}{\partial t},$$

so that substituting $\frac{\partial \rho}{\partial t}$ in (4.4), we obtain

$$\frac{d\rho}{dt} - \frac{\partial \rho}{\partial x}\frac{dx}{dt} + a(\rho)\frac{\partial \rho}{\partial x} = 0,$$

giving

$$\frac{d\rho}{dt} - \frac{\partial \rho}{\partial x}\left(\frac{dx}{dt} - a(\rho)\right) = 0.$$

Therefore, $\frac{d\rho}{dt} = 0$ on the lines

$$\frac{dx}{dt} = a(\rho), \tag{4.6}$$

which implies that ρ and hence $a(\rho)$ is constant along these lines. These are the characteristics, which are straight lines in this case given by

$$x = at + x_0, \tag{4.7}$$

or

$$t = \frac{x - x_0}{a}, \tag{4.8}$$

where x_0 is the value of x at $t = 0$, and

$$a = (1 - 9\rho(x_0, 0))e^{-9\rho(x_0,0)} \tag{4.9}$$

from (4.5).

To obtain the exact solution, we trace the characteristic that passes through the point (x, t) back to the initial density profile, where ρ has the same value on that characteristic, i.e.

$$\rho(x, t) = \rho(x_0, 0) = \rho_0.$$

When characteristics cross, however, the solution becomes multiply defined and the continuous theory breaks down. This is encountered immediately when considering for example the square wave (4.13) (see Figure 4.3) at $x = 10$, where the two discontinuities need to be categorised into shocks, fans or combinations of both. To do this consider the flux function between the points to the left and right of the discontinuity, ρ_L and ρ_R. The shock speed s is given by the Rankine-Hugoniot jump condition, [21],

$$s = \frac{[f]}{[\rho]} = \frac{f(\rho_L) - f(\rho_R)}{\rho_L - \rho_R}. \tag{4.10}$$

If, for all $\rho \in [\rho_L, \rho_R]$, the entropy condition due to Oleinik is satisfied [21], i.e.,

$$R \equiv \frac{f(\rho_R) - f(\rho)}{\rho_R - \rho} \leq s \leq \frac{f(\rho_L) - f(\rho)}{\rho_L - \rho} \equiv L, \tag{4.11}$$

then a discontinuity is a shock. Figure (4.1) is a pictorial representation of this condition. However, the generic flux function (4.3) is non convex and we therefore need to check where ρ_L and ρ_R are situated relative to the point of inflection. The point of inflection of the flux function is at $\rho = \rho_I$, where

$$f''(\rho_I) = (81\rho_I - 18)e^{-9\rho_I} = 0,$$

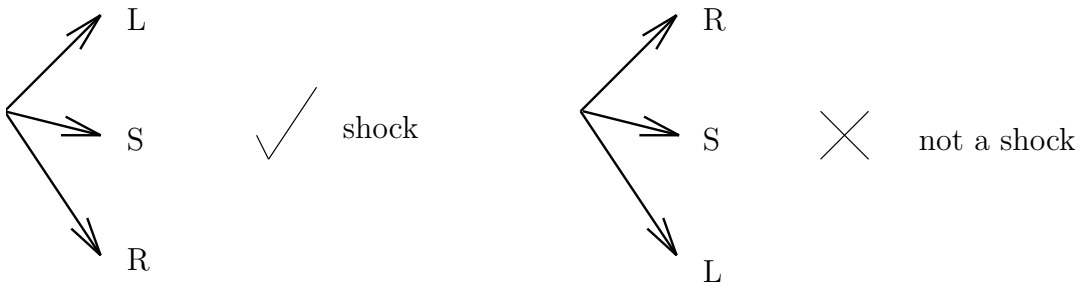

Figure 4.1: Pictorial representation of Oleinik's entropy condition. The slope between ρ_R and ρ is labelled R, between ρ_L and ρ is labelled L, while the shock speed given by the slope between ρ_L and ρ_R is labelled S. This condition must be satisfied for all $\rho \in [\rho_L, \rho_R]$ for the discontinuity to be a true shock.

hence

$$\rho_I = \frac{2}{9}. \tag{4.12}$$

Since for both discontinuities ρ_L and ρ_R lie on opposite sides of the point of inflection the entropy condition is not satisfied for either discontinuity in the square wave.

4.3 Application to Two Test Problems

To test the different numerical schemes derived later, exact solutions are derived for two test problems. Here the densities and velocity functions have been normalised to simplify the calculations: velocity has been divided by the maximal velocity v_{max} and density divided by some maximal bumper to bumper density ρ_{max}.

4.3.1 Square Wave

The first test problem is a square wave of height 1/2 with a density of 1/10 outside of the wave, Figure 4.2. The left side of the wave was positioned at a distance of 10 unit lengths from the left hand end of the road, and the right side of the wave positioned at 20 unit lengths. Hence

$$\rho(x,0) = \begin{cases} \frac{1}{2} & 10 \leq x \leq 20 \\ \frac{1}{10} & \text{otherwise .} \end{cases} \tag{4.13}$$

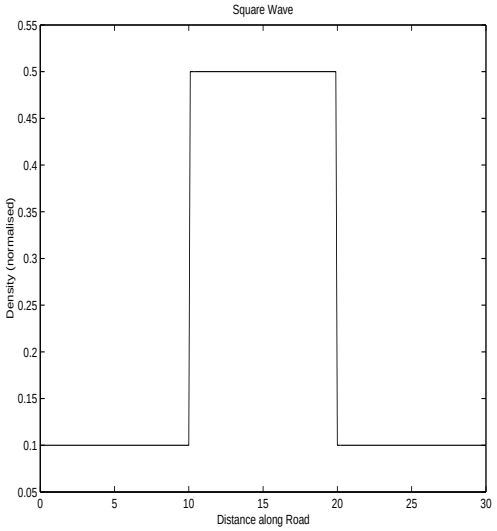

Figure 4.2: Test problem 1: Square wave.

We discuss the evaluation of this initial data. First consider the left hand discontinuity (at $x = 10$). The densities to the left and right of the discontinuity, ρ_L and ρ_R, are on opposite sides of the point of inflection in Figure 4.3. More precisely, $\rho_L < \rho_I < \rho_R$. The discontinuity must therefore be split into sections, each of which must be checked against the entropy condition (4.11). The sections are determined by drawing a line from ρ_L towards ρ_R, but making a tangent to the flux function rather than cutting through it. This tangential point is called $T1$ (see Figure 4.3). The positions of ρ_L and ρ_R are not drawn to scale on the top diagram in order to exaggerate the following points. The arrows in the top and bottom left diagram demonstrate the application of the entropy condition (4.11) which is satisfied for all $\rho \in [\rho_L, T_1]$, since $R < s < L$, the shock speed s always lying between L and R due to $T1$ being the tangential point. The discontinuity between ρ_L and $T1$ is therefore a shock. The bottom right diagram of Figure 4.3 shows the actual position of T1 in the discontinuity. This construction ensures that we have the correct entropy-satisfying weak solution for the shock [21].

The discontinuity from $T1$ to ρ_R is now checked against the entropy condition. Figure 4.4 demonstrates how (4.11) is not satisfied. The arrows show how $R > s > L$ for all $\rho \in [T1, \rho_R]$. The top part of the discontinuity, i.e. from $T1$ to ρ_R is therefore an expansion fan.

The right hand discontinuity (at $x = 20$) is treated similarly. Figure 4.5 demon-

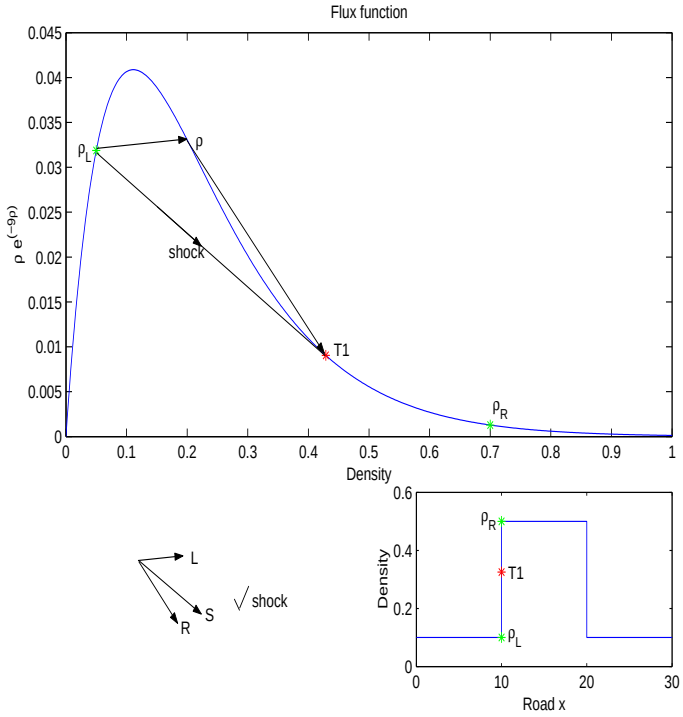

Figure 4.3: Diagram showing the tangent to the flux function, $T1$, from ρ_L and demonstrating ρ_L to $T1$ is a shock.

trates the position of the tangential point $T2$ from ρ_L towards ρ_R. The arrows again show how (4.11) is satisfied for $\rho \in [T2, \rho_L]$ and hence the discontinuity from $T2$ to ρ_L is a shock. Figure 4.6 demonstrates how the bottom section of the discontinuity, ρ_R to $T2$, fails to satisfy the entropy condition and is therefore an expansion fan. The right hand discontinuity is therefore also split into a shock and fan, but inverted compared to the left hand discontinuity.

Both shocks have fixed height and base initially, shock 1 on the left hand side, shock 2 on the right, and hence travel at constant speed according to the Rankine-Hugoniot jump condition (4.10). Initially shock 1 is moving with greater negative velocity than shock 2.

The rarefraction fan from T_2 to $\rho = 0.1$ on the right discontinuity will expand as expected to the right of the discontinuity, each point travelling according to the slope of the flux function $f'(\rho) = (1 - 9\rho)exp(-9\rho)$, which, from Figure 4.3, is negative, with decreasing speed as you move along the fan towards the base, giving a curve in the density profile that is concave upwards. The rarefraction fan from $T1$ to $\rho = 0.5$ also expands with each point moving with negative velocity, decreasing as you

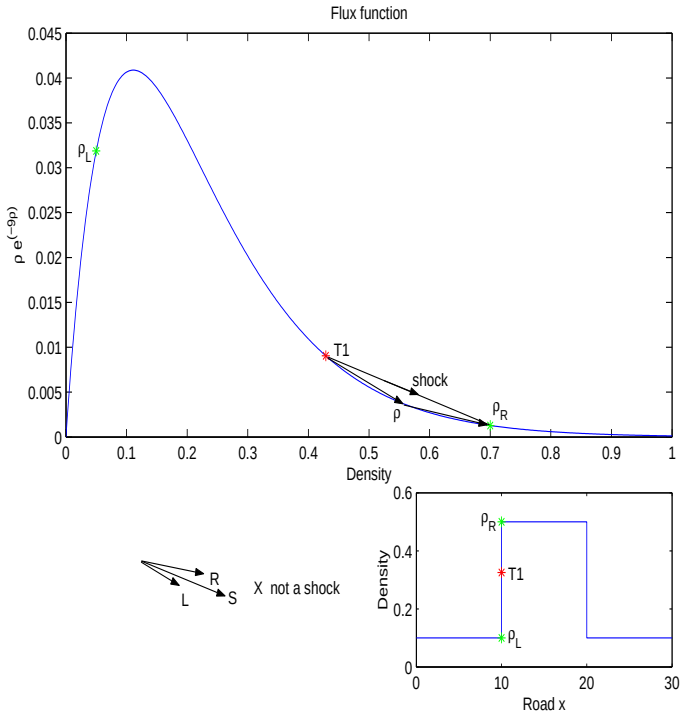

Figure 4.4: Diagram showing the tangent to the flux function, $T1$, from ρ_L and demonstrating $T1$ to ρ_R is not a shock.

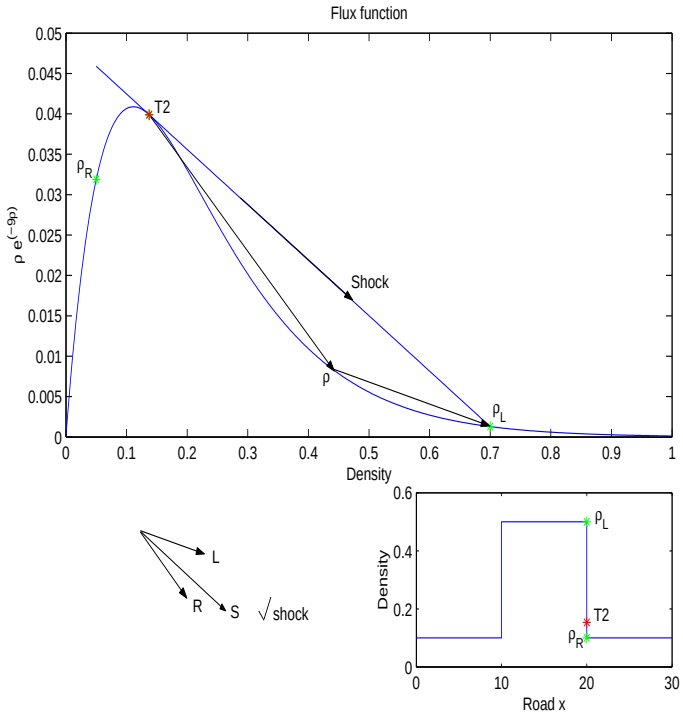

Figure 4.5: Diagram showing the tangent to the flux function, $T2$, from ρ_L and demonstrating ρ_L to $T2$ is a shock.

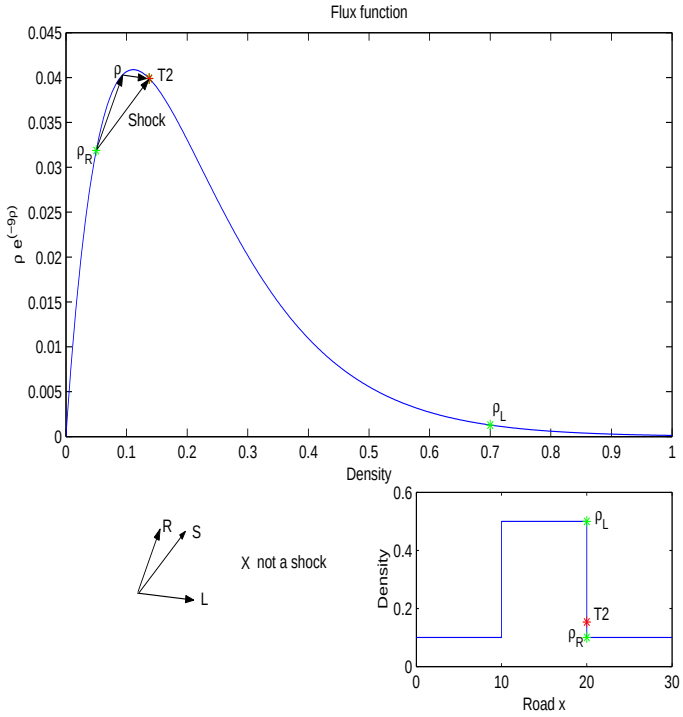

Figure 4.6: Diagram showing the tangent to the flux function, $T2$, from ρ_L and demonstrating $T2$ to ρ_R is not a shock.

approach ρ_R, again giving a concave density profile. The right of the fan, however, is moving more slowly in the negative direction than the second shock. The result is that whereas initially shock 2 is moving with constant velocity, once it catches up to the first expansion fan its height will no longer be fixed at $\rho = 0.5$. This height will be given by the point in the expansion fan it has caught up with. The base of the shock will therefore no longer be fixed, but is still given by the tangent from the height to the flux function, thus T2 increases. This has the effect of increasing the negative velocity of this shock, shock 3, giving it very different properties to shocks 1 and 2. This is demonstrated by Figure 4.7. Shocks 1 and 2 are straight lines with shock 1 moving faster, therefore having a more shallow slope than shock 2, also a straight line. Shock 3 has increasing negative speed also given by (4.10), therefore curves from shock 2 towards shock 1. This has the effect of creating two sections of fan to the right of the shock. The first as before, but as $T2$ increases the base of the shock fans out also.

Eventually shock 3 crosses shock 2 with the overall effect of the discontinuity collapsing into one smaller shock with base $\rho = 0.1$ from shock 1 and height $\rho = T2$ (current) from the base of shock 3. The speed of this shock is also negative but moves

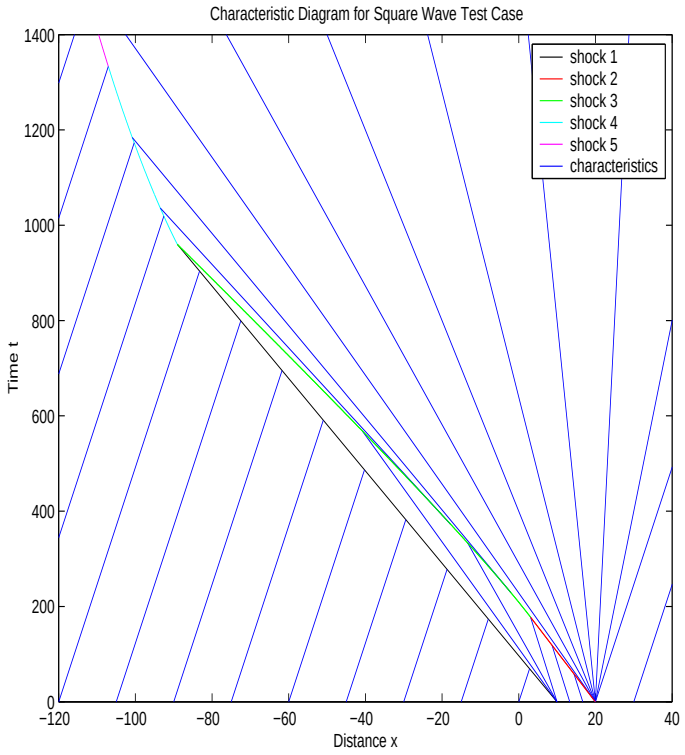

Figure 4.7: Characteristic diagram for square wave test problem.

slower in the negative direction than points in the top expansion fan. These points therefore move into this shock, thus decreasing its height until such a time as all the points from the top fan are absorbed into the shock. The resulting fifth shock is also moving faster than the points in the original fan and therefore the fan gets absorbed into the shock, also decreasing its height and varying its velocity. The velocity of this final shock gradually decreases and eventually moves with positive velocity, all the while catching up with the original fan. The movement of the shocks is demonstrated by Figure 4.8. Figure 4.9 shows the analytic solution of the density profile progressing with time for the square wave test problem.

Calculating the movement of the shocks requires the use of a numerical technique to solve the ordinary differential equations involved. The first two shocks are moving with constant velocity given by (4.10), (see Figure 4.9 at times 50 and 100), but when shock 2 reaches the top of the right hand fan the new shock 3 moves with varying velocity, dependent on the height of the fan reached (see Figure 4.9 at times 200 and 700). This will in turn affect the tangential point, $T2$, thus giving a smaller shock with greater negative velocity. Finding the point of the fan reached depends on the

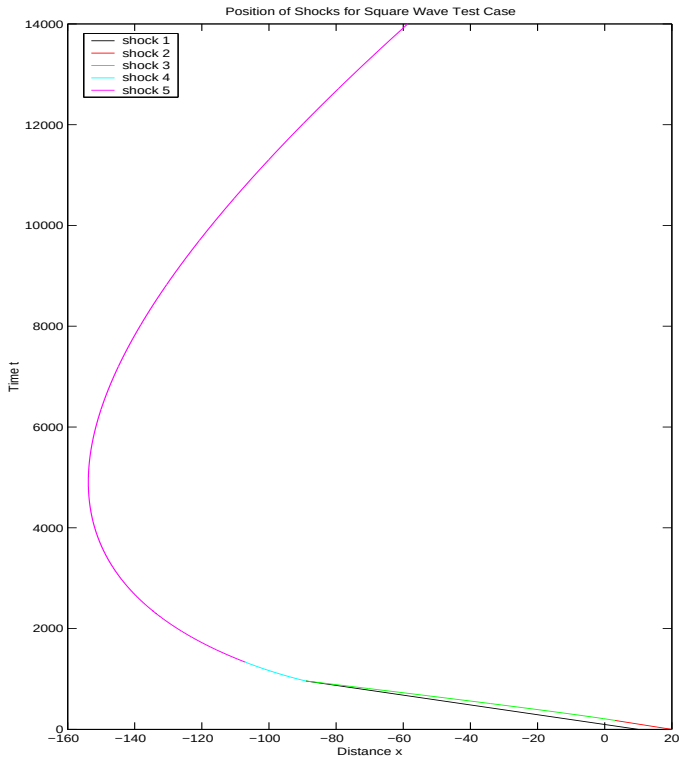

Figure 4.8: Positions of shocks only for square wave test problem.

speed of the shock, which is not known for all time. Thus, given the initial ρ_L, $T2$ and shock speed we can use the R-H shock equation, (4.10),

$$\frac{dx}{dt} = \frac{f(\rho_L) - f(T2)}{\rho_L - T2} = g(t, x), \tag{4.14}$$

to find the evolution of the shock. In general this equation needs a numerical method for its solution. We use the fourth order Runge-Kutta method, for which

$$x(t + \Delta t) = x(t) + \frac{1}{6}(K_1 + 2K_2 + 2K_3 + K_4),$$

with

$$\begin{aligned} K_1 &= \Delta t \;\; g(t, x) \\ K_2 &= \Delta t \;\; g\left(t + \frac{1}{2}\Delta t, x + \frac{1}{2}K_1\right) \\ K_3 &= \Delta t \;\; g\left(t + \frac{1}{2}\Delta t, x + \frac{1}{2}K_2\right) \\ K_4 &= \Delta t \;\; g\left(t + \Delta t, x + K_3\right), \end{aligned} \tag{4.15}$$

where, for each $K_2 - K_4$, the function g and therefore ρ_L and corresponding $T2$ need to be calculated. The new height, ρ_L, is calculated by the speed of the points in the

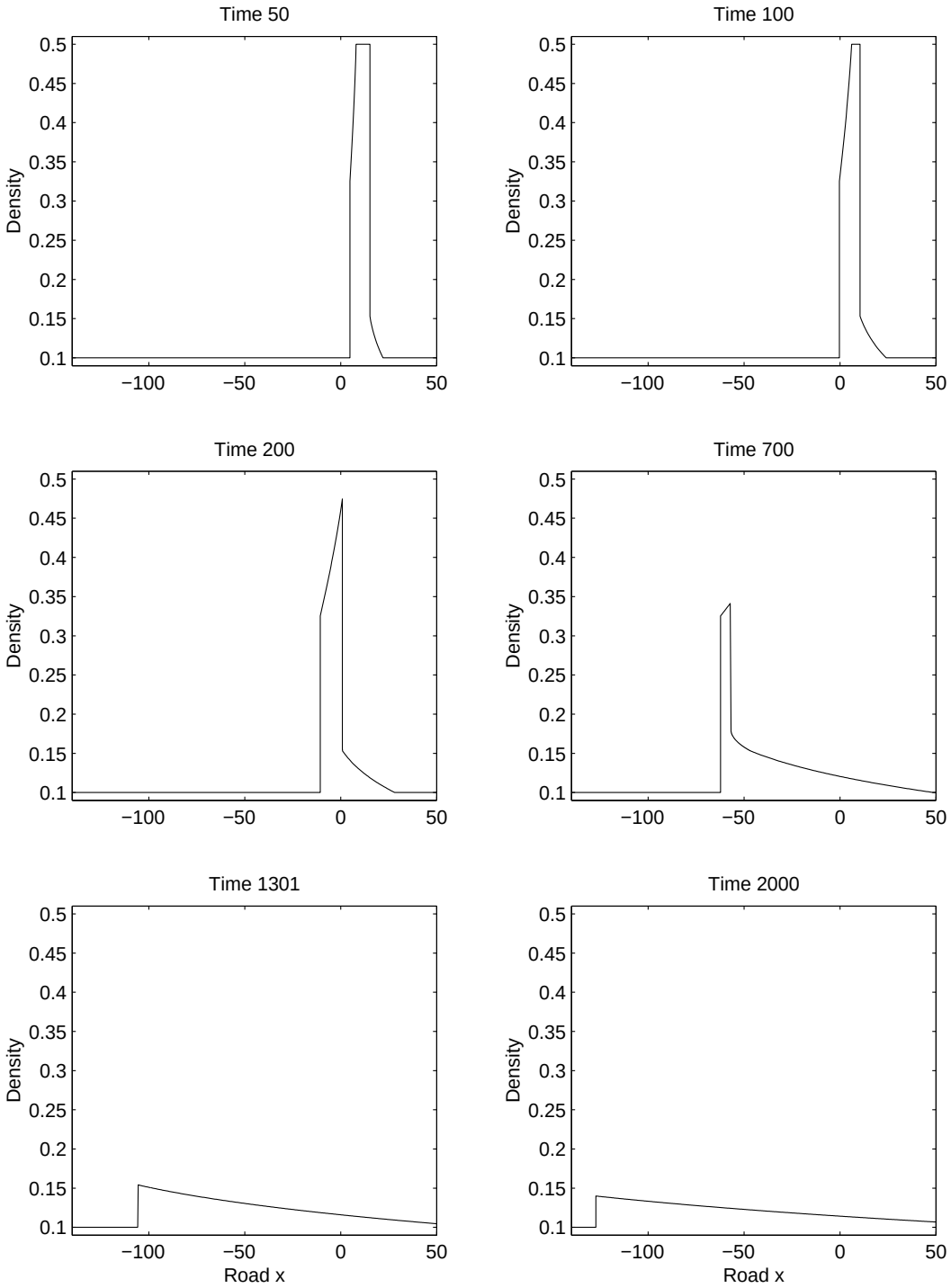

Figure 4.9: Analytic solution of the square wave test problem.

fan. Given the position (t, x), the point in the fan reached must be travelling at speed $\frac{x-10}{t}$. Equating this to the derivative of the flux function we can use Newton-Raphson iterations to determine ρ_L. Since

$$f'(\rho_L) = (1 - 9\rho_L)e^{-9\rho_L} = \frac{x-10}{t}, \tag{4.16}$$

we set

$$F = (1 - 9\rho_L)e^{-9\rho_L} - \frac{x-10}{t}.$$

We have

$$\frac{dF}{d\rho_L} = (81\rho_L - 18)e^{-9\rho_L},$$

so that using Newton-Raphson iterations we calculate

$$\rho_L^{new} = \rho_L^{old} - \left(\frac{dF}{d\rho_L}(\rho_L^{old})\right)^{-1} F(\rho_L^{old}), \tag{4.17}$$

until $|\rho^{new} - \rho^{old}| <$ a given tolerance, or until $|F|$ is sufficiently small. Once the new height of the shock is known, the new base must be calculated from the tangent to the flux function by equating the derivative of the flux function at $T2$ to the slope of the line between $(T2, f_{T2})$ and (ρ_L, f_L). This gives

$$f'(T2) = \frac{f_{T2} - f_L}{T2 - \rho_L}. \tag{4.18}$$

Multiplying through by $T2 - \rho_L$, we have

$$F = f_{T2} - f_L - (T2 - \rho_L)f'(T2) = 0.$$

Substituting for the flux function (4.3), we obtain

$$F = \left(9\,T2^2 - 9\,T2\rho_L + \rho_L\right)e^{-9\,T2} - \rho_L e^{-9\rho_L} = 0$$

$$\frac{dF}{d\,T2} = \left(-81\,T2^2 + T2(81\rho_L + 18) - 18\rho_L\right)e^{-9\,T2}, \tag{4.19}$$

and using the Newton-Raphson method again we can calculate $T2$ by (4.17). Once ρ_L and $T2$ are found, the new speed of the shock is calculated from (4.10) and the whole process is repeated until shock 3 crosses shock 1. When this happens the two shocks collapse and leave a smaller shock with base $\rho - 0.1$ and height of the final tangential point $T2$ from shock 3, with fans to the right (see Figure 4.9).

The movement of the fourth shock also requires some numerical evaluation. It has a base $\rho_L = 0.1$ and initially its height is given by the last tangent $T2$. Its initial speed is therefore

$$\frac{f(\rho_L) - f(T2)}{\rho_L - T2}.$$

This is only an instantaneous height however. The points of the fan immediately to the right of the shock move with a more negative velocity than the shock itself, and therefore move into the shock, thereby decreasing its height, thus changing its speed. Initially the points of the fan are from the base of the third shock fanning out due to its decreasing height. The characteristics are therefore tangents from the third shock going into shock 4 (see Figure 4.7). To calculate the movement of shock 4 we require the movement of shock 3, and more specifically the slope of the tangent at each iteration. We then work backwards along shock 3. Starting with the initial speed of shock 4 we find where the shock moving with this speed crosses the last tangent to shock 3. The density corresponding to the speed given by the slope of this tangent is calculated from (4.18) to (4.19). This is then the new height ρ_R of the shock, with a new speed given by (4.10). This process is repeated until the final tangent from shock 3 crosses shock 4, (see Figure 4.9 at time 1301).

The final stage is just a fifth shock followed by a fan created from the initial right hand discontinuity that was split into a shock and a fan (see Figure 4.9 time 100). Again the points in the fan have a greater negative velocity than the shock, and so move into it thus decreasing its height further and altering its velocity. The height of the shock ρ_R can easily be found using the fourth order Runge-Kutta method on

$$\frac{dx}{dt} = \frac{f(\rho_L) - f(\rho_R)}{\rho_L - \rho_R},$$

where $\rho_L = 0.1$ and ρ_R can be found using Newton-Raphson iterations, (4.16) to (4.17), given

$$f'(\rho_R) = \frac{x - 20}{t}.$$

Figure 4.9 at time 2000 is an example of the final shock fan left after all interactions have occurred. As demonstrated in Figure 4.8, shock 5 moves with increasing velocity due to its decreasing height and eventually moves off in the positive $x-$ direction while the base of the fan continues to spread. The full evolution is shown in Figure 4.9.

Helbing, [13], discussed how the LWR model with a linear flux function was unable to correctly predict the dispersion of a platoon of traffic, but here we see that with a non convex choice of flux function, the platoon can be dispersed from the front and the rear which is more like observed behaviour.

There is however a possible objection to this test problem in that traffic will perhaps never find itself in the initial state (4.13). For this reason we consider a possibly more realistic starting profile.

4.3.2 Half-Cosine Wave

The second test problem is a half cosine wave joined to a discontinuity, Figure 4.10. The density outside of the perturbation is again $\frac{1}{10}$. Hence

$$\rho(x,0) = \begin{cases} \frac{1}{2}\cos^2\left(\frac{\pi x}{20}\right) & 10 \leq x \leq 20 \\ \\ 0 & \text{otherwise} \end{cases} \tag{4.20}$$

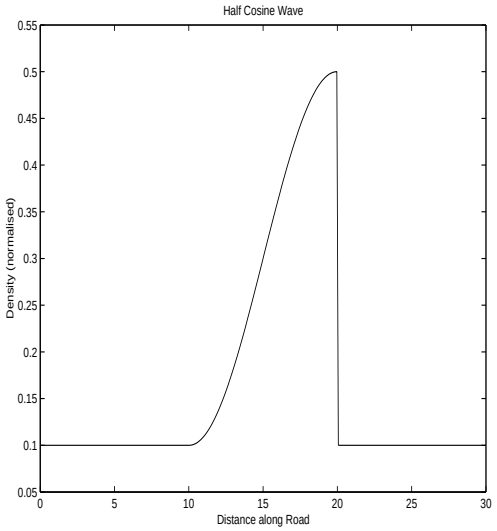

Figure 4.10: Test problem 2: Half cosine wave.

The second test problem, (4.20), can be treated similarly to the first. The discontinuity is of the same form as the right discontinuity of the square wave in that it also splits into a shock and a fan at the tangent point $T2$ from ρ_L to the flux function, see Figures 4.5 and 4.6. This shock has negative speed greater than the points on the

curve to its left, therefore the shock will start losing height immediately. The tangential point $T2$ therefore also changes immediately, unlike the square wave test problem that only changes height after the right hand shock catches up with the left hand fan. The movement of this shock is calculated in the same way as for the square wave test problem after the shock has caught the fan, i.e. in (4.14) and (4.15). Here, however, the points in the curve are travelling according to

$$x = f'(\rho_o)t + x_o, \tag{4.21}$$

where the velocity is given by

$$f'(\rho(x_o, 0)) \equiv f'(\rho_o) = (1 - 9\rho_o)e^{-9\rho_o}, \tag{4.22}$$

and the density, constant along characteristics, is

$$\rho(x_o, 0) \equiv \rho_o = \frac{2}{5}\cos^2\frac{\pi x_o}{20} + \frac{1}{10}.$$

ρ_L is therefore found by determining what point in the curve has been reached, and its corresponding initial position x_o.

Again, this is a non-linear problem so Newton iterations are used where, from (4.21),

$$F = f'(\rho_o)t + x_o - x,$$

with

$$\frac{dF}{dx_o} = f''(\rho_o)\frac{d\rho_o}{dx_o}t + 1,$$

where

$$f''(\rho_o) = (81\rho_o - 18)e^{-9\rho_o},$$

and

$$\frac{d\rho_o}{dx_o} = -\frac{\pi}{50}\sin\frac{\pi x_o}{10}.$$

So, from an initial guess x_o^{old}, x_o^{new} is calculated in a similar way to (4.17). Once we know x_o we can calculate the corresponding ρ_o from (4.20), i.e.,

$$\rho_o = \rho(x_o, 0) = \frac{1}{2}\cos^2\left(\frac{\pi x_o}{20}\right),$$

and this is ρ_L. The tangential point $T2$ is then calculated as before, (4.18, 4.19). We can then apply Runge-Kutta (4.15) to the movement of the shock where again $\frac{dx}{dt}$ is given by (4.14).

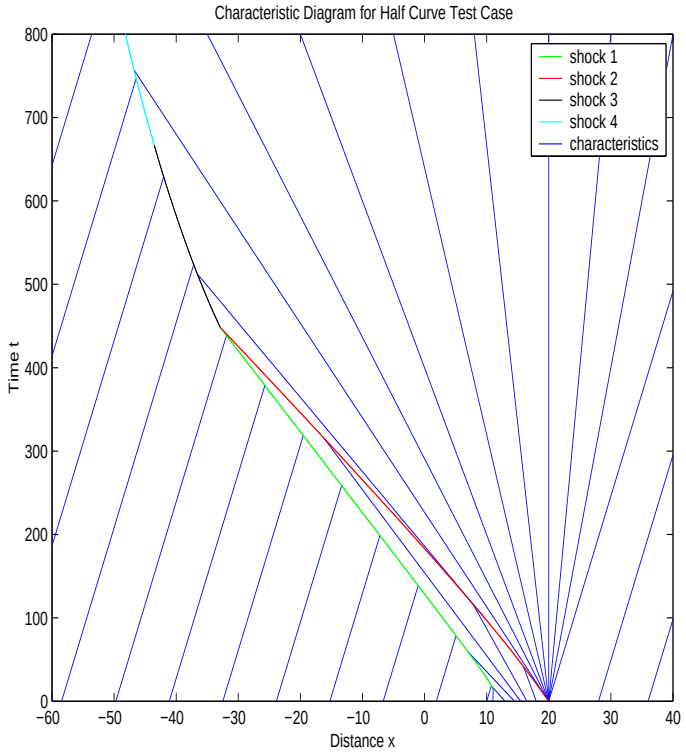

Figure 4.11: Characteristic diagram for half cosine wave test problem.

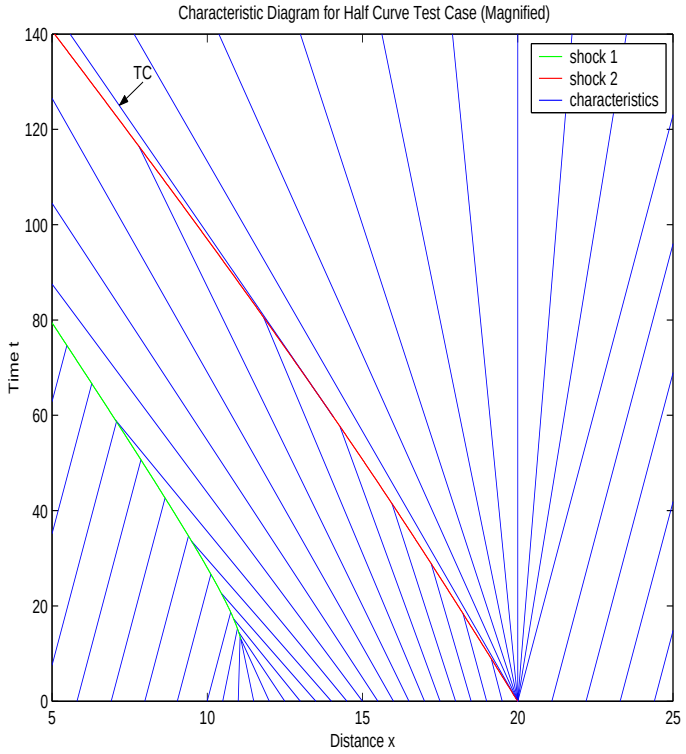

Figure 4.12: Close up of the characteristic diagram for half cosine wave test problem, TC being one of the characteristics tangent to shock 2.

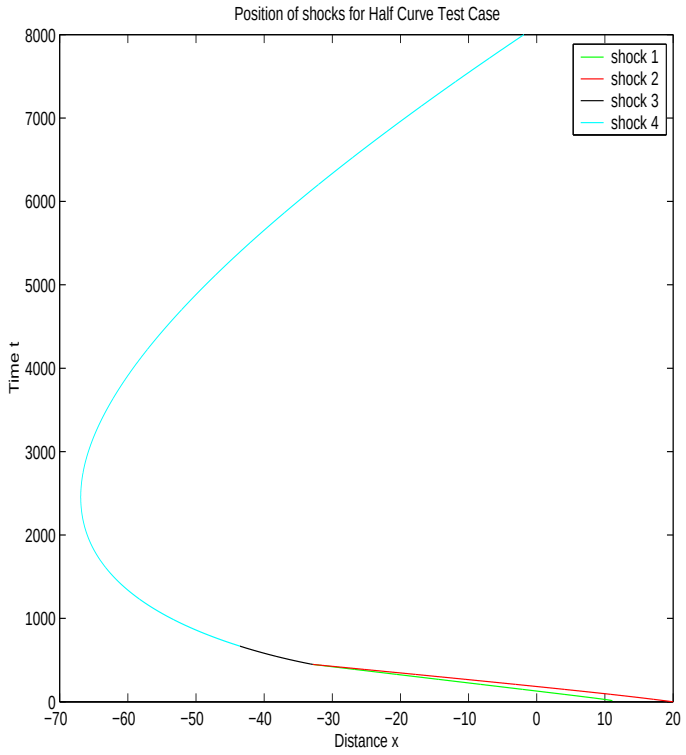

Figure 4.13: Positions of shocks only for half cosine wave test problem.

Each point in the curved section of the test problem will move with velocity given by (4.22). Due to the nature of the flux function however, these points will be moving at different speeds, some greater than others, and will therefore start to form a shock. This corresponds to where the characteristics, given by (4.7) to (4.9), first cross. This is found by using the *characteristic envelope* to determine when two neighbouring characteristics have the same value x at a given time t, i.e. where a small change in the initial position x_o produces no change in x, thus

$$\frac{dx}{dx_0} = 0. \tag{4.23}$$

Since x is given by (4.7), i.e.

$$x = at + x_0,$$

a is as in (4.9), i.e.

$$a = (1 - 9\rho(x_0, 0))e^{-9\rho(x_0,0)}$$

and

$$\rho_0 = \rho(x_0, 0) = \frac{1}{2}\cos^2\left(\frac{\pi x_0}{20}\right)$$

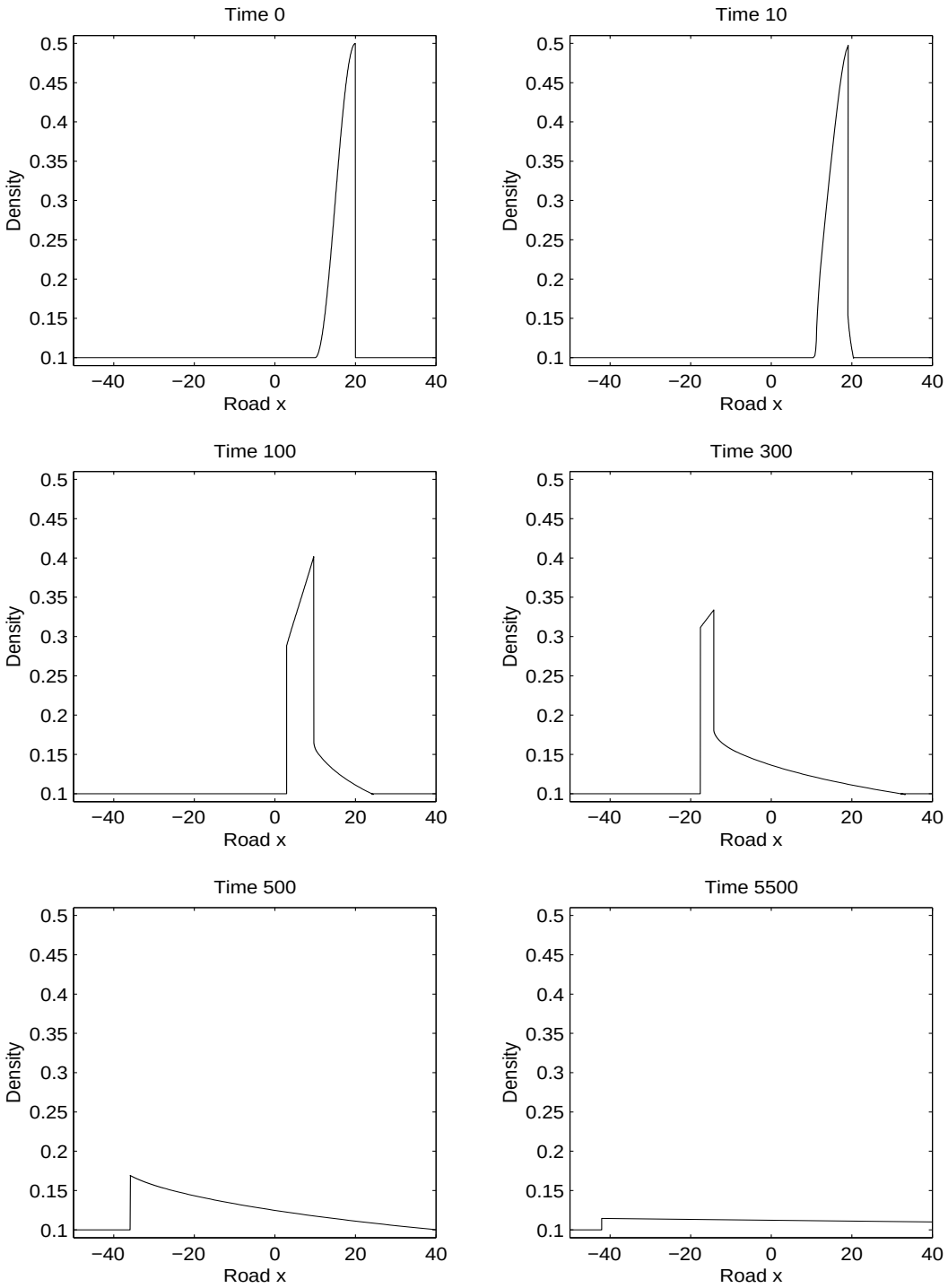

Figure 4.14: Analytic solution of the half cosine wave test problem.

for $10 \leq x_0 \leq 20$, then differentiating x w.r.t. x_0 gives

$$\frac{dx}{dx_0} = \frac{da}{dx_0}t + 1, \tag{4.24}$$

where

$$\frac{da}{dx_0} = \frac{da}{d\rho_0}\frac{d\rho_0}{dx_0} = \left((81\rho_0 - 18)e^{-9\rho_0}\right)\left(-\frac{\pi}{40}\sin\left(\frac{\pi x_0}{10}\right)\right).$$

Hence, $\frac{dx}{dx_0} = 0$ when

$$t = -\left(\frac{da}{dx_0}\right)^{-1}.$$

To find the time that the characteristics first cross, we seek the minimum value of t for which (4.23) holds, i.e. where $\frac{dt}{dx_0} = 0$ (and $\frac{d^2t}{dx_0^2} > 0$). Using Mathematica, this minimum value of t is found to be $= 12.86$ which corresponds to $x = 11.09$ with $\rho_o = 0.1243$, where $x_o = 11.59$.

This shock, shock 1, then moves off with speed s, (4.10), which is more negative (i.e. faster) than points to the left and less negative (i.e. slower) than points to the right, therefore it grows in size with decreasing base ρ_L and increasing height ρ_R. Again fourth-order Runge-Kutta is used to determine the movement of the shock with $g(t, x)$ given by an equivalent version of (4.14) with ρ_L and ρ_R where ρ_L and ρ_R are two solutions to the same Newton iterations (4.16) to (4.17), hence care with initial values for ρ_o^{old} is required.

The movement of both shocks is repeated simultaneously until they cross. At this point the two test problems are very similar, although this similarity occurs at different values of t. After the collision of shocks we are left with a single discontinuity, shock 3, with base $\rho_L = \frac{1}{10}$ originating from ρ_L of shock 1 and height from the final value of ρ_R of shock 2. This is connected to the fan that was to the right of shock 2. The movement of this shock-fan is then the same as for the previous test problem, where initially ρ_R is determined by the section of shock 2 that gradually fanned out due to the decreasing height of the discontinuity. This corresponds to characteristics originating from and tangent to shock 2 going into shock 3, (see Figure 4.12 where the characteristic labelled TC is one such tangent). Eventually ρ_R will decrease and change the shock speed so that the shock 4 moves into the original fan at the base of shock 1. Figure 4.11 is the full characteristic diagram for the movement of the half curve test problem. Figure 4.12 is a small section of (4.11) magnified to highlight the

formation of the shock and all the characteristics in the curved section. Figure 4.13 is the position of the shocks without the characteristics and demonstrates the movement of shock 4 after a long time and Figure 4.14 is a series of cross-sections of the density at various times.

4.3.3 Discussion

The first test problem is an idealised representation of a platoon of vehicles, i.e. a region of high density or a local cluster of traffic where $\rho = \frac{1}{2}$ surrounded by regions of low density, where $\rho = \frac{1}{10}$. The second test problem is perhaps slightly more realistic, in the sense that behind the shock the traffic is more spread out and varies smoothly between the low and high densities. Traffic approaching a jam ahead might slow down before reaching it in anticipation. This second test problem might therefore be representative of the removal of a partial blockage of a motorway in the presence of low density traffic and we might want to know how the traffic will evolve. As we have seen, after a sufficient amount of time the behaviour of the two test problems is qualitatively the same. A test problem combining the two, i.e. low density followed by a curve and plateau, joined to a region of low density by a discontinuity would model a partial blockage that has been present for a while before being removed. In this scenario the behaviour would be a combination of both test problems.

Consider the trajectories of the vehicles. Traffic flowing through these test profiles would experience what most drivers have experienced in motorway driving, that is the *phantom traffic jam*. While driving along in low density, suddenly a vehicle encounters a jam, or a region of slow moving high density traffic, then after a while the jam appears to clear without any apparent reason for the jam.

A vehicle approaching a platoon in test problem 1 would be travelling at $V(\rho_{low})$, i.e. high velocity, then reach the discontinuity and suddenly enter a region of high density. Figure 4.15 is a plot of the vehicle trajectory in the characteristic plane. That vehicle would adjust its velocity according to $V(\rho_{high})$, thereby travelling at a much reduced speed. The shock, however, is moving with negative velocity, therefore the slow moving car will pass through the shock and, assuming the platoon had been allowed to evolve before the vehicle had reached it, the car will then move into the

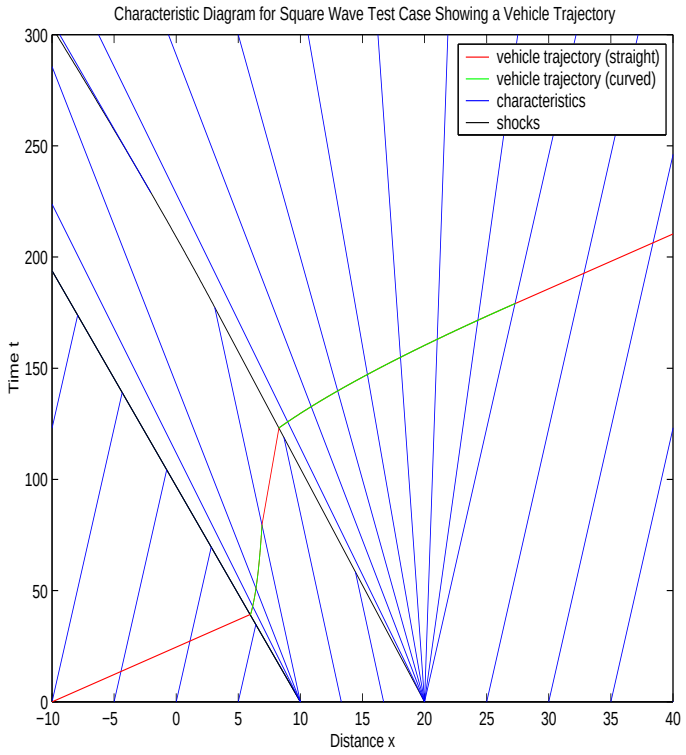

Figure 4.15: Characteristic diagram for square wave test problem with a vehicle trajectory.

fan region of increasing density. Again the points of the fan are moving with differing negative velocities, therefore the car will observe a smoother increase in density up to the maximum of $\rho = \frac{1}{2}$ (the green section of the trajectory in Figure 4.15). This seems reasonable since the shock might represent the traffic slowing down in advance of a jam ahead at the same time and propagating backwards, followed by a more gradual increase up to the maximum. This maximum is then experienced while the car moves through the plateau. Then, since the shock at the front of the platoon also has negative velocity, the vehicle will experience a sudden drop in density followed by a more gradual dispersion of the traffic ahead, i.e. the shock-fan in Figure 4.16.

Since the shocks propagate with negative speed, after some time the cluster will have moved against the flow of traffic down the road therefore a vehicle could feasibly clear the jam well before it reaches the original position of the partial blockage, thereby experiencing the jam *for no apparent reason.*

The second test problem would have similar observations with transitions being a little smoother initially, until the system is allowed to evolve to where the left shock is sufficiently large, in which case the driver would have much the same experience.

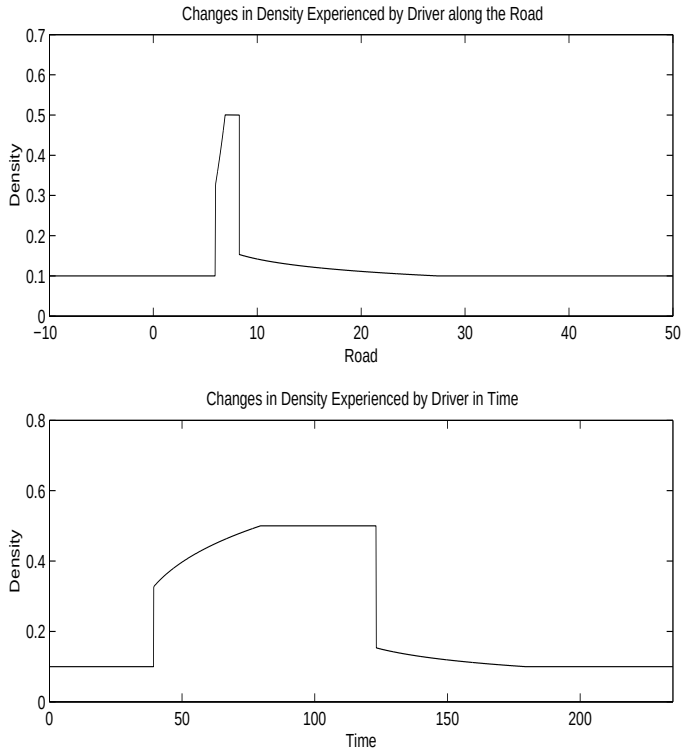

Figure 4.16: The conditions experienced by a vehicle, in space and in time .

There is also a second issue about the behaviour of the test profiles. An external person, e.g. from a helicopter or bridge, would observe the platoon moving slowly against the flow of traffic, then after sufficient time, the front shock would reach the shock at the rear of the platoon and the cluster would collapse to a much smaller discontinuity followed by a fan. This would represent the jam clearing itself and drivers present would also experience the disappearance of the jam, but for a different reason. Here it has actually cleared, whereas in the previous experience the car has simply moved through it and the platoon has propagated backwards against the flow.

The test problems are also an approximation to vehicles at a traffic light, (assuming no side roads), with a slight modification of having zero density to the right of the right hand discontinuity, being the position of the red light. The resulting characteristic diagram would be the same as for the test problems above, apart from the right hand fan would fan out from $T2$ as before down to zero, rather than $\rho = \frac{1}{10}$. The positions of the shocks etc. would be the same. According to Strang [32] and Haberman [10], the timings of the traffic lights must be such that they remain green to allow the shock at the rear of the queue (shock 1) to pass through the lights before they change back to

red, otherwise the traffic would crawl along and back up. In the above test problems this corresponds to allowing enough time for shock 5, (shock 4 in the half curve case), to change direction and move forwards of the lights, i.e. at $x = 20$.

As we will see later (in Chapter 8), the LWR model is unable to capture interactions between waves. To do this a system of equations is required. The next Chapter therefore discusses the systems we are going to consider in this thesis.

Chapter 5

Two-Equation Models

In this chapter we consider the application of *Higher Order Models*, or more accurately systems of equations, namely the PW model, BMW, AR and Zhang. All models consist of the conservation of mass equation (2.5) coupled with a second *traffic-like* equation to capture the complex interactions observed in traffic flow. Here we write the systems first in conservative form then in quasi-linear form and find the eigenvalue and eigenvectors for each. These are then used to create a test problem for the two-equation models and, in Chapter 7, to implement the numerical schemes.

5.1 Payne-Whitham Model

A two-equation model was proposed in the 1970's independently by Payne [27] and by Whitham [36], we shall refer to this as the PW model. The first equation is the conservation of mass equation as discussed earlier, i.e.

$$\frac{\partial \rho}{\partial t} + \frac{\partial f(\rho)}{\partial x} = 0 \tag{5.1}$$

with ρ representing the density of vehicles and the flux function $f(\rho) = \rho v$ where v is the velocity. In the one-equation model a particular form of $v(\rho)$ is assumed. In the two-equation models v and ρ are assumed to be independent and a second equation formed connecting them, as in a fluid model.

In the PW model the second equation is derived from the Navier-Stokes equation of motion for a one-dimensional compressible flow, but with a pressure $p = C_o^2 \rho$ and a

relaxation term. This gives

$$\frac{\partial v}{\partial t} + v\frac{\partial v}{\partial x} = -\frac{C_o^2}{\rho}\frac{\partial \rho}{\partial x} + \left(\frac{V(\rho) - v}{\tau}\right) + \frac{\mu}{\rho}v_{xx} \tag{5.2}$$

where C_o and τ are constants, and the velocity $V(\rho)$ is the 'maximal and out of danger' velocity meant to mimic drivers' behaviour. Kerner and Konhäuser [16], KK, describe $V(\rho)$ as being 'determined by the average balance between safety requirements and risk readiness of the driver as well as legal traffic regulations and road conditions'. There are many possible choices for the velocity function $V(\rho)$, as discussed earlier (3.3) to (3.7).

In order to rewrite the left hand side of (5.2) in conservative form, first we use the product rule

$$(\rho v)_t = \rho v_t + v\rho_t$$

and, substituting in for $v\rho_t$ after multiplying (5.1) by v, we have that

$$v(\rho v)_x + (\rho v)_t - \rho v_t = 0. \tag{5.3}$$

Substituting (5.3) into (5.2) multiplied by ρ gives

$$\rho v_t + \rho v v_x = -C_o^2\rho_x + \rho\frac{(V(\rho) - v)}{\tau} + \mu v_{xx}$$

while substituting for ρv_t from (5.3) gives

$$v(\rho v)_x + (\rho v)_t + \rho v v_x = -C_o^2\rho_x + \rho\frac{(V(\rho) - v)}{\tau} + \mu v_{xx}. \tag{5.4}$$

Again using the product rule on $(\rho v v)_x$, i.e.

$$(\rho v v)_x = (\rho v)_x v + (\rho v)v_x$$

and substituting in (5.4) for $(\rho v)_x v + (\rho v)v_x$ we obtain

$$\left(\frac{(\rho v)^2}{\rho}\right)_x + (\rho v)_t = -C_o^2\rho_x + \rho\frac{(V(\rho) - v)}{\tau} + \mu v_{xx}.$$

Hence we obtain the second equation (5.2) with the left hand side in conservative form

$$(\rho v)_t + \left(\frac{(\rho v)^2}{\rho} + C_o^2\rho\right)_x = \rho\frac{(V(\rho) - v)}{\tau} + \mu v_{xx}, \tag{5.5}$$

where ρ and ρv are the conserved variables. The source terms on the right hand side consist of a relaxation term and a viscosity term.

The two-equation conservative model, (5.1) and (5.5), can conveniently be written in the vector form

$$\mathbf{u}_t + \mathbf{f}(\mathbf{u})_x = \mathbf{R} \tag{5.6}$$

where

$$\mathbf{u} = \begin{pmatrix} \rho \\ \rho v \end{pmatrix}, \quad \mathbf{f}(\mathbf{u}) = \begin{pmatrix} \rho v \\ \dfrac{(\rho v)^2}{\rho} + C_o^2 \rho \end{pmatrix} \tag{5.7}$$

and

$$\mathbf{R} = \begin{pmatrix} 0 \\ \rho \dfrac{(V(\rho) - v)}{\tau} + \mu v_{xx} \end{pmatrix}.$$

Initially we shall consider the situation where there is no viscosity or relaxation, i.e. $\mathbf{R} = \mathbf{0}$, hence the problem reduces to that of isothermal flow [21].

Referring to (5.6), with $\mathbf{u}$, $\mathbf{f}(\mathbf{u})$ given by (5.7), we can write the system in quasi-linear form as

$$\frac{\partial \mathbf{u}}{\partial t} + A(\mathbf{u}) \frac{\partial \mathbf{u}}{\partial x} = \mathbf{0}, \tag{5.8}$$

where the matrix $A(\mathbf{u})$ is given by

$$A(\mathbf{u}) = \frac{\partial \mathbf{f}}{\partial \mathbf{u}} = \begin{pmatrix} 0 & 1 \\ C_o^2 - \dfrac{(\rho v)^2}{\rho^2} & \dfrac{2\rho v}{\rho} \end{pmatrix}. \tag{5.9}$$

We can then find the eigenvalues λ and corresponding eigenvectors $\mathbf{e}$ of A in order to diagonalise it. From

$$|A - \lambda I| = 0$$

$$(-\lambda)(2v - \lambda) - \left(C_o^2 - v^2\right) = 0$$

$$\lambda^2 - 2v\lambda - \left(C_o^2 - v^2\right) = 0$$

giving

$$\lambda_1 = v + C_o, \quad \lambda_2 = v - C_o. \tag{5.10}$$

Since there are two real distinct eigenvalues the system is hyperbolic, as for all the two-equation models considered.

To obtain the corresponding eigenvectors $\mathbf{e}_1$ and $\mathbf{e}_2$ we seek a vector $\mathbf{x}$ that satisfies

$$(A - \lambda I)\,\mathbf{x} = \mathbf{0}.$$

So for λ_1 we have

$$\begin{pmatrix} -v - C_o & 1 \\ C_o^2 - v^2 & v - C_o \end{pmatrix} \mathbf{x} = \mathbf{0}.$$

Choosing x_1 to be 1, we get $x_2 = v + C_o$, giving the eigenvector

$$\mathbf{e}_1 = \begin{pmatrix} 1 \\ v + C_o \end{pmatrix}. \tag{5.11}$$

Similarly for λ_2 we get

$$\mathbf{e}_2 = \begin{pmatrix} 1 \\ v - C_o \end{pmatrix}. \tag{5.12}$$

It is necessary to calculate the eigenvalues and corresponding eigenvectors in order to apply state-of-the-art upwind numerical schemes. The solution consists of two waves each moving with speed given by the eigenvalues, and strength derived from the corresponding eigenvectors. The flux functions are nonlinear, therefore it is difficult to derive exact solutions to the system for general initial data. However, the system is locally diagonalisable due to the linearly independent eigenvectors, and therefore some of the schemes applied are chosen to exploit this property.

5.2 Berg-Mason-Woods Model

Recently Berg, Mason and Woods (BMW), revisited the PW model in the form above, as used by Kerner and Konhäuser [16], and attempted to improve on it by deriving the model from car-following models, but without assuming the coefficient of the ρ_x term is constant, and including more higher order terms, arguing their significance is greater than previously thought [3]. Their model is given by (5.1) coupled with

$$v_t + vv_x = \frac{(V(\rho) - v)}{\tau} + \frac{V'(\rho)}{\tau}\left(\frac{\rho_x}{2\rho} + \frac{\rho_{xx}}{6\rho^2} - \frac{\rho_x^2}{2\rho^3}\right) \tag{5.13}$$

where τ is the relaxation time and $V(\rho)$ is taken to be the velocity function (3.7). Again we wish to write the left hand side in conservation form, therefore if we multiply (5.1)

by v and add it to $\rho\times$(5.13) we obtain

$$v\rho_t + \rho v_t + v(\rho v)_x + \rho v v_x - \frac{V'(\rho)}{2\tau}\rho_x = \rho\frac{(V(\rho)-v)}{\tau} + \frac{V'(\rho)}{\tau}\left(\frac{\rho_{xx}}{6\rho} - \frac{(\rho_x)^2}{2\rho^2}\right), \quad (5.14)$$

which can be rewritten as

$$(\rho v)_t + \left(\frac{(\rho v)^2}{\rho} - \frac{1}{2\tau}V(\rho)\right)_x = \rho\frac{(V(\rho)-v)}{\tau} + \frac{V'(\rho)}{\tau}\left(\frac{\rho_{xx}}{6\rho} - \frac{(\rho_x)^2}{2\rho^2}\right). \quad (5.15)$$

The BMW model, like PW, also contains a relaxation term but the viscosity includes higher order terms. The coefficient of the ρ_x term on the left hand side of (5.15) is given by $\frac{V'(\rho)}{2\tau}$, a function of ρ, whereas in the PW model it is just C_o, a constant. Other than this they have a similar form.

The conserved variables and flux function are given by

$$\mathbf{u} = \begin{pmatrix} \rho \\ \rho v \end{pmatrix}, \mathbf{f}(\mathbf{u}) = \begin{pmatrix} \rho v \\ \frac{(\rho v)^2}{\rho} - \frac{V(\rho)}{2\tau} \end{pmatrix}, \quad (5.16)$$

and the vector of right hand side terms $\mathbf{R}$ is

$$\mathbf{R} = \begin{pmatrix} 0 \\ \rho\frac{(V(\rho)-v)}{\tau} + \frac{V'(\rho)}{\tau}\left(\frac{\rho_{xx}}{6\rho} - \frac{(\rho_x)^2}{2\rho^2}\right) \end{pmatrix}. \quad (5.17)$$

The system can then be written in the form of (5.8), with

$$A(\mathbf{u}) = \begin{pmatrix} 0 & 1 \\ -\frac{V'(\rho)}{2\tau} - v^2 & 2v \end{pmatrix} \quad (5.18)$$

whose eigenvalues and corresponding eigenvectors are

$$\lambda_1 = v + \sqrt{\frac{-V'(\rho)}{2\tau}}, \quad \lambda_2 = v - \sqrt{\frac{-V'(\rho)}{2\tau}} \quad (5.19)$$

and

$$\mathbf{e_1} = \begin{pmatrix} 1 \\ v + \sqrt{\frac{-V'(\rho)}{2\tau}} \end{pmatrix}, \quad \mathbf{e_2} = \begin{pmatrix} 1 \\ v - \sqrt{\frac{-V'(\rho)}{2\tau}} \end{pmatrix}. \quad (5.20)$$

Since $V(\rho)$ is a monotonically decreasing function, $V'(\rho) \leq 0$, ensuring the eigenvalues and eigenvectors are real.

5.3 Aw-Rascle Model

A model by Aw and Rascle [1] that claims to be an improvement on the PW model has recently been proposed. They argue that other researchers have stuck too closely to fluid flow models and not allowed for significant differences between traffic and fluids, e.g. traffic is more concerned with the flow in front, rather than behind (see Chapter 2).

The model proposed by Aw and Rascle, henceforth known as AR, is

$$\frac{\partial \rho}{\partial t} + \frac{\partial (\rho v)}{\partial x} = 0$$

as in (5.1), together with a Lagrangian equation

$$\frac{\partial (v + P(\rho))}{\partial t} + v \frac{\partial (v + P(\rho))}{\partial x} = 0 \tag{5.21}$$

where $P(\rho)$ is a smooth increasing pressure function. They suggest

$$P(\rho) = C_0^2 \rho^\gamma \tag{5.22}$$

for the pressure where $\gamma > 0$, and $C_0 = 1$.

Multiplying (5.21) by ρ and using the product rule

$$(\rho (v + P))_t = \rho (v + P)_t + (v + P) \rho_t,$$

$$(\rho v (v + P))_x = \rho v (v + P)_x + (v + P) (\rho v)_x,$$

we get

$$(\rho (v + P))_t - (v + P) \rho_t + (\rho v (v + P))_x - (v + P) (\rho v)_x = 0. \tag{5.23}$$

Now, using (5.1), we can reduce the left hand side of (5.23) to

$$(\rho (v + P))_t + (\rho v (v + P))_x = 0. \tag{5.24}$$

This is now in conservative form, where the second conserved variable is $\rho (v + P) = y$, say. Hence, rewriting the AR system using the conserved variables ρ and y, equations (5.1) and (5.23) become

$$(\rho)_t + (y - \rho P)_x = 0,$$

$$(y)_t + \left(\frac{y^2}{\rho} - yP\right)_x = 0. \tag{5.25}$$

In the vector notation of (5.6) this is

$$\mathbf{u} = \begin{pmatrix} \rho \\ y \end{pmatrix}, \quad \mathbf{f}(\mathbf{u}) = \begin{pmatrix} y - \rho P \\ \dfrac{y^2}{\rho} - yP \end{pmatrix}, \quad \mathbf{R} = \mathbf{0}, \tag{5.26}$$

which can then be written in the form of (5.8), with

$$A(\mathbf{u}) = \begin{pmatrix} -(\gamma+1)P & 1 \\ -\dfrac{y^2}{\rho^2} - \dfrac{\gamma P y}{\rho} & \dfrac{2y}{\rho} - P \end{pmatrix} \tag{5.27}$$

whose eigenvalues and corresponding eigenvectors are

$$\lambda_1 = v, \quad \lambda_2 = v - \gamma P \tag{5.28}$$

and

$$\mathbf{e_1} = \begin{pmatrix} 1 \\ v + (\gamma+1)P \end{pmatrix}, \quad \mathbf{e_2} = \begin{pmatrix} 1 \\ v + P \end{pmatrix}. \tag{5.29}$$

5.4 Zhang Model

Another model has recently been proposed, by Zhang [40], that claims to be devoid of gas-like behaviour that plagues other higher-order models.

Again, it is a system consisting of the conservation of mass equation

$$\rho_t + (\rho v)_x = 0 \tag{5.30}$$

but here coupled with

$$v_t + (v + \rho V'(\rho))\, v_x = 0, \tag{5.31}$$

which is based on car-following models (see Chapter 2). This can be written in conservative form if we first expand out equation (5.30) to get

$$\rho_t + \rho v_x + v\rho_x = 0. \tag{5.32}$$

We then substitute for ρv_x from (5.32) into (5.31) to obtain

$$v_t + v v_x + V'(\rho)\,(-\rho_t - v\rho_x) = 0,$$

which can be rewritten as

$$v_t + vv_x - (V(\rho))_t - v((V(\rho))_x = 0,$$

or in Langrangian form as

$$(v - V(\rho))_t + v\,(v - V(\rho))_x = 0. \tag{5.33}$$

If we consider the products

$$\begin{aligned}(\rho(v - V(\rho)))_t &= \rho\,(v - V(\rho))_t + (v - V(\rho))\,\rho_t \\ (\rho v(v - V(\rho)))_x &= \rho v\,(v - V(\rho))_x + (v - V(\rho))(\rho v)_x,\end{aligned}$$

we can make substitutions into $\rho \times$ (5.33) giving

$$(\rho(v - V(\rho)))_t - (v - V(\rho))\rho_t + (\rho v(v - V(\rho)))_x - (v - V(\rho))(\rho v)_x = 0,$$

and using (5.30) we obtain, in conservative form,

$$(\rho(v - V(\rho)))_t + (\rho v(v - V(\rho)))_x = 0. \tag{5.34}$$

Letting $w = \rho(v - V(\rho))$ the system can be written as

$$\mathbf{u} = \begin{pmatrix} \rho \\ w \end{pmatrix}, \quad \mathbf{f}(\mathbf{u}) = \begin{pmatrix} w + \rho V(\rho) \\ \dfrac{w^2}{\rho} + wV(\rho) \end{pmatrix}, \tag{5.35}$$

whose Jacobian matrix is given by

$$A(\mathbf{u}) = \begin{pmatrix} \rho V'(\rho) + V(\rho) & 1 \\ -\dfrac{w^2}{\rho^2} + wV'(\rho) & 2\dfrac{w}{\rho} + V(\rho) \end{pmatrix}. \tag{5.36}$$

The eigenvalues and eigenvectors of this matrix are found to be

$$\lambda_1 = v, \quad \lambda_2 = v + \rho V'(\rho)$$

$$\mathbf{e}_1 = \begin{pmatrix} 1 \\ v - V(\rho) - \rho V'(\rho) \end{pmatrix}, \quad \mathbf{e}_2 = \begin{pmatrix} 1 \\ v - V(\rho) \end{pmatrix}. \tag{5.37}$$

5.5 Discussion on Wavespeeds

It is worth noting here the difference between the wavespeeds of the different models. The one-equation LWR model consists of a single wave whose velocity is given by the derivative of the flux function. For the generic test problems this lies in the range $[-25.73, v_{max}]$, which is not unreasonable, as information travels forward at a maximum no faster than the speed of the traffic. This is in keeping with the assumption that traffic is anisotropic, i.e. only reacts to conditions ahead. The PW model, however has two waves travelling at speeds given by $v \pm C_0$, one of which will always be travelling faster than the speed if the traffic, v. This is one of the reasons this model has been criticised. The same applies to the BMW model. The AR model has wavespeeds given by v and $v - \gamma P$. This seems reasonable since, as in the LWR model, the faster wave will move at the same speed as the traffic, no faster. This is also true of Zhang, whose wavespeeds are given by v and $v + \rho V'(\rho)$ with $V'(\rho) < 0$. This demonstrates the desirable anisotropic nature of the LWR, AR and Zhang models, and the isotropic nature of the PW and BMW models, for which PW-type models have been severely criticised. See Chapter 2 for further discussion.

Chapter 6

Numerical Methods for the LWR Model

In this chapter several numerical schemes to approximate the LWR model are described. Since equation (4.1) is in conservation form, where ρ is the conserved variable, a number of conservative numerical schemes are ideally suited to be applied to it. By choosing the velocity function V_2 of (3.4) and taking initial conditions (4.13), numerical results from various schemes can be compared to the analytic solution (Figure(6.2)) for the purpose of validation. The numerical schemes considered here are

- First Order Upwind with an Entropy Fix ([21])
- Engquist-Osher
- Lax-Friedrichs
- Second Order with a Flux Limiter (Minmod)

In order to implement these schemes first we need to set up the notation. The solution space (x, t) is split up into a uniform computational grid where the grid spacing in the x directon is given by Δx, and the spacing in the time direction is given by Δt. Where the grid lines cross is a node. The position of the jth node in the x direction and nth node in the time direction (x_j, t^n), is given by $(j\Delta x, n\Delta t)$. It is at these nodes that we wish to approximate the solution, i.e.

$$\rho(j\Delta x, n\Delta t) \approx \rho_j^n,$$

where ρ_j^n is our approximate value to the true solution $\rho(j\Delta x, n\Delta t)$.

There are many ways of approximating the partial differential equation we are trying to solve,

$$\rho_t + (\rho V(\rho))_x = 0. \tag{6.1}$$

Here we are concentrating on *shock capturing finite difference methods* because these methods are capable of automatically choosing the correct weak solutions, including shocks and shock speeds. These involve various ways of approximating the spatial and temporal derivatives. Here we will concentrate on schemes that approximate the temporal derivative ρ_t by a one-sided approximation given by

$$\rho_t \approx \frac{\rho_j^{n+1} - \rho_j^n}{\Delta t}.$$

In doing this the schemes that follow can all be written in the general form

$$\rho_j^{n+1} = \rho_j^n - \frac{\Delta t}{\Delta x}\left(h_{j+\frac{1}{2}} - h_{j-\frac{1}{2}}\right), \tag{6.2}$$

where h is the numerical flux, the difference in the schemes being how the flux derivative $(\rho V(\rho))_x$, is discretised, hence different definitions of h.

6.1 First Order Upwind

This scheme takes a one-sided difference of the space derivative, the direction depending on the wave direction. This can be determined by calculating the Courant number,

$$\nu_{j+\frac{1}{2}} = \frac{\Delta t}{\Delta x}\left[\frac{f\left(\rho_{j+1}^n\right) - f\left(\rho_j^n\right)}{\rho_{j+1}^n - \rho_j^n}\right], \tag{6.3}$$

which is an approximation to $\frac{\Delta t}{\Delta x}\times$ wave speed $(f'(\rho))$. For numerical stability this number should be less than one to ensure waves do not travel through more than one cell in any given time step. If the wave speed $\nu_{j+\frac{1}{2}}$ is positive then for this scheme $h_{j+\frac{1}{2}}$ in (6.2) is given by $h_{j+\frac{1}{2}} = f_j$, otherwise $h_{j+\frac{1}{2}} = f_{j+1}$.

As suggested by its name this scheme is first order accurate. This means the error generated by approximating the derivatives is of the order Δx in space and Δt in time. This can be found by considering the Taylor series expansion on the derivatives. For

example, for the time derivative expanding ρ_j^{n+1} about $(j\Delta x, n\Delta t)$ gives

$$\begin{aligned}\frac{\rho_j^{n+1}-\rho_j^n}{\Delta t} &= \frac{1}{\Delta t}(\rho(j\Delta x, n\Delta t)+\Delta t\rho_t(j\Delta x, n\Delta t)\\ &\quad +\frac{\Delta t^2}{2}\rho_{tt}(j\Delta x, n\Delta t)+O(\Delta t^3)-\rho(j\Delta x, n\Delta t)),\\ &= \rho_t(j\Delta x, n\Delta t)+\frac{\Delta t}{2}\rho_{tt}(j\Delta x, n\Delta t)+O(\Delta t^2),\end{aligned}$$

i.e. first order accuracy in time. A similar treatment of the spatial derivative yields the same result for the order of accuracy in space for this scheme.

First Order Upwind is equivalent to subtracting $\nu_{j-\frac{1}{2}}\Delta\rho_{j-\frac{1}{2}}$ from the value of ρ at either the left or right node ($j-1$ or j), depending on the wave direction, where $\Delta\rho_{j-\frac{1}{2}}=\rho_j-\rho_{j-1}$, unless $\rho_{j+1}^n=\rho_j^n$, in which case $\nu_{j+\frac{1}{2}}=\frac{\Delta t}{\Delta x}f'(\rho_j^n)$.

The algorithm may be summarised as follows.

- Initially, set $\rho_j^{n+1}=\rho_j^n\ \forall j$.
- If $\nu_{j-\frac{1}{2}}>0$ then

  $$\rho_j^{n+1}\rightarrow\rho_j^{n+1}-\nu_{j-\frac{1}{2}}\Delta\rho_{j-\frac{1}{2}}$$

  else $\nu_{j-\frac{1}{2}}<0$ and

  $$\rho_{j-1}^{n+1}\rightarrow\rho_{j-1}^{n+1}-\nu_{j-\frac{1}{2}}\Delta\rho_{j-\frac{1}{2}},$$

  noting here that if $\nu_{j-\frac{1}{2}}=0$, then the wave speed is zero, and the density does not change.

6.2 First Order Upwind with an Entropy Fix

A problem with applying the First Order Upwind scheme to an entropy violating discontinuity across the sonic point ρ_s is that, with a non-linear flux function the scheme may calculate the overall flux in the cell to be zero, hence the numerical solution does not disperse the jump which should disperse as an expansion fan (see Chapter 4). To overcome this a sonic entropy fix is required. For a fully convex/concave flux function, an intermediate non-physical point (ρ_m, f_m) which is the intersection of the tangents at ρ_R and ρ_L can be constructed in order to artificially split the discontinuity up into two smaller shocks that move with speeds given by the tangents, hence enabling the points of the fan to move off with the correct velocity.

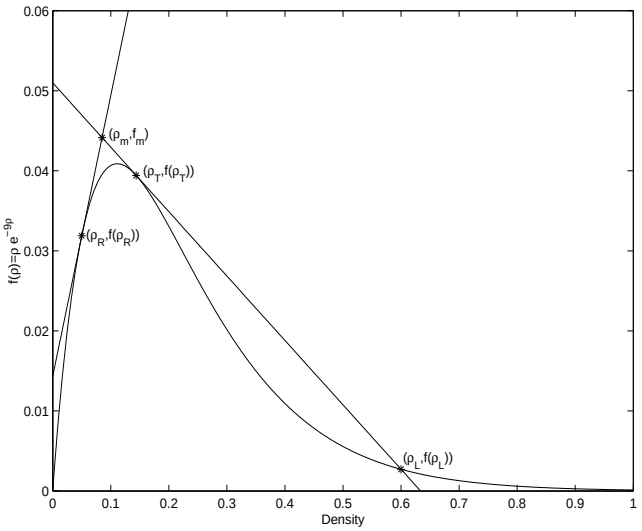

Figure 6.1: The flux function f_2 (normalised), the tangent to the curve at ρ_R, the tangent at ρ_T that passes through ρ_L, and their intersection ρ_m.

For a non-convex flux function, however, the intermediate point is the intersection of the tangent at ρ_R and the tangent that forms the convex hull of $f(\rho)$ from ρ_L (see Figure 6.1), where ρ_T is found as before (4.18)-(4.17). The point (ρ_m, f_m) is then found by equating the derivative of f to the equation of the slope of a line for the two tangents, i.e.

$$f'(\rho_R) = \frac{f_R - f_m}{\rho_R - \rho_m}, \tag{6.4}$$

and

$$f'(\rho_T) = \frac{f_m - f_T}{\rho_m - \rho_T}. \tag{6.5}$$

Eliminating ρ_m from (6.4) and (6.5) we have that

$$f_m = f_T + f'(\rho_T)\left(\frac{f'(\rho_R) - \hat{a}}{f'(\rho_R) - f'(\rho_T)}\right)(\rho_R - \rho_T), \tag{6.6}$$

where

$$\hat{a} = \frac{f_R - f_T}{\rho_R - \rho_T}.$$

The First Order Upwind with the Entropy Fix is then implemented by updating the affected nodes, i.e. all points that satisfy $\rho_R < \rho_s < \rho_L$ in this case, by

$$\rho_L^{n+1} = \rho_L^n - \frac{\Delta t}{\Delta x}\left(f_m - f_L\right)$$

$$\rho_R^{n+1} = \rho_R^n - \frac{\Delta t}{\Delta x}\left(f_R - f_m\right).$$

We can find ρ_m by substituting f_m back into (6.4) or (6.5). Once (ρ_m, f_m) is found, the single discontinuity is treated as two separate discontinuities where (ρ_R, ρ_T) is a rarefaction wave and (ρ_T, ρ_L) is a shock moving with a speed s, which, as in (4.10), is

$$s = \frac{f_T - f_L}{\rho_T - \rho_L}.$$

6.3 Engquist-Osher Scheme

From the discretisation given by (6.2), for the Engquist-Osher scheme h is defined by

$$h_{j+\frac{1}{2}} = f_j^+ + f_{j+1}^- + f(\rho_s) \tag{6.7}$$

and ρ_s is the sonic point of $f(\rho)$. We define f_j^+ and f_j^- in integral form as

$$\begin{aligned} f_j^+ &= \int_{\rho_s}^{\rho_j} \chi(u) f'(u) du, \\ f_j^- &= \int_{\rho_s}^{\rho_j} (1 - \chi(u)) f'(u) du, \end{aligned}$$

where

$$\chi(u) = \begin{cases} 1 & \text{if } f'(u) > 0 \\ 0 & \text{otherwise} \end{cases}$$

In regions where the flux function is convex these reduce to

$$f_j^+ = [f(u)]_{\rho_s}^{max(\rho_s,\rho_j)} = f(max(\rho_s, \rho_j)) - f(\rho_s)$$

$$f_j^- = [f(u)]_{\rho_s}^{min(\rho_s,\rho_j)} = f(min(\rho_s, \rho_j)) - f(\rho_s).$$

In regions where the flux function $f(\rho)$ is concave (i.e. $\dfrac{d^2 f}{d\rho^2} < 0$), f_j^+ and f_j^- are redefined by swapping max and min to give

$$f_j^+ = f(min(\rho_s, \rho_j)) - f(\rho_s)$$

$$f_j^- = f(max(\rho_s, \rho_j)) - f(\rho_s). \tag{6.8}$$

6.4 Lax-Friedrichs Scheme

Starting from the central difference scheme,

$$\rho_j^{n+1} = \rho_j^n - \frac{\Delta t}{2\Delta x}\left(f_{j+1}^n - f_{j-1}^n\right),$$

(which is linearly unconditionally unstable), the first order Lax-Friedrichs scheme replaces ρ_j^n with $\frac{\rho_{j+1}^n + \rho_{j-1}^n}{2}$ giving

$$\rho_j^{n+1} = \frac{\rho_{j+1}^n + \rho_{j-1}^n}{2} - \frac{\Delta t}{2\Delta x}\left(f_{j+1}^n - f_{j-1}^n\right), \tag{6.9}$$

which makes it conditionally stable.

6.5 Second Order Schemes

Alternative schemes can be constructed so that the truncation error is of the order Δx^2 or higher. The greater the order of accuracy the faster the truncation error reduces as you refine the mesh size. Higher order schemes, although they have this reduced truncation error, are prone to oscillations, particularly at discontinuities. Applying Flux Limiters is one way of reducing and in many cases eliminating these oscillations, at the expense of locally reducing the order of accuracy of the scheme. Flux Limiters are dealt with in the next section.

The second order scheme being considered here is best dealt with in two stages. The first stage is applying First Order Upwind (Section 6.1). The second stage is designed to take part of the value of ρ from one node and transfer it to the value of ρ at the next node, again the direction depending on the wave direction. With the right choice this gives the scheme second order accuracy.

Second order scheme is achieved, if $\nu_{j-\frac{1}{2}} > 0$, by adding the extra step

$$\rho_j^{n+1} \to \rho_j^{n+1} + \frac{1}{2}\frac{\Delta t}{\Delta x}\left(1 - \nu_{j-\frac{1}{2}}\right)\Delta f_{j-\frac{1}{2}}$$

$$\rho_{j-1}^{n+1} \to \rho_{j-1}^{n+1} - \frac{1}{2}\frac{\Delta t}{\Delta x}\left(1 - \nu_{j-\frac{1}{2}}\right)\Delta f_{j-\frac{1}{2}},$$

else if $\nu_{j-\frac{1}{2}} < 0$,

$$\rho_j^{n+1} \to \rho_j^{n+1} - \frac{1}{2}\frac{\Delta t}{\Delta x}\left(1 + \nu_{j-\frac{1}{2}}\right)\Delta f_{j-\frac{1}{2}}$$

$$\rho_{j-1}^{n+1} \to \rho_{j-1}^{n+1} + \frac{1}{2}\frac{\Delta t}{\Delta x}\left(1 + \nu_{j-\frac{1}{2}}\right)\Delta f_{j-\frac{1}{2}}. \tag{6.10}$$

This is the Lax-Wendroff scheme.

6.6 Second Order Schemes with a Flux Limiter (Minmod)

Second order schemes normally give oscillations near shocks but these can be suppressed by the use of flux limiters in the second stage above [34]. The first stage is applying First Order Upwind as before (Section 6.1).

The second stage (6.10) is rearranged to introduce a ratio r of flux differences which is then monitored to check for over or undershoots. A limiter function $\phi(r)$ kicks in only in the event of these over or undershoots, supresses them and reduces the order of accuracy locally.

The second order stage with the limiter is, if $\nu_{j-\frac{1}{2}} > 0$,

$$\rho_j^{n+1} \rightarrow \rho_j^{n+1} + \frac{1}{2}\phi\left(r_{j-1}^+\right)\nu_{j-\frac{1}{2}}\left(1-\nu_{j-\frac{1}{2}}\right)\Delta\rho_{j-\frac{1}{2}}$$

$$\rho_{j-1}^{n+1} \rightarrow \rho_{j-1}^{n+1} - \frac{1}{2}\phi\left(r_{j-1}^+\right)\nu_{j-\frac{1}{2}}\left(1-\nu_{j-\frac{1}{2}}\right)\Delta\rho_{j-\frac{1}{2}},$$

else $\nu_{j-\frac{1}{2}} < 0$

$$\rho_j^{n+1} \rightarrow \rho_j^{n+1} - \frac{1}{2}\phi\left(r_j^-\right)\nu_{j-\frac{1}{2}}\left(1+\nu_{j-\frac{1}{2}}\right)\Delta\rho_{j-\frac{1}{2}}$$

$$\rho_{j-1}^{n+1} \rightarrow \rho_{j-1}^{n+1} + \frac{1}{2}\phi\left(r_j^-\right)\nu_{j-\frac{1}{2}}\left(1+\nu_{j-\frac{1}{2}}\right)\Delta\rho_{j-\frac{1}{2}},$$

where $r_j^{\pm}$ are defined as

$$r_j^+ = \frac{\left(1-\nu_{j-\frac{1}{2}}\right)\Delta f_{j-\frac{1}{2}}}{\left(1-\nu_{j+\frac{1}{2}}\right)\Delta f_{j+\frac{1}{2}}}, \quad r_j^- = \frac{\left(1+\nu_{j+\frac{1}{2}}\right)\Delta f_{j+\frac{1}{2}}}{\left(1+\nu_{j-\frac{1}{2}}\right)\Delta f_{j-\frac{1}{2}}}. \tag{6.11}$$

Here r_j^+ is r for a positive wave speed and r_j^- is r for a negative wave speed, where $\nu_{j+\frac{1}{2}}$ is as in (6.3) and $\phi(r)$ is the limiter.

There are various flux limiters $\phi(r)$ available, one being Roe's Minmod limiter [34]. This is defined as

$$\phi(r) = max\left(0, min\left(r, 1\right)\right)$$

which gives the output 1 if $r > 1$, 0 if $r < 0$, and r if $0 < r < 1$.

Since r is defined by (6.11), then when programming the limiter it is worth noting that if r is the output then its denominator will cancel with a term multiplying it, so r need not necessarily be calculated explicitly. Merely comparing the relative magnitudes

of the numerator and denominator will decide the output. For example, if a is the numerator of r, where

$$a = \alpha_{k-\frac{1}{2}}(\Delta f_{k-\frac{1}{2}}),$$

and b is the denominator of r, where

$$b = \alpha_{k+\frac{1}{2}}(\Delta f_{k+\frac{1}{2}}),$$

then

$$ab < 0 \Rightarrow \frac{a}{b} < 0 \Rightarrow \phi = 0.$$

If $ab > 0$ where either

$$abs(a) > abs(b) \Rightarrow \frac{a}{b} > 1 \Rightarrow \phi = 1$$

or

$$abs(a) < abs(b) \Rightarrow \frac{a}{b} < 1 \Rightarrow \phi = \frac{a}{b} = r$$

we can implement the limiter using $\psi = \phi b$, hence eliminating the need to calculate r, as this causes problems when $\Delta f \to 0$.

By substituting 1 for $\phi(r)$ and simplifying, we return to the Second Order scheme without flux limiter, which is the same as the Lax-Wendroff scheme (6.10).

6.7 Comparison of Schemes on the Test Problems

Figure 6.2 shows the analytic solution after time $t = 201$ for the test problem of the square wave compared to the four schemes above, and Figure 6.3 shows the analytic solution compared to Second Order with Minmod at different times.

As expected, the second order scheme with flux limiter produced the best results. First Order Upwind with Entropy Fix and Engquist-Osher both gave the correct behaviour, but Lax-Friedrichs displayed too much diffusion, causing it to lose much of the shape definition.

Figure 6.4 shows the analytic solution compared to Second Order with Minmod for the half curve test case, as again the second order scheme produced the best results. This gives confidence that we can apply the second order scheme to real data, which we do in Chapter 8. First however, we look at the implementation of numerical schemes to systems in the next chapter.

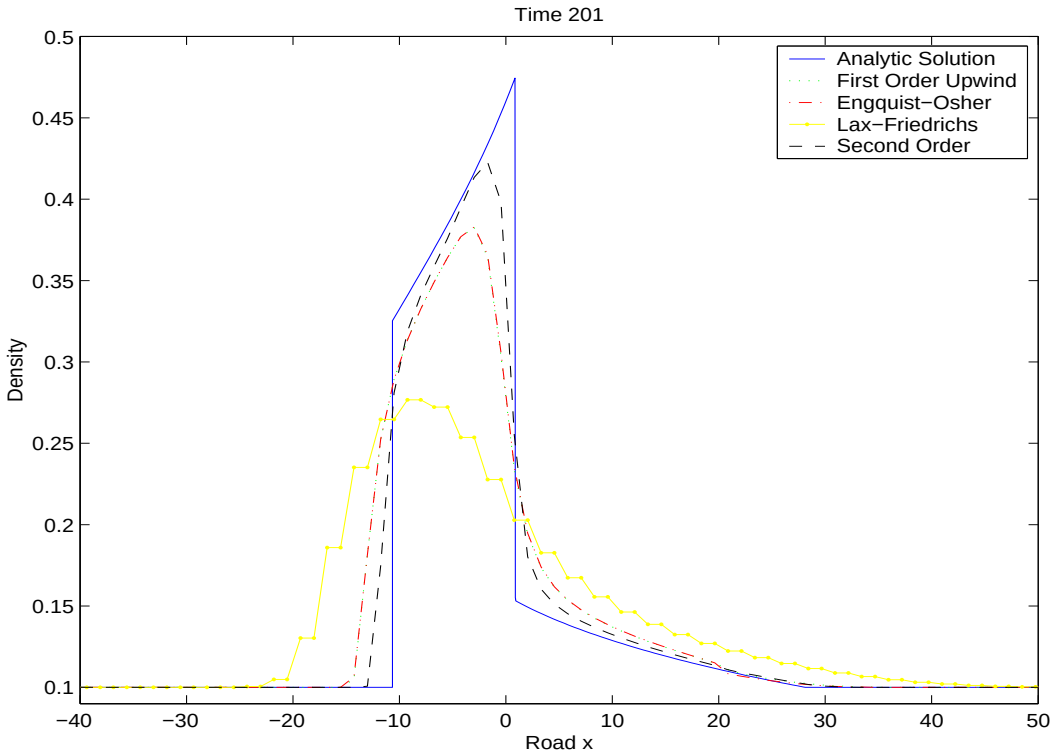

Figure 6.2: Comparison of 4 different schemes at a given time for square wave test problem.

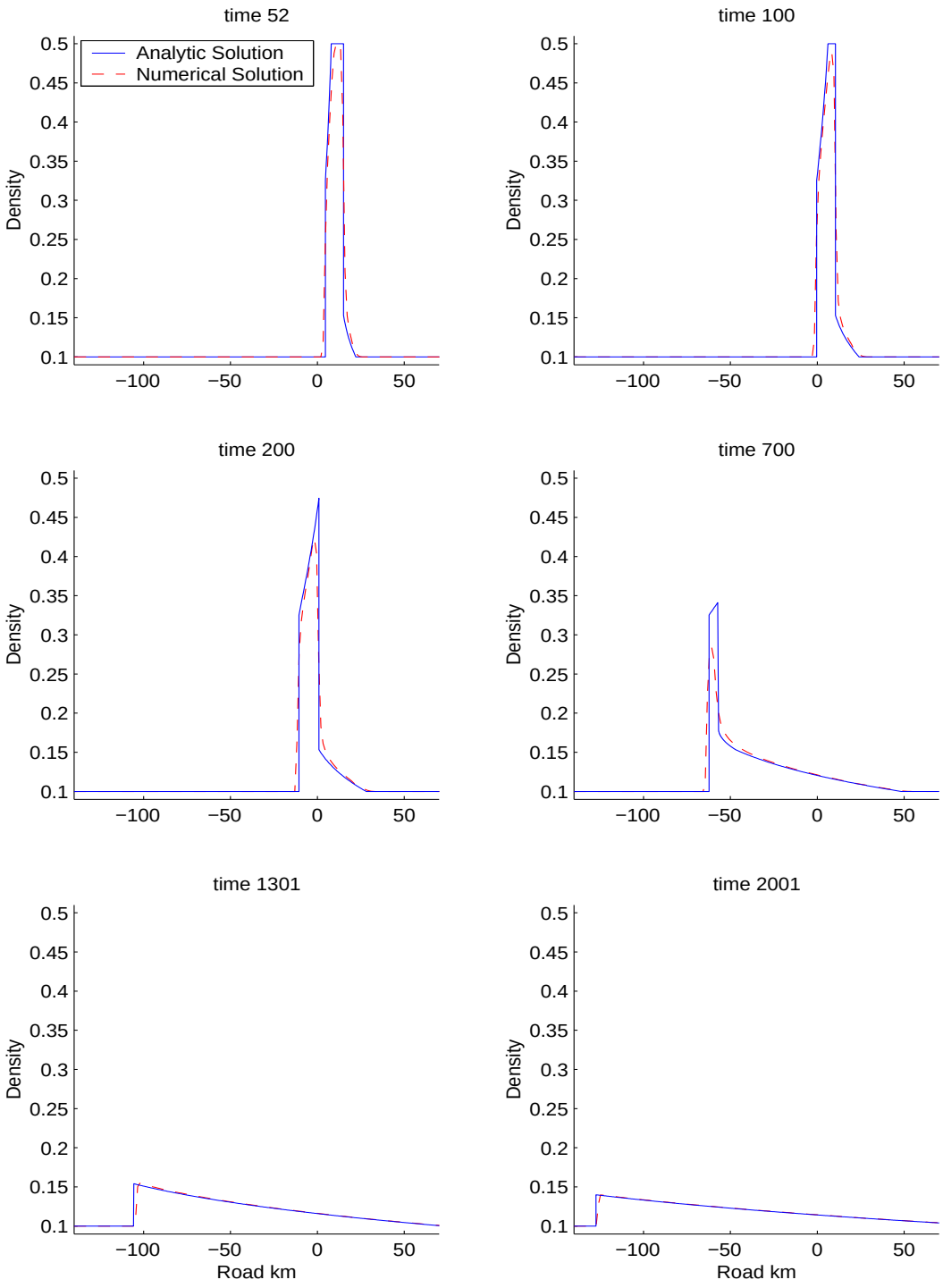

Figure 6.3: Analytic solution compared to numerical solution using Second Order with Minmod for the square wave test problem, using a coarse grid where $\Delta x = 1.2552$ and $\Delta t = 4.002$.

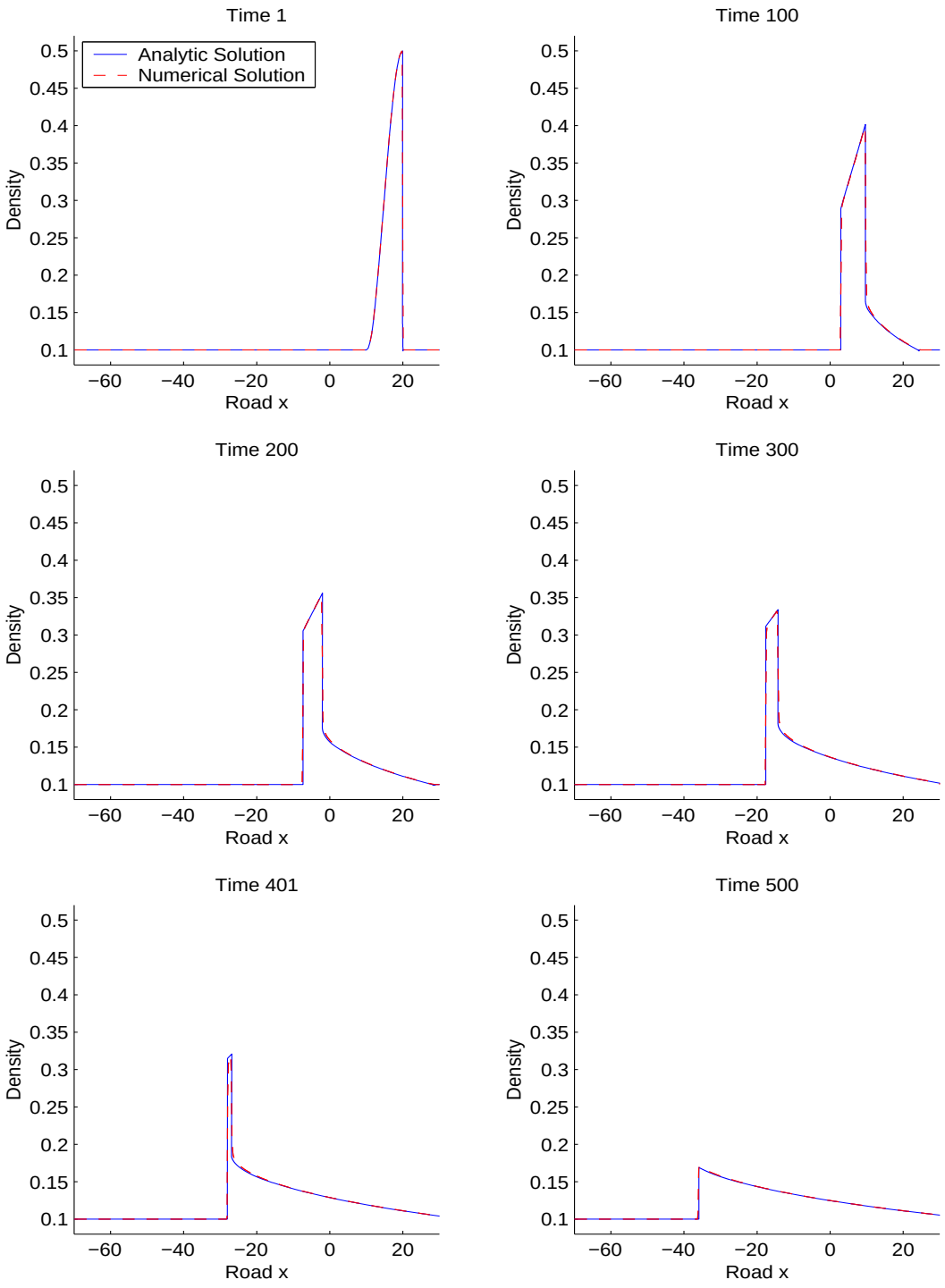

Figure 6.4: Analytic solution compared to numerical solution using Second Order with Minmod for the half curve test problem. $\Delta x = 0.1669$ and $\Delta t = 1.1443$.

Chapter 7

Numerical Methods for Systems

For systems of equations such as the two equation models, we shall implement the first order Lax-Friedrichs scheme as well as upwind schemes based on decomposition. In the latter (Roe) schemes the models are decomposed into component scalar problems and a second order TVD scheme with flux limiters is applied to each. These are a class of schemes for scalar homogeneous equations that ensure spurious oscillations cannot be formed, [11]. Due to the systems considered here not being scalar however, the TVD property is not guaranteed, although oscillations are significantly reduced.

7.1 The Lax-Friedrichs Scheme

For systems such as (5.26), the Lax-Friedrichs scheme is given by

$$\mathbf{u}_j^{n+1} = \frac{1}{2}\left(\mathbf{u}_{j+1}^n + \mathbf{u}_{j-1}^n\right) - \frac{\Delta t}{2\Delta x}\left(\mathbf{f}_{j+1}^n - \mathbf{f}_{j-1}^n\right), \tag{7.1}$$

where j, n are the space and time step indices respectively (c.f. Section 6.4).

The scheme is first order accurate. It is known to smooth out solutions excessively and have a *step* feature, but it is nonetheless useful for getting a rough idea of the behaviour of the system very cheaply. It is conservative and easy to apply.

7.2 Roe's Upwind Scheme

The idea behind Roe's scheme is to take a non-linear system of the form (5.8) and to linearise it locally by approximating the Jacobian matrix $A(\mathbf{u})$ in an interval using Roe

averages [30]. The resulting system can then be decomposed within each interval into its two component waves travelling at approximate speeds given by the eigenvalues of the averaged Jacobian matrix $\tilde{A}(\tilde{\mathbf{u}})$. Subsequently standard scalar upwind schemes can be applied to each component.

7.2.1 Roe Decomposition

Given an interval (x_L, x_R) and any data $\mathbf{u} = \mathbf{u}_R - \mathbf{u}_L$ we can form differences $\Delta\mathbf{u}$, where $\mathbf{u}_R$ is $\mathbf{u}$ to the right of the cell, and $\mathbf{u}_L$ is $\mathbf{u}$ to the left of the cell . We can then find values for α_1 and α_2 such that

$$\Delta\mathbf{u} = \sum_{k=1}^{2} \alpha_k \mathbf{e}_k, \tag{7.2}$$

where $\mathbf{e}_k$ are the eigenvectors of $A(\mathbf{u})$, i.e. project $\Delta\mathbf{u}$ onto the eigenvectors.

For an infinitesimally small difference $\Delta\mathbf{u}$ and a corresponding small $\Delta\mathbf{f}$, using (5.27),

$$\Delta\mathbf{f} = A(\mathbf{u})\Delta\mathbf{u} = \sum_{k=1}^{2} \lambda_k \alpha_k \mathbf{e}_k, \tag{7.3}$$

where $\Delta\mathbf{f} = A(\mathbf{u})\Delta\mathbf{u}$ is referred to as the conservation or shock capturing property.

Equation (7.3) contains $A(\mathbf{u})$ and infinitesimally small differences $\Delta\mathbf{u}$ and $\Delta\mathbf{f}$. As a numerical approximation Roe considers finite differences over discrete intervals (cells) and constructs *average values*, $\tilde{\alpha}$, $\tilde{\lambda}$, $\tilde{\mathbf{e}}$, $\tilde{\rho}$ and $\tilde{v}$, which satisfy discrete versions of (7.2) and (7.3), at least to first order. The details will become clear in the examples below.

Each component (wave) problem ($k = 1, 2$) can then be solved by one of the schemes in Chapter 6 and the results combined to give the full solution.

7.2.2 The Payne-Whitham Model

For the PW model, (7.2) gives

$$\begin{pmatrix} \Delta\rho \\ \Delta\rho v \end{pmatrix} = \alpha_1 \begin{pmatrix} 1 \\ \dfrac{\rho v}{\rho} + C_o \end{pmatrix} + \alpha_2 \begin{pmatrix} 1 \\ \dfrac{\rho v}{\rho} - C_o \end{pmatrix}, \tag{7.4}$$

where Δ now refers to *finite* differences. Solving for α_1 and α_2, we get

$$\alpha_1 = \frac{1}{2}\Delta\rho + \frac{1}{2C_o}\left(\Delta(\rho v) - \frac{\rho v}{\rho}\Delta\rho\right) \tag{7.5}$$

and

$$\alpha_2 = \frac{1}{2}\Delta\rho - \frac{1}{2C_o}\left(\Delta(\rho v) - \frac{\rho v}{\rho}\Delta\rho\right). \tag{7.6}$$

The discrete averages are therefore

$$\tilde{\lambda}_k = \tilde{v} \pm C_o, \tag{7.7}$$

$$\tilde{\alpha}_k = \frac{1}{2}\Delta\rho \pm \frac{1}{2C_0}\left(\Delta(\rho v) - \tilde{v}\Delta\rho\right), \tag{7.8}$$

where the tilde refers to averages yet to be defined, and

$$\tilde{\mathbf{e}}_k = \begin{bmatrix} 1 \\ \tilde{v} \pm C_o \end{bmatrix}, \quad k = 1, 2. \tag{7.9}$$

We now seek Roe averages to the variables ρ and v from (7.3). The first equation of

$$\Delta\mathbf{f} = \tilde{A}\Delta\mathbf{u} \tag{7.10}$$

for the PW model simply gives $\Delta(\rho v) = \Delta(\rho v)$. Roe averages are not unique, Roe [30], therefore chose

$$\tilde{\rho} = \sqrt{\rho_R \rho_L}, \tag{7.11}$$

as a convenient definition for $\tilde{\rho}$, where ρ_R is the value of ρ at the right end of the cell, and ρ_L is the value of ρ at the left end of the cell. $\tilde{v}$ is then found from the second equation of (7.3), which requires

$$\begin{aligned} \Delta f_2 = \Delta\left(\frac{(\rho v)^2}{\rho}\right) + \Delta\left(C_o^2\rho\right) &= \left(\tilde{v}^2 + C_o^2\right)(\tilde{\alpha}_1 + \tilde{\alpha}_2) + 2\tilde{v}C_o(\tilde{\alpha}_1 - \tilde{\alpha}_2) \\ &= \left(\tilde{v}^2 + C_o^2\right)\Delta\rho + 2\tilde{v}\left(\Delta(\rho v) - \tilde{v}\Delta\rho\right) \end{aligned}$$

to hold. This gives a quadratic equation in terms of $\tilde{v}$

$$\tilde{v}^2\Delta\rho - 2\tilde{v}\Delta(\rho v) + \Delta(\rho v^2) = 0,$$

and expanding out $\Delta(.) = (.)_R - (.)_L$ gives

$$\frac{(\rho_R v_R - \rho_L v_L) \pm \sqrt{(\rho_R v_R - \rho_L v_L)^2 - (\rho_R - \rho_L)(\rho_R v_R^2 - \rho_L v_L^2)}}{(\rho_R - \rho_L)}.$$

Taking the positive root then leads to

$$\tilde{v} = \frac{\left(\sqrt{\rho_R}v_R + \sqrt{\rho_L}v_L\right)}{\left(\sqrt{\rho_R} + \sqrt{\rho_L}\right)} \tag{7.12}$$

(see [8] for details).

7.2.3 The Berg-Mason-Woods Model

To find $\alpha_{1,2}$ we use (7.2). This gives

$$\begin{pmatrix} \Delta\rho \\ \Delta\rho v \end{pmatrix} = \alpha_1 \begin{pmatrix} 1 \\ v + \sqrt{-\frac{V'(\rho)}{2\tau}} \end{pmatrix} + \alpha_2 \begin{pmatrix} 1 \\ v - \sqrt{-\frac{V'(\rho)}{2\tau}} \end{pmatrix},$$

and the Roe averages of $\tilde{\alpha}_{1,2}$, are found in the same way as for PW. This gives

$$\begin{aligned} \tilde{\alpha}_1 &= \frac{\Delta\rho v - \tilde{v}\Delta\rho + \Delta\rho\sqrt{-\frac{\widetilde{V'(\rho)}}{2\tau}}}{2\sqrt{-\frac{\widetilde{V'(\rho)}}{2\tau}}}, \\ \tilde{\alpha}_2 &= \frac{\Delta\rho\sqrt{-\frac{\widetilde{V'(\rho)}}{2\tau}} - \Delta\rho v + \tilde{v}\Delta\rho}{2\sqrt{-\frac{\widetilde{V'(\rho)}}{2\tau}}}. \end{aligned} \tag{7.13}$$

To find the Roe averages $\tilde{v}$ and $\widetilde{V'(\rho)}$, using (7.10) we have that $\Delta(\rho v) = \Delta(\rho v)$ as with the PW model. The second equation however, gives

$$\Delta\left(\frac{(\rho v)^2}{\rho}\right) - \frac{1}{2\tau}\Delta(V(\rho)) = -\tilde{v}^2\Delta\rho - \frac{1}{2\tau}\widetilde{V'(\rho)}\Delta\rho + 2\tilde{v}\Delta(\rho v), \tag{7.14}$$

which can be separated into two equations, namely

$$\tilde{v}^2\Delta\rho - 2\tilde{v}\Delta(\rho v) + \Delta(\rho v^2) = 0 \tag{7.15}$$

and

$$\frac{1}{2\tau}\widetilde{V'(\rho)}\Delta\rho - \frac{1}{2\tau}\Delta V(\rho) = 0. \tag{7.16}$$

It is easily seen from (7.16) that

$$\widetilde{V'(\rho)} = \frac{\Delta V(\rho)}{\Delta\rho}, \tag{7.17}$$

and that (7.15) is the same as the quadratic obtained for $\tilde{v}$ for the PW model, $\tilde{v}$ for the BMW is therefore

$$\tilde{v} = \frac{\left(\sqrt{\rho_R}v_R + \sqrt{\rho_L}v_L\right)}{\left(\sqrt{\rho_R} + \sqrt{\rho_L}\right)}$$

.

7.2.4 The Aw-Rascle Model

We use (7.2) to find $\alpha_{1,2}$, where

$$\begin{pmatrix} \Delta\rho \\ \Delta y \end{pmatrix} = \alpha_1 \begin{pmatrix} 1 \\ v + (\gamma+1)P \end{pmatrix} + \alpha_2 \begin{pmatrix} 1 \\ v + P \end{pmatrix},$$

and the Roe averages $\tilde{\alpha}_{1,2}$, for the Aw-Rascle model are found in the same way as before. This gives

$$\begin{aligned} \tilde{\alpha}_1 &= \frac{\Delta y - (\tilde{v} + \tilde{P})\Delta\rho}{\gamma\tilde{P}}, \\ \tilde{\alpha}_2 &= \frac{\left(\tilde{v} + (\gamma+1)\tilde{P}\right)\Delta\rho - \Delta y}{\gamma\tilde{P}}. \end{aligned} \tag{7.18}$$

Now we need to find the Roe averages $\tilde{v}$ and $\tilde{P}$. Using (7.10) we have that

$$\Delta\left(y - \rho P\right) = -(\gamma+1)\tilde{P}\Delta\rho + \Delta y, \tag{7.19}$$

and

$$\Delta\left(\frac{y^2}{\rho} - Py\right) = -\left(\tilde{v}^2 + (\gamma+2)\tilde{P}\tilde{v} + (\gamma+1)\tilde{P}^2\right)\Delta\rho + (2\tilde{v} + \tilde{P})\Delta y. \tag{7.20}$$

It is easily seen from (7.19) that

$$\tilde{P} = \frac{\Delta\rho P}{(\gamma+1)\Delta\rho} \tag{7.21}$$

satisfies (7.10). Finding Roe averages for $\tilde{v}$ from (7.20) involves rewriting (7.20) as

$$a\tilde{v}^2 + b\tilde{v} + c = 0 \tag{7.22}$$

where

$$\begin{aligned} a &= \Delta\rho, \\ b &= (\gamma+2)\tilde{P}\Delta\rho - 2\Delta y, \\ c &= \Delta\left(\frac{y^2}{\rho} - Py\right) + (\gamma+1)\tilde{P}^2\Delta\rho - \tilde{P}\Delta y. \end{aligned}$$

$\tilde{v}$ can then be found using the quatratic formula

$$\tilde{v} = \frac{2c}{-b \mp \sqrt{b^2 - 4ac}}. \tag{7.23}$$

The Roe averages in each cell must lie between the values at the nodes at either end of the cell. This decides which root to take for (7.23).

7.2.5 The Zhang Model

For the Zhang model, (7.2) gives

$$\begin{pmatrix} \Delta\rho \\ \Delta w \end{pmatrix} = \alpha_1 \begin{pmatrix} 1 \\ v - V(\rho) - \rho V'(\rho) \end{pmatrix} + \alpha_2 \begin{pmatrix} 1 \\ v - V(\rho) \end{pmatrix}. \tag{7.24}$$

Solving for α_1 and α_2, we get

$$\begin{aligned} \tilde{\alpha_1} &= \frac{\left(\tilde{v} - \widetilde{V(\rho)}\right)\Delta\rho - \Delta w}{\tilde{\rho}\widetilde{V'(\rho)}}, \\ \tilde{\alpha_2} &= \frac{\left(\tilde{\rho}\widetilde{V'(\rho)} - \tilde{v} + \widetilde{V(\rho)}\right)\Delta\rho + \Delta w}{\tilde{\rho}\widetilde{V'(\rho)}}. \end{aligned} \tag{7.25}$$

Roe averages are obtained from (7.10) as before. The first component gives

$$\tilde{\rho}\widetilde{V'(\rho)} + \widetilde{V(\rho)} = \frac{\Delta(\rho V(\rho))}{\Delta\rho}, \tag{7.26}$$

which is purely in terms of functions of ρ. We can therefore use Newton iteration on (7.26) to obtain a Roe average for $\tilde{\rho}$, where

$$F = \rho V'(\rho) + V(\rho) - \frac{\Delta(\rho V(\rho))}{\Delta\rho},$$

and

$$\frac{dF}{d\rho} = \rho V''(\rho) + 2V'(\rho),$$

$\tilde{\rho}$ is then calculated from (4.17). $\widetilde{V(\rho)}$ and $\widetilde{V'(\rho)}$ are taken to be $V(\tilde{\rho})$ and $V'(\tilde{\rho})$ respectively.

The second component gives

$$\Delta\left(\frac{w^2}{\rho} + wV(\rho)\right) = \left(-\frac{\tilde{w}^2}{\tilde{\rho}^2} + \tilde{w}V'(\tilde{\rho})\right)\Delta\rho + \left(\frac{2\tilde{w}}{\tilde{\rho}} + V(\tilde{\rho})\right)\Delta w,$$

where $w = \rho(v - V(\rho))$. Hence writing this as a quadratic in terms of v first we have

$$\begin{aligned} \Delta\left(\frac{w^2}{\rho} + wV(\rho)\right) &= \frac{\tilde{w}}{\tilde{\rho}}\left(-\frac{\tilde{w}}{\tilde{\rho}} + \tilde{\rho}V'(\tilde{\rho})\right)\Delta\rho + (2(\tilde{v} - V(\tilde{\rho})) + V(\tilde{\rho}))\,\Delta w, \\ &= (\tilde{v} - V(\tilde{\rho}))\left(-\tilde{v} + \frac{\Delta(\rho V(\rho))}{\Delta\rho}\right)\Delta\rho + (2\tilde{v} - V(\tilde{\rho}))\Delta w, \end{aligned}$$

using (7.26), giving

$$\tilde{v}^2\Delta\rho + \tilde{v}\left(-\Delta(\rho V(\rho)) - V(\tilde{\rho})\Delta\rho - 2\Delta w\right) + V(\tilde{\rho})\Delta(\rho V(\rho)) + V(\tilde{\rho})\Delta w - \Delta\left(\frac{w^2}{\rho} + wV(\rho)\right).$$

Hence,

$$\begin{aligned} a &= \Delta\rho, \\ b &= -\Delta(\rho V(\rho)) - V(\tilde{\rho})\Delta\rho - 2\Delta w, \\ c &= V(\tilde{\rho})\Delta(\rho V(\rho)) + V(\tilde{\rho})\Delta w - \Delta\left(\frac{w^2}{\rho} + wV(\rho)\right), \end{aligned}$$

as in (7.22), with solution (7.23).

However, solving for $\tilde{v}$ in this way doesn't always give real solutions. Fortunately, we are able to take advantage of the structure of the flux function $\mathbf{f}(\mathbf{u})$ to give an alternative method for finding Roe averages.

7.2.6 Alternative Way of Finding Averages

Roe averages need not be unique. It is possible to take advantage of the special structure of both the Aw-Rascle and Zhang models in order to find alternative averages. The flux functions can both be written as

$$\mathbf{f} = v\mathbf{u} = v\begin{pmatrix} u_1 \\ u_2 \end{pmatrix}, \tag{7.27}$$

then

$$\begin{aligned} A &= \frac{\partial \mathbf{f}}{\partial \mathbf{u}} = \frac{\partial(v\mathbf{u})}{\partial \mathbf{u}} \\ &= \begin{pmatrix} \frac{\partial}{\partial u_1}(vu_1) & \frac{\partial}{\partial u_2}(vu_1) \\ \frac{\partial}{\partial u_1}(vu_2) & \frac{\partial}{\partial u_2}(vu_2) \end{pmatrix}, \\ &= \begin{pmatrix} \frac{\partial v}{\partial u_1}u_1 + v & u_1\frac{\partial v}{\partial u_2} \\ u_2\frac{\partial v}{\partial u_1} & \frac{\partial v}{\partial u_2}u_2 + v \end{pmatrix}. \end{aligned} \tag{7.28}$$

Now, (7.10) may be written as

$$\tilde{A}\Delta\mathbf{u} = \Delta\mathbf{f} = \Delta(v\mathbf{u}) = \bar{v}\Delta\mathbf{u} + \bar{u}\Delta v, \tag{7.29}$$

where $\bar{v}$ is the mean value of v etc. We also note that

$$\tilde{A}\Delta\mathbf{u} = \begin{pmatrix} \tilde{u}_1\widetilde{\frac{\partial v}{\partial u_1}} & \tilde{u}_1\widetilde{\frac{\partial v}{\partial u_2}} \\ \tilde{u}_2\widetilde{\frac{\partial v}{\partial u_1}} & \tilde{u}_2\widetilde{\frac{\partial v}{\partial u_2}} \end{pmatrix}\Delta\mathbf{u} + \tilde{v}\Delta\mathbf{u}. \tag{7.30}$$

If we now set $\tilde{v} = \bar{v}$, $\tilde{u}_1 = \bar{u}_1$ and $\tilde{u}_2 = \bar{u}_2$, then from (7.29)

$$\begin{pmatrix} \bar{u}_1 \widetilde{\frac{\partial v}{\partial u_1}} & \bar{u}_1 \widetilde{\frac{\partial v}{\partial u_2}} \\ \bar{u}_2 \widetilde{\frac{\partial v}{\partial u_1}} & \bar{u}_2 \widetilde{\frac{\partial v}{\partial u_2}} \end{pmatrix} \Delta \mathbf{u} = \bar{\mathbf{u}} \Delta v,$$

and provided $\bar{u_1}$, $\bar{u_2} \neq 0$,

$$\widetilde{\frac{\partial v}{\partial u_1}} \Delta u_1 + \widetilde{\frac{\partial v}{\partial u_2}} \Delta u_2 = \Delta v. \tag{7.31}$$

Making the observation that the element $A_{1,2} = 1$ for both models (see (5.27), (5.36)), we can deduce

$$\bar{u}_1 \widetilde{\frac{\partial v}{\partial u_2}} = 1$$

and therefore

$$\widetilde{\frac{\partial v}{\partial u_2}} = \frac{1}{\bar{u}_1}, \tag{7.32}$$

and hence from (7.31)

$$\widetilde{\frac{\partial v}{\partial u_1}} = \frac{\Delta v}{\Delta u_1} - \frac{\Delta u_2}{\bar{u}_1 \Delta u_1}. \tag{7.33}$$

If we now write v explicitly as a function of $\mathbf{u}$, find $\widetilde{\frac{\partial v}{\partial u_1}}$ and compare the elements $\tilde{A}_{2,1}$, we can obtain one average. The final average is then determined by comparing the $\tilde{A}_{1,1}$ elements.

Aw-Rascle Model

Starting with $y = \rho(v + P(\rho))$ and hence $v = \frac{y}{\rho} - P(\rho)$, the first derivative is given by

$$\frac{\partial v}{\partial \rho} = -\frac{y}{\rho^2} - P'(\rho),$$

therefore,

$$-\frac{\bar{y}}{\bar{\rho}^2} - \tilde{P}'(\rho) = \frac{\Delta v}{\Delta \rho} - \frac{\Delta y}{\bar{\rho} \Delta \rho},$$

i.e.

$$\tilde{P}'(\rho) = \frac{\Delta y}{\bar{\rho} \Delta \rho} - \frac{\Delta v}{\Delta \rho} - \frac{\bar{y}}{\bar{\rho}^2}. \tag{7.34}$$

Now,

$$A(1,1) = \rho \frac{\partial v}{\partial \rho} + \frac{y}{\rho} - P(\rho)$$

therefore, comparing the elements $\tilde{A}_{1,1}$ yields

$$\frac{\bar{y}}{\bar{\rho}} - \tilde{P}(\rho) = \bar{v}$$

i.e.

$$\tilde{P}(\rho) = \frac{\bar{y}}{\bar{\rho}} - \bar{v}. \tag{7.35}$$

The eigenvalues, eigenvectors and $\tilde{\alpha}$'s are written in terms of $P'(\rho)$ and $P(\rho)$ (rather than letting $P'(\rho) = \gamma\rho P(\rho)$), hence

$$\tilde{\lambda}_1 = \tilde{v}, \quad \tilde{\lambda}_2 = \tilde{v} - \tilde{\rho}\tilde{P}'(\rho),$$

$$\mathbf{e_1} = \begin{pmatrix} 1 \\ \tilde{v} + \tilde{P}(\rho) + \tilde{\rho}\tilde{P}'(\rho) \end{pmatrix}, \quad \mathbf{e_2} = \begin{pmatrix} 1 \\ \tilde{v} + \tilde{P} \end{pmatrix},$$

and

$$\tilde{\alpha}_1 = \frac{\Delta y - (\tilde{v} + \tilde{P})\Delta\rho}{\tilde{\rho}\tilde{P'(\rho)}},$$

$$\tilde{\alpha}_2 = \frac{\left(\tilde{v} + \tilde{P} + \tilde{\rho}\tilde{P}'(\rho)\right)\Delta\rho - \Delta y}{\tilde{\rho}\tilde{P'(\rho)}}.$$

Roe's Decomposition can then be applied.

Zhang Model

Similarly, for the Zhang model, $w = \rho(v - V(\rho))$, hence $v = \frac{w}{\rho} + V(\rho)$, therefore

$$\frac{\partial v}{\partial \rho} = -\frac{w}{\rho^2} + V'(\rho).$$

Comparing elements $\tilde{A}_{2,1}$ gives

$$-\frac{\bar{w}}{\bar{\rho}^2} + \widetilde{V}'(\rho) = \frac{\Delta v}{\Delta\rho} - \frac{\Delta w}{\bar{\rho}\Delta\rho},$$

and hence

$$\widetilde{V}'(\rho) = \frac{\Delta v}{\Delta\rho} - \frac{\Delta w}{\bar{\rho}\Delta\rho} + \frac{\bar{w}}{\bar{\rho}^2}. \tag{7.36}$$

Finally, by comparing elements $\tilde{A}_{1,1}$ we have

$$\bar{\rho}\widetilde{\frac{\partial v}{\partial \rho}} + \frac{\bar{w}}{\bar{\rho}} + \widetilde{V}(\rho) = \bar{\rho}\widetilde{\frac{\partial v}{\partial \rho}} + \bar{v},$$

i.e.

$$\widetilde{V}(\rho) = \bar{v} - \frac{\bar{w}}{\bar{\rho}}. \tag{7.37}$$

We are now ready to apply Roe's scheme.

7.2.7 Roe Decomposition with First Order Upwind Scheme

Once we have found the Roe averages we can implement the scheme component by component, in the same way as the First Order Upwind scheme (see Chapter 6). The values of $\mathbf{u}$ at the new time step are equal to the old ones plus the addition of

$$\tilde{\boldsymbol{\psi}}_k = -\frac{\Delta t}{\Delta x}\tilde{\lambda}_k\tilde{\alpha}_k\tilde{\mathbf{e}}_k \begin{cases} to \quad \mathbf{u}_{j+1} \quad if \quad \tilde{\lambda}_k > 0, \quad or \\ to \quad \mathbf{u}_j \quad\;\; if \quad \tilde{\lambda}_k < 0, \end{cases} \tag{7.38}$$

for k =1, 2 (Compare to Section 6.1).

7.2.8 Roe Decomposition with Second Order Schemes

A second step may be applied after First Order Upwind to give the scheme second order accuracy, as in Section 6.5.

If $\tilde{\lambda}_k > 0$

$$\left.\begin{aligned} \mathbf{u}_j^n &\rightarrow \mathbf{u}_j^{n*} + \frac{1}{2}\left(1 - \left|\tilde{\lambda}_k\frac{\Delta t}{\Delta x}\right|\right)\tilde{\boldsymbol{\psi}}_k, \\ \mathbf{u}_{j+1}^n &\rightarrow \mathbf{u}_{j+1}^{n*} - \frac{1}{2}\left(1 - \left|\tilde{\lambda}_k\frac{\Delta t}{\Delta x}\right|\right)\tilde{\boldsymbol{\psi}}_k, \end{aligned}\right\} \tag{7.39}$$

else if $\tilde{\lambda}_k < 0$

$$\left.\begin{aligned} \mathbf{u}_j^n &\rightarrow \mathbf{u}_j^{n*} - \frac{1}{2}\left(1 - \left|\tilde{\lambda}_k\frac{\Delta t}{\Delta x}\right|\right)\tilde{\boldsymbol{\psi}}_k, \\ \mathbf{u}_{j+1}^n &\rightarrow \mathbf{u}_{j+1}^{n*} + \frac{1}{2}\left(1 - \left|\tilde{\lambda}_k\frac{\Delta t}{\Delta x}\right|\right)\tilde{\boldsymbol{\psi}}_k, \end{aligned}\right\} \tag{7.40}$$

where $\mathbf{u}_j^{n*}$ is the solution $\mathbf{u}_j^n$ after First Order Upwind has been applied. For each separate k this is equivalent to the Lax-Wendroff scheme.

7.2.9 Use of Flux Limiters

As for scalar equations, one of the drawbacks of second order schemes is the appearance of oscillations near shocks. The second order step of a scheme overcompensates for the diffusive nature of a first order step. We therefore add an extra feature which is designed to prevent these oscillations, namely a Flux Limiter $\boldsymbol{\phi}_j$. As in Section 6.6, the Minmod Flux Limiter replaces $\tilde{\boldsymbol{\psi}}_k$ in the second step above. If the *first components* of

$$\tfrac{1}{2}\left(1 - \left|\tilde{\lambda}_k\tfrac{\Delta t}{\Delta x}\right|\right)\tilde{\boldsymbol{\psi}}_k, \quad \tfrac{1}{2}\left(1 - \left|\tilde{\lambda}_{upwind}\tfrac{\Delta t}{\Delta x}\right|\right)\tilde{\boldsymbol{\psi}}_{upwind}$$

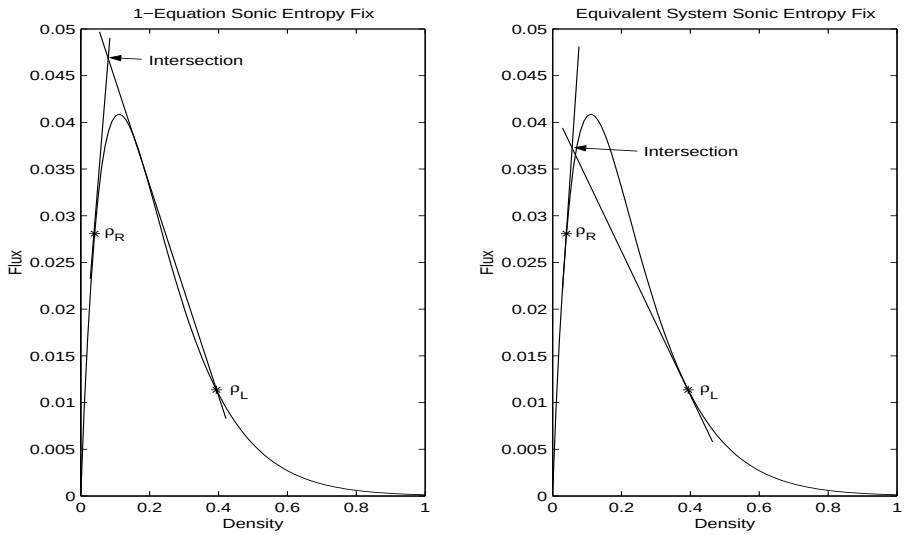

Figure 7.1: The left diagram shows the intersection point used to determine the fluxes when using the sonic entropy fix for a one-equation model. The right diagram shows the intersection point used when applying the equivalent sonic entropy fix method for systems.

are of opposite signs, then $\tilde{\boldsymbol{\phi}}_k = 0$. If not, consider the absolute values. If the first components satisfy

$$\left|\frac{1}{2}\left(1 - \left|\tilde{\lambda}_k \frac{\Delta t}{\Delta x}\right|\right)\tilde{\boldsymbol{\psi}}_k\right| < \left|\frac{1}{2}\left(1 - \left|\tilde{\lambda}_{upwind} \frac{\Delta t}{\Delta x}\right|\right)\tilde{\boldsymbol{\psi}}_{upwind}\right|$$

then $\tilde{\boldsymbol{\phi}}_k = \tilde{\boldsymbol{\psi}}_k$, otherwise $\tilde{\boldsymbol{\phi}}_k = \tilde{\boldsymbol{\psi}}_{upwind}$.

The second stage is then applied as with (7.39) and (7.40), but with $\tilde{\boldsymbol{\phi}}_k$ replacing $\tilde{\boldsymbol{\psi}}_k$.

So if $\tilde{\lambda}_k > 0$

$$\left.\begin{aligned} \mathbf{u}_j^n &\rightarrow \mathbf{u}_j^{n*} + \frac{1}{2}\left(1 - \left|\tilde{\lambda}_k \frac{\Delta t}{\Delta x}\right|\right)\tilde{\boldsymbol{\phi}}_k, \\ \mathbf{u}_{j+1}^n &\rightarrow \mathbf{u}_{j+1}^{n*} - \frac{1}{2}\left(1 - \left|\tilde{\lambda}_k \frac{\Delta t}{\Delta x}\right|\right)\tilde{\boldsymbol{\phi}}_k, \end{aligned}\right\} \tag{7.41}$$

else if $\tilde{\lambda}_k < 0$

$$\left.\begin{aligned} \mathbf{u}_j^n &\rightarrow \mathbf{u}_j^{n*} - \frac{1}{2}\left(1 - \left|\tilde{\lambda}_k \frac{\Delta t}{\Delta x}\right|\right)\tilde{\boldsymbol{\phi}}_k, \\ \mathbf{u}_{j+1}^n &\rightarrow \mathbf{u}_{j+1}^{n*} + \frac{1}{2}\left(1 - \left|\tilde{\lambda}_k \frac{\Delta t}{\Delta x}\right|\right)\tilde{\boldsymbol{\phi}}_k. \end{aligned}\right\} \tag{7.42}$$

7.2.10 Sonic Entropy Fix for Systems

As with the one-equation model, systems may also require a sonic entropy fix when applying a first order upwind scheme. Here, however, after decomposing the system

into its component waves we no longer have a flux function in terms of one variable only as with the one-equation case, since it is a system that has been linearised for the calculation of Roe averages. We cannot therefore, as in the one-equation case, simply check if ρ_L and ρ_R are on opposite sides of the sonic point. Before, if this was the case, we used the intersection of the two tangents from ρ_L and ρ_R as the split point, see Figure 7.1 (left). With systems we check if the wavespeeds are such that $\lambda_L > \lambda_R$. If so then the entropy condition (4.11) tells us this is a shock as before, but if it is not satisfied then we apply a sonic entropy fix regardless of where ρ_L and ρ_R are relative to any *sonic points*. This is to ensure that fans disperse correctly. It is applied to each cell for each wave as follows:

The wavespeeds are calculated at the left and right nodes of the cell using the eigenvalues of the system, λ. These λ_L and λ_R are then compared to the cell average wavespeed $\tilde{\lambda}$. Set

$$\begin{aligned} \nu_L &= min(\tilde{\lambda}, \lambda_L) \\ \nu_R &= max(\tilde{\lambda}, \lambda_R). \end{aligned}$$

Then, if $\lambda_L \geq \tilde{\lambda} \geq \lambda_R$, i.e. (4.11) is satisfied, there is a shock and

$$\nu_L = \tilde{\lambda}\frac{\Delta t}{\Delta x}, \quad \nu_R = \tilde{\lambda}\frac{\Delta t}{\Delta x}, \tag{7.43}$$

i.e.

$$\nu_L = \nu_R,$$

and the sonic entropy fix is not required.

If, however, the entropy condition is not satisfied, i.e. $\lambda_L \leq \tilde{\lambda} \leq \lambda_R$, then

$$\nu_L = \lambda_L\frac{\Delta t}{\Delta x}, \quad \nu_R = \lambda_R\frac{\Delta t}{\Delta x} \quad \text{and} \quad \nu_c = \tilde{\lambda}\frac{\Delta t}{\Delta x}, \tag{7.44}$$

and a sonic entropy fix is required.

The flux from the cell is then shared between the left and right nodes. This is implemented using

$$pos(z) = \frac{z + |z|}{2},$$

i.e.,

$$pos(z) = \begin{cases} z & \text{if } z \geq 0 \\ 0 & \text{if } z < 0. \end{cases} \tag{7.45}$$

The left and right fluxes are then calculated using

$$\begin{aligned}\phi_L &= [pos(-\nu_R)(\nu_C - \nu_L) + pos(-\nu_L)(\nu_R - \nu_C)]\,\frac{\tilde{\alpha}}{(\nu_R - \nu_L)},\\ \phi_R &= -[pos(\nu_R)(\nu_C - \nu_L) + pos(\nu_L)(\nu_R - \nu_C)]\,\frac{\tilde{\alpha}}{(\nu_R - \nu_L)},\end{aligned} \tag{7.46}$$

where $\tilde{\alpha}$ is as calculated previously, (7.8), (7.18) and (7.25). These fluxes are then used in place of $\tilde{\boldsymbol{\psi}}$, (7.38), when applying first order upwind schemes, [33].

What this method doesn't take into account is that if there is a non convex flux function. It is equivalent in the one-equation case to finding the intersection of the two tangents from ρ_L and ρ_R, (see Figure 7.1 right) rather than the intersection of the tangent from ρ_R and the line from ρ_L that makes a tangent to the flux function, (see Figure 7.1 left). The method is, however, equivalent if the flux function is convex/concave. Because decomposition is a local linearisation, although this is only an approximation it is adequate for these purposes.

7.3 Boundary Conditions and Characteristic Variables

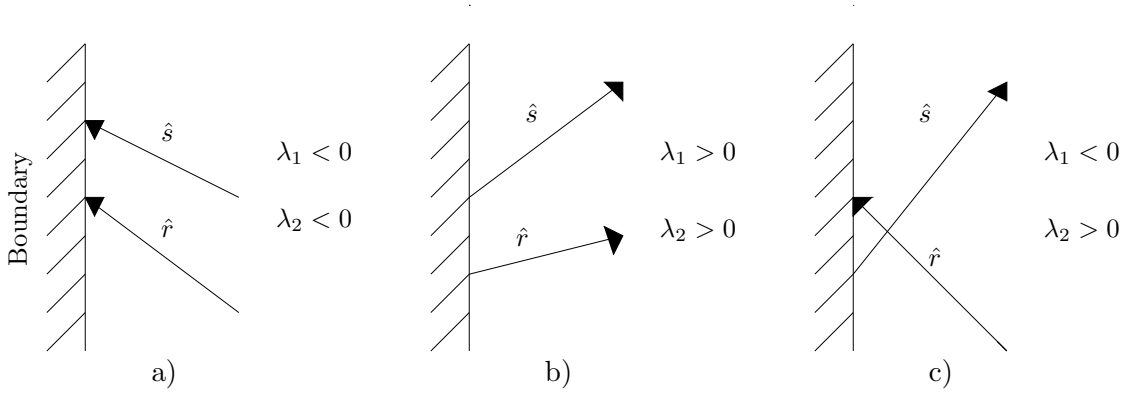

Figure 7.2: When to use boundary data.

The question remains of what to do at the boundaries. As discussed in Chapter 2, for a well posed problem along with initial data, boundary data is required only when the waves are moving into the domain from the boundary. If both wave speeds $\lambda_{1,2}$ are of the same sign at the boundary, then the waves are either both going into, or both coming out of the boundary. If they are both going into the boundary then there

is no need for boundary data (Figure 7.2a). Indeed, if boundary data was supplied the problem would be over prescribed as the conditions are determined from inside the domain, by the waves moving into the boundary. If both of the waves are coming out of the boundary, then we must impose two boundary conditions, say both density and velocity (from the M25 data supplied) (Figure 7.2b). If the wave speeds are of opposite signs, however, then we should only supply the data for the wave coming into the region (see Figure 7.2c). This can be done by splitting the system up into its component waves using diagonalisation.

Taking the system in the form of (5.8), having found the eigenvalues $\lambda_{1,2}$, and eigenvectors $\mathbf{e}_{1,2}$, we construct a matrix X whose columns are the eigenvectors of A together with a diagonal matrix Λ whose entries are the corresponding eigenvalues. Premultiplying (5.8) by X^{-1} and using $XX^{-1} = I$, we get

$$X^{-1}\mathbf{u}_t + X^{-1}AXX^{-1}\mathbf{u}_x = \mathbf{0}. \tag{7.47}$$

Substituting for $X^{-1}AX = \Lambda$ and defining

$$\hat{\mathbf{r}}_t = X^{-1}\mathbf{u}_t, \quad \hat{\mathbf{r}}_x = X^{-1}\mathbf{u}_x, \tag{7.48}$$

where

$$\hat{\mathbf{r}} = \begin{pmatrix} \hat{r} \\ \hat{s} \end{pmatrix},$$

we are able to integrate (7.48) and hence express $\hat{r}$ and $\hat{s}$ explicitly in terms of the conserved variables $\mathbf{u}$. Using this transformation, the system can therefore be expressed as

$$\hat{\mathbf{r}}_t + \Lambda\hat{\mathbf{r}}_x = \mathbf{0} \tag{7.49}$$

which has separated the system into two non-linear scalar advection equations in $\hat{r}$ and $\hat{s}$. These are called the characteristic variables as they are constant along the characteristics $dx/dt = \lambda_{1,2}$ respectively.

Consider the case when $\lambda_1 < 0$ and $\lambda_2 > 0$ (Figure 7.3) at the left hand boundary, where the direction of flow is from left to right. $\hat{r}$ is coming into the boundary at P, so is found by tracing back the characteristic to time n, into the cell between nodes 1 and 2. $\hat{s}$ is coming out of the boundary at P, so is calculated from the collected M25 data $\mathbf{u}_B^{n+1}$. Once $\hat{r}$ and $\hat{s}$ are known we can calculate $\mathbf{u}^{n+1}$ at the point P by

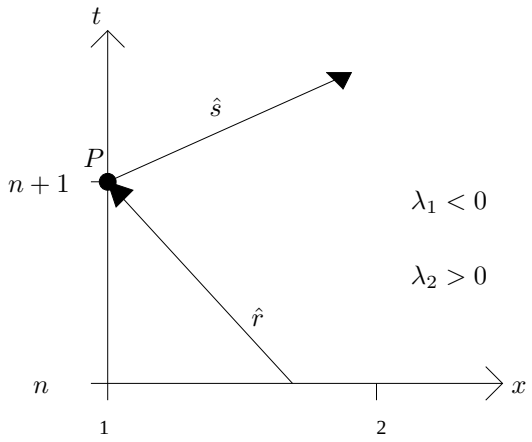

Figure 7.3: Deciding what data to use to calculate Characteristic Variables, depending on direction of flow of the two component waves.

rearranging the solution found by integrating (7.48). Alternatively when $\lambda_1 > 0$ and $\lambda_2 < 0$, $\hat{r}$ is calculated from the boundary data $\mathbf{u}_B^{n+1}$ and $\hat{s}$ is found by tracing back the characteristic into the cell.

7.3.1 Characteristic Variables for the Payne-Whitham Model

Applying (7.48) and (7.49) to the Payne-Whitham model, we have that

$$X = \begin{pmatrix} 1 & 1 \\ v + C_0 & v - C_0 \end{pmatrix}, \quad X^{-1} = \frac{-1}{2C_0} \begin{pmatrix} v - C_0 & -1 \\ -(v + C_0) & 1 \end{pmatrix}, \tag{7.50}$$

and

$$\Lambda = \begin{pmatrix} \lambda_1 & 0 \\ 0 & \lambda_2 \end{pmatrix} = \begin{pmatrix} v + C_0 & 0 \\ 0 & v - C_0 \end{pmatrix}.$$

From (7.48) we have that

$$\begin{aligned} \hat{r}_t &= -\frac{1}{2C_0}(v - C_0)\rho_t + \frac{1}{2C_0}(\rho v)_t \\ &= \frac{1}{2C_0}\left(C_0\rho_t + \rho v_t\right) \\ &= \frac{\rho}{2C_0}\left(v_t + C_0(ln\rho)_t\right), \end{aligned} \tag{7.51}$$

and similarly for $\hat{r}_x$. The partial differential equation for $\hat{s}$ is found to be

$$\hat{s}_t = -\frac{\rho}{2C_0}\left(v_t - C_0(ln\rho)_t\right). \tag{7.52}$$

Equations (7.51) and (7.52) cannot be solved explicitly. However we are looking for Characteristic Variables that satisfy (7.49). If we rewrite (7.51) and (7.52) as

$$\hat{\mathbf{r}}_t = M\mathbf{r}_t \tag{7.53}$$

where

$$M = \frac{\rho}{2C_0}\begin{pmatrix} 1 & 0 \\ 0 & -1 \end{pmatrix}$$

and

$$\mathbf{r} = \begin{pmatrix} r \\ s \end{pmatrix} = \begin{pmatrix} v + C_0 ln(\rho) \\ v - C_0 ln(\rho) \end{pmatrix}, \tag{7.54}$$

then substituting (7.53) into (7.49) we have that

$$M\left(\mathbf{r}_t + \Lambda\mathbf{r}_x\right) = \mathbf{0},$$

since M is diagonal, and provided $\rho \neq 0$ M is invertible, hence

$$\mathbf{r}_t + \Lambda\mathbf{r}_x = \mathbf{0},$$

and the components of $\mathbf{r}$ in (7.54) are the Characteristic Variables with wavespeeds $\lambda_{1,2}$ respectively.

Considering the case when $\lambda_1 < 0$ and $\lambda_2 > 0$ (Figure 7.3) we calculate r by tracing back the characteristic to the previous time step into the cell between nodes 1 and 2, and take a linear interpolation between $\mathbf{u}_1$ and $\mathbf{u}_2$ to find the corresponding $\mathbf{u}_I$. r is then calculated using $\mathbf{u}_I$ and s is calculated from the M25 data at time $n+1$, $\mathbf{u}_{M25}^{n+1}$, using (7.54). $\mathbf{u}^{n+1}$ is then calculated by rearranging (7.54), i.e.

$$\begin{aligned} v &= \frac{1}{2}(r+s), \\ \rho &= exp\left(\frac{r-s}{2C_0}\right). \end{aligned}$$

7.3.2 Characteristic Variables for the Berg-Mason-Woods Model

For the BMW model we have

$$X = \begin{pmatrix} 1 & 1 \\ v + \sqrt{-\dfrac{V'(\rho)}{2\tau}} & v - \sqrt{-\dfrac{V'(\rho)}{2\tau}} \end{pmatrix}, \quad X^{-1} = -\sqrt{\frac{\tau}{-2V'(\rho)}}\begin{pmatrix} v - \sqrt{-\dfrac{V'(\rho)}{2\tau}} & -1 \\ -v - \sqrt{-\dfrac{V'(\rho)}{2\tau}} & 1 \end{pmatrix} \tag{7.55}$$

and

$$\Lambda = \begin{pmatrix} v + \sqrt{-\dfrac{V'(\rho)}{2\tau}} & 0 \\ 0 & v - \sqrt{-\dfrac{V'(\rho)}{2\tau}} \end{pmatrix},$$

constructed from the eigenvalues and eigenvectors of A.

From (7.48), we have that

$$\begin{aligned} \hat{r}_t &= -\sqrt{\frac{\tau}{-2V'(\rho)}} \left(v\rho_t - \sqrt{-\frac{V'(\rho)}{2\tau}}\rho_t - (\rho v)_t \right) \\ &= -\sqrt{\frac{\tau}{-2V'(\rho)}} \left(-\rho v_t - \sqrt{-\frac{V'(\rho)}{2\tau}}\rho_t \right) \\ &= \rho\sqrt{\frac{\tau}{-2V'(\rho)}} \left(v_t + \frac{1}{\rho}\sqrt{-\frac{V'(\rho)}{2\tau}}\rho_t \right), \end{aligned} \tag{7.56}$$

and similarly for $\hat{r}_x$. The partial differential equation for $\hat{s}$ is found to be

$$\begin{aligned} \hat{s}_t &= -\sqrt{\frac{\tau}{-2V'(\rho)}} \left(-v\rho_t - \sqrt{-\frac{V'(\rho)}{2\tau}}\rho_t + (\rho v)_t \right), \\ &= -\rho\sqrt{\frac{\tau}{-2V'(\rho)}} \left(v_t - \frac{1}{\rho}\sqrt{-\frac{V'(\rho)}{2\tau}}\rho_t \right). \end{aligned} \tag{7.57}$$

Again, (7.56) and (7.57) cannot be solved explicitly, so we rewrite them as (7.53) where

$$M = \rho\sqrt{\frac{\tau}{-2V'(\rho)}} \begin{pmatrix} 1 & 0 \\ 0 & -1 \end{pmatrix}$$

and

$$\mathbf{r} = \begin{pmatrix} r \\ s \end{pmatrix} = \begin{pmatrix} v + \displaystyle\int_a^\rho \frac{1}{\bar{\rho}}\sqrt{-\frac{V'(\bar{\rho})}{2\tau}}d\bar{\rho} \\ v - \displaystyle\int_b^\rho \frac{1}{\bar{\rho}}\sqrt{-\frac{V'(\bar{\rho})}{2\tau}}d\bar{\rho} \end{pmatrix}, \tag{7.58}$$

where a and b are arbitrary constants. The integral

$$\int_a^\rho \frac{1}{\rho}\sqrt{-\frac{V'(\bar{\rho})}{2\tau}}d\bar{\rho} = \int_a^\rho g(\bar{\rho})d\bar{\rho}$$

for example, can be approximated using Simpson's Rule,

$$\int_a^\rho g(\bar{\rho})d\bar{\rho} \approx \frac{1}{6}(\rho - a)\left(g(a) + 4g(a+\rho) + g(\rho)\right), \tag{7.59}$$

where ρ and v are the cell Roe averages when the Characteristic Variable is being calculated from inside the cell and $\rho = \rho_B$, $v = v_B$ when calculating the Characteristic Variable from the boundary.

Substituting (7.53) into (7.49) we have that

$$M\left(\mathbf{r}_t + \Lambda \mathbf{r}_x\right) = \mathbf{0},$$

since M is diagonal, and provided $\rho\sqrt{\dfrac{\tau}{-2V'(\rho)}} \neq 0$, and hence $\rho \neq 0$, M is invertible, therefore the Characteristic Variables are the components of

$$\mathbf{r}_t + \Lambda \mathbf{r}_x = \mathbf{0},$$

given by (7.58) with wavespeeds $\lambda_{1,2}$ respectively.

When $\lambda_1 < 0$ and $\lambda_2 > 0$ for example, (Figure 7.3) we calculate r by tracing back the characteristic to the previous time step into the cell between nodes 1 and 2, and take a linear interpolation between $\mathbf{u}_1$ and $\mathbf{u}_2$ to find the corresponding $\mathbf{u}_I$. r is then calculated using $\mathbf{u}_I$ and s is calculated from the M25 data at time $n+1$, $\mathbf{u}_{M25}^{n+1}$, using (7.58). Again, $\mathbf{u}^{n+1}$ is calculated by rearranging (7.58) to get

$$v = \frac{r+s}{2} + \int_a^b \frac{1}{\bar{\rho}}\sqrt{-\frac{V'(\bar{\rho})}{2\tau}}d\bar{\rho},$$

$$\int_a^\rho \frac{1}{\bar{\rho}}\sqrt{-\frac{V'(\bar{\rho})}{2\tau}}d\bar{\rho} + \int_b^\rho \frac{1}{\bar{\rho}}\sqrt{-\frac{V'(\bar{\rho})}{2\tau}}d\bar{\rho} = \frac{r-s}{2},$$

where ρ could be calculated using Newton-Raphson iterations.

This approach is rather involved and uses many approximations. A simpler approach is to eliminate the need to find Characteristic Variables by adding a *ghost cell* either side of the boundary nodes containing real data. This is discussed later in Section 7.4.1

7.3.3 Characteristic Variables for the Aw-Rascle Model

For the Aw-Rascle model we have

$$X = \begin{pmatrix} 1 & 1 \\ v + (\gamma+1)P & v+P \end{pmatrix}, \quad X^{-1} = \frac{-1}{\gamma P}\begin{pmatrix} v+P & -1 \\ -v-(\gamma+1)P & 1 \end{pmatrix} \tag{7.60}$$

and

$$\Lambda = \begin{pmatrix} v & 0 \\ 0 & v-\gamma P \end{pmatrix},$$

constructed from the eigenvalues and eigenvectors of A.

From (7.48), we have that

$$\begin{aligned}\hat{r}_t &= \frac{-1}{\gamma P}\left((v+P)\rho_t - y_t\right)\\ &= \frac{-1}{\gamma P}\left((v+P)\rho_t - (\rho(v+P))_t\right)\\ &= \frac{\rho}{\gamma P}\left(v_t + P_t\right), \end{aligned} \tag{7.61}$$

and similarly for $\hat{r}_x$. The partial differential equation for $\hat{s}$ is found to be

$$\begin{aligned}\hat{s}_t &= \frac{-1}{\gamma P}\left(\left(-v-(\gamma+1)P\right)\rho_t + y_t\right),\\ &= \frac{-\rho}{\gamma P} v_t. \end{aligned} \tag{7.62}$$

Again, (7.61) and (7.62) cannot be solved explicitly, so we rewrite them as (7.53) where

$$M = \frac{\rho}{\gamma P}\begin{pmatrix} 1 & 0\\ 0 & -1\end{pmatrix}$$

and

$$\mathbf{r} = \begin{pmatrix} r\\ s\end{pmatrix} = \begin{pmatrix} v+P\\ v\end{pmatrix}. \tag{7.63}$$

Then substituting (7.53) into (7.49) we have that

$$M\left(\mathbf{r}_t + \Lambda \mathbf{r}_x\right) = \mathbf{0},$$

since M is diagonal, and provided $\dfrac{\rho}{\gamma P} \neq 0$, and hence $\rho \neq 0$, M is invertible, therefore

$$\mathbf{r}_t + \Lambda \mathbf{r}_x = \mathbf{0},$$

and the components of $\mathbf{r}$ in (7.63) are the Characteristic Variables with wavespeeds $\lambda_{1,2}$ respectively.

Again, if we consider the case when $\lambda_1 < 0$ and $\lambda_2 > 0$ (Figure 7.3) we calculate r by tracing back the characteristic to the previous time step into the cell between nodes 1 and 2, and take a linear interpolation between $\mathbf{u}_1$ and $\mathbf{u}_2$ to find the corresponding $\mathbf{u}_I$. r is then calculated using $\mathbf{u}_I$ and s is calculated from the M25 data at time $n+1$, $\mathbf{u}^{n+1}_{M25}$, using (7.63). Again, $\mathbf{u}^{n+1}$ is calculated by rearranging (7.63) to get

$$\rho = (r-s)^{\frac{1}{\gamma}},$$

$$v = s.$$

7.3.4 Characteristic Variables for the Zhang Model

The matrix X of eigenvectors used to find the Characteristic Variables is

$$X = \begin{pmatrix} 1 & 1 \\ v - V(\rho) - \rho V'(\rho) & v - V(\rho) \end{pmatrix}, \tag{7.64}$$

and its inverse is

$$X^{-1} = \frac{1}{\rho V'(\rho)} \begin{pmatrix} v - V(\rho) & -1 \\ -v + V(\rho) + \rho V'(\rho) & 1 \end{pmatrix}. \tag{7.65}$$

The diagonal matrix of corresponding eigenvalues is

$$\Lambda = \begin{pmatrix} v & 0 \\ 0 & v + \rho V'(\rho) \end{pmatrix}. \tag{7.66}$$

Multiplying the system by X^{-1} gives

$$X^{-1}\mathbf{u}_t + X^{-1}AXX^{-1}\mathbf{u}_x = 0$$

and hence

$$\hat{\mathbf{r}}_t + \Lambda\hat{\mathbf{r}}_x = 0$$

therefore giving the partial derivatives of the Characteristic Variables

$$\hat{\mathbf{r}}_{t,x} = X^{-1}\mathbf{u}_{t,x} \tag{7.67}$$

i.e.

$$\begin{aligned} \hat{r}_t &= \frac{1}{\rho V'(\rho)} \left((v - V(\rho))\rho_t - w_t \right) \\ &= \frac{1}{\rho V'(\rho)} \left(\frac{w}{\rho}\rho_t - w_t \right) \\ &= \frac{-1}{V'(\rho)} \left(\frac{1}{\rho} w_t - \frac{w}{\rho^2}\rho_t \right) \end{aligned}$$

giving

$$\hat{r}_t = \frac{-1}{V'(\rho)} \left(\frac{w}{\rho} \right)_t. \tag{7.68}$$

Similarly for the second Characteristic Variable s, from (7.67) we have

$$\begin{aligned} \hat{s}_t &= \frac{1}{\rho V'(\rho)} \left((-v + V(\rho) + \rho V'(\rho))\rho_t + w_t \right) \\ &= \frac{1}{\rho V'(\rho)} \left(-\left(\frac{w}{\rho} + \rho V'(\rho) \right) \rho_t + w_t \right) \\ &= \frac{1}{V'(\rho)} \left(-\left(\frac{w}{\rho^2} + V'(\rho) \right) \rho_t + \frac{1}{\rho} w_t \right) \end{aligned}$$

giving

$$\hat{s}_t = \frac{1}{V'(\rho)} \left(\frac{w}{\rho} + V(\rho) \right)_x . \tag{7.69}$$

This gives us a diagonal matrix M, where

$$M = \frac{1}{V'(\rho)} \begin{pmatrix} -1 & 0 \\ 0 & 1 \end{pmatrix}, \tag{7.70}$$

and provided $V'(\rho) \neq 0$, i.e. $\rho \neq 0$, then M^{-1} exists and r, s given by

$$r = \frac{w}{\rho}, \quad s = \frac{w}{\rho} + V(\rho) \tag{7.71}$$

are the Characteristic Variables of the system. The original conservative variables can be recovered from these from

$$V(\rho) = s - r, \quad w = \rho r \tag{7.72}$$

7.4 Boundary Data Fix

At the boundary, because we are using explicit schemes, the boundary approach taken so far using Characteristic Variables does not allow movement of waves into the domain. There is a potential problem if the wavespeeds just inside are such that waves inside are moving out of the domain. This is a result of truncating the computational region. The onset of a large wave entering the region can therefore be missed. For this reason real data is incorporated into the averaged wavespeeds at the boundary cells and the boundary nodes are updated from fluxes for each wave calculated using these averages. This provides the information that the method requires for the onset of an incoming wave. We are unable to use traditional methods here as they require the assumption that the data is smooth at the boundary in which case the wavespeeds would be consistent in a boundary cell with the adjacent real data. In this kind of problem, however, the data is far from smooth hence we cannot ignore the possibility of wavespeeds suddenly changing sign, thereby causing the numerical methods and indeed the theory to break down.

Consider the LWR model (that has only one wavespeed). Figure 7.4 gives the derivative of the flux function, hence the wavespeeds for different values of density, ρ.

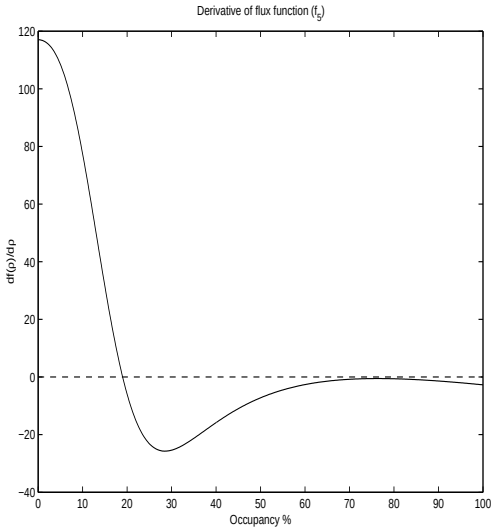

Figure 7.4: Derivative of flux function (f_5).

If $\rho < \bar{\rho}$, the sonic point of the flux function (where $\bar{\rho} = 19\%$), then $\lambda > 0$. Conversely, if $\rho > \bar{\rho}$ then $\lambda < 0$. Now consider the right hand boundary. If $\lambda > 0$, i.e. low density, but there is an approaching wave just outside the solution space with high density, i.e. $\lambda < 0$, then the scheme does not allow that wave to enter the domain. To allow for this type of movement, a fix is required.

The cell averaged wavespeed $\tilde{\lambda}$ at the end cells, rather than being calculated using the nodal values ρ_1^n and ρ_2^n at the left hand boundary (ρ_{m-1}^n, ρ_m^n at the right hand boundary), are therefore instead calculated using real data at the boundary, i.e. using ρ_{BL}^n (real data at the left hand boundary) and ρ_2^n, or ρ_{m-1}^n and ρ_{BR}^n at the right hand boundary. The result is that if for example at the left hand boundary the wavespeed $\tilde{\lambda}(\rho_1, \rho_2) < 0$, but outside the domain a wave is approaching with positive speed, then this wave is prevented from entering the domain. If, however, $\tilde{\lambda}$ is calculated using $\tilde{\lambda}(\rho_{BL}, \rho_2)$ then this averaged wavespeed would allow the wave to enter. This approach is applied at both boundaries.

This argument can be extended to systems, applied to each individual wave at the boundaries. Again, a problem occurs when there is a switch in the direction of the wave across the boundary node. The averaged wavespeeds $\tilde{\lambda}_{1,2}(\mathbf{u}_{BL}^n, \mathbf{u}_2^n)$, $\tilde{\lambda}_{1,2}(\mathbf{u}_{m-1}^n, \mathbf{u}_{BR}^n)$ are calculated at the left and right hand boundaries respectively. The Characteristic Variables are then calculated using these wavespeeds that are now influenced by the real data and hence allow the movement of waves into and out of the boundaries as

required.

7.4.1 BMW boundary fix

As mentioned in Section 7.3.2, calculating the Characteristic Variables for the BMW model is rather involved with many approximations made. It is therefore simpler to avoid having to find the Characteristic Variables altogether and add an extra ghost cell adjacent to each of the end nodes. This extra cell is made up of real data. The schemes are then applied as normal, with these two extra cells, thus the end nodes are treated like any other internal cell, with the ghost cells now being updated only receiving information from one side. This however is not a concern as the ghost cell is simply overwritten at the end of a time step by the real data. This is only an approximation as it is overprescribing the problem, but the ghost cells are outside of the domain and it also allows the movement of waves into and out of the boundaries as described above.

7.5 Riemann Test Problem

To check the Second Order scheme with Sonic Entropy Fix and Flux Limiter is giving the correct results for the PW, AR and Zhang models the results of a Riemann Problem were compared to its analytic solution. The initial densities and velocities were of the form

$$U = \begin{cases} U_L & \text{if } x < 15, \\ U_R & \text{if } x \geq 15, \end{cases} \tag{7.73}$$

where $U := (\rho, v)$.

For the comparison ρ_L and ρ_R were chosen to be 20% and 60% occupancy respectively. For the PW and AR models the initial velocities v_L, v_R were taken to be $V(\rho_L)$, $V(\rho_R)$ respectively. As noted in Zhang however, if $v = V(\rho)$ the single LWR equation is recovered and the solution to the Riemann problem for the two-system is not valid. For this reason the initial velocities were chosen as 60 and 15 km/h respectively.

The analytic Riemann problem solution was obtained from standard work on isothermal equations for the PW model, [21], and the expressions given in the AR

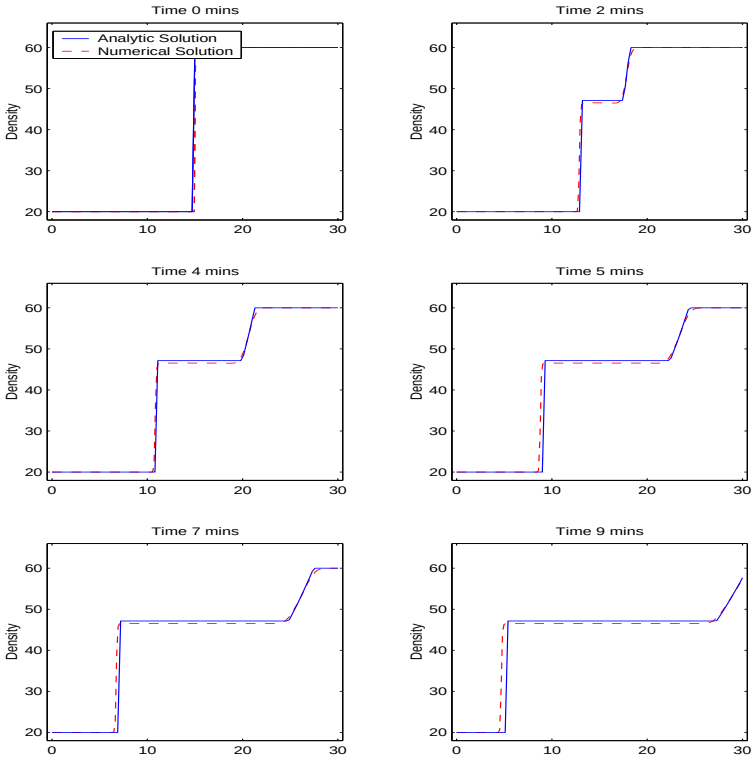

Figure 7.5: Riemann test problem for the PW model. The progression of density through time.

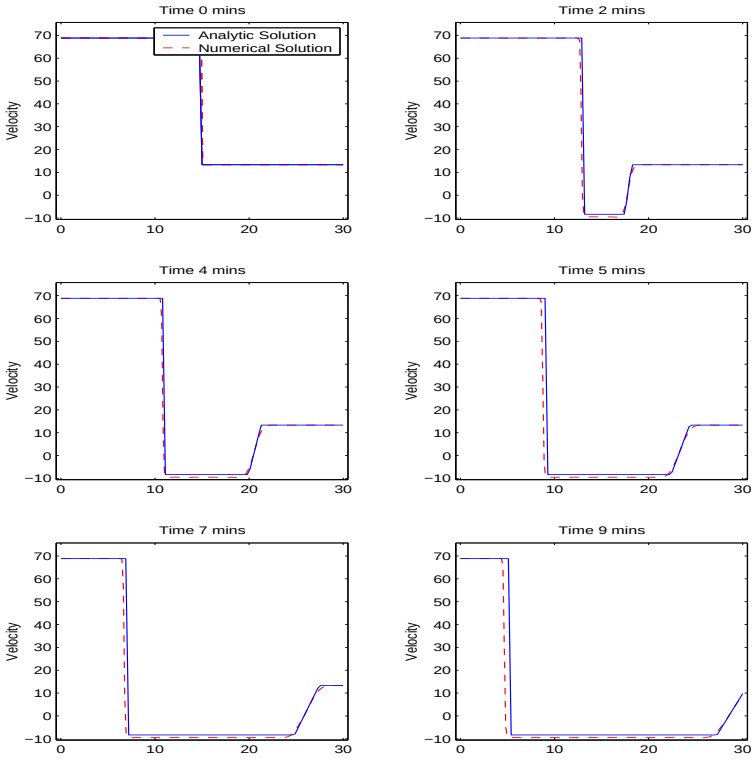

Figure 7.6: Riemann test problem for the PW model. The progression of velocity through time.

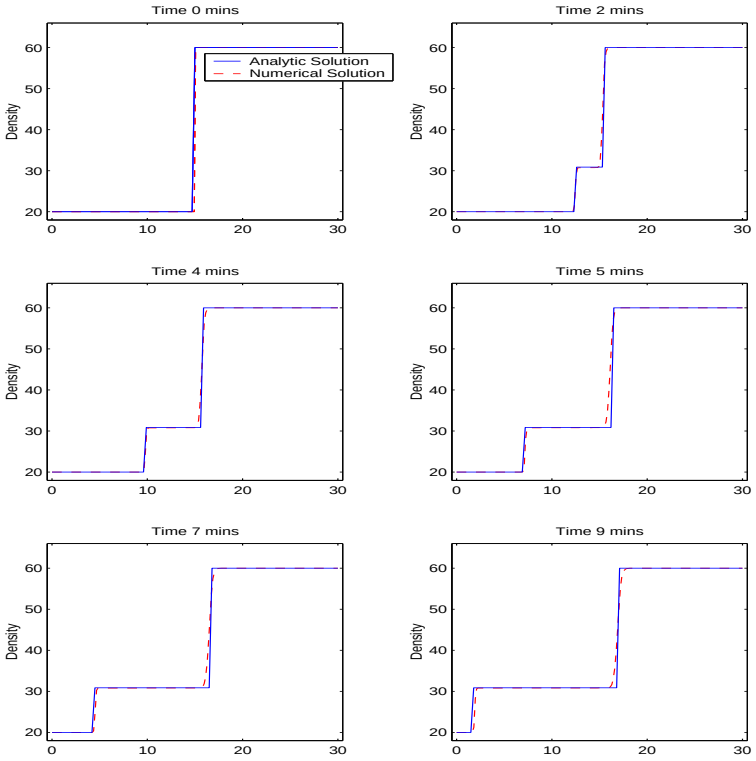

Figure 7.7: Riemann test problem for the AR model. The progression of density through time.

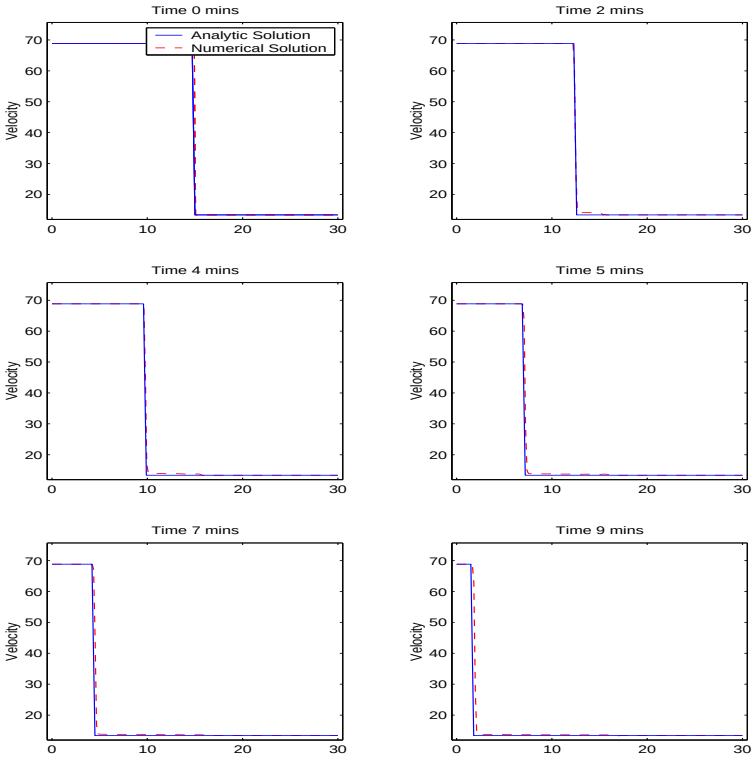

Figure 7.8: Riemann test problem for the AR model. The progression of velocity through time.

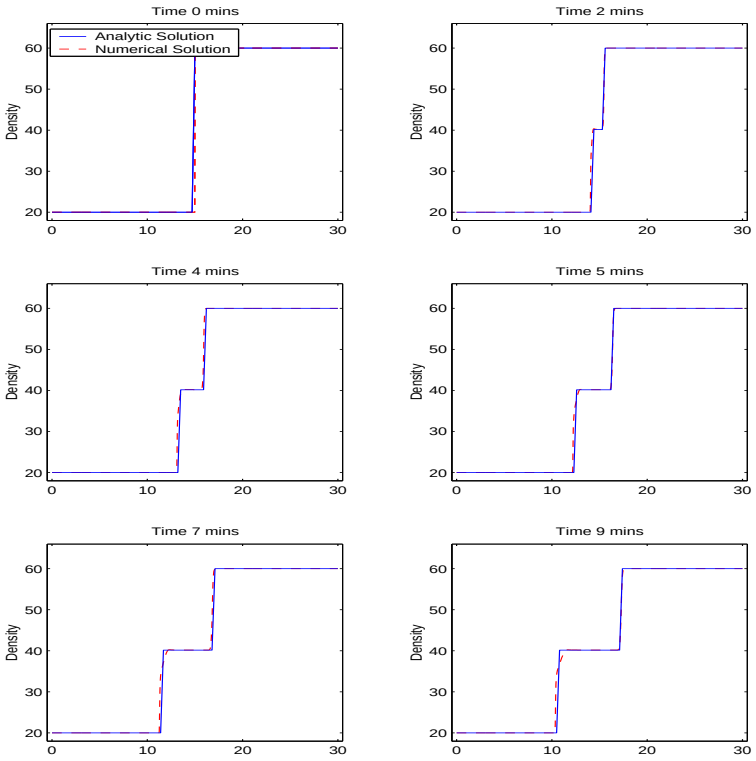

Figure 7.9: Riemann test problem for the Zhang model. The progression of density through time.

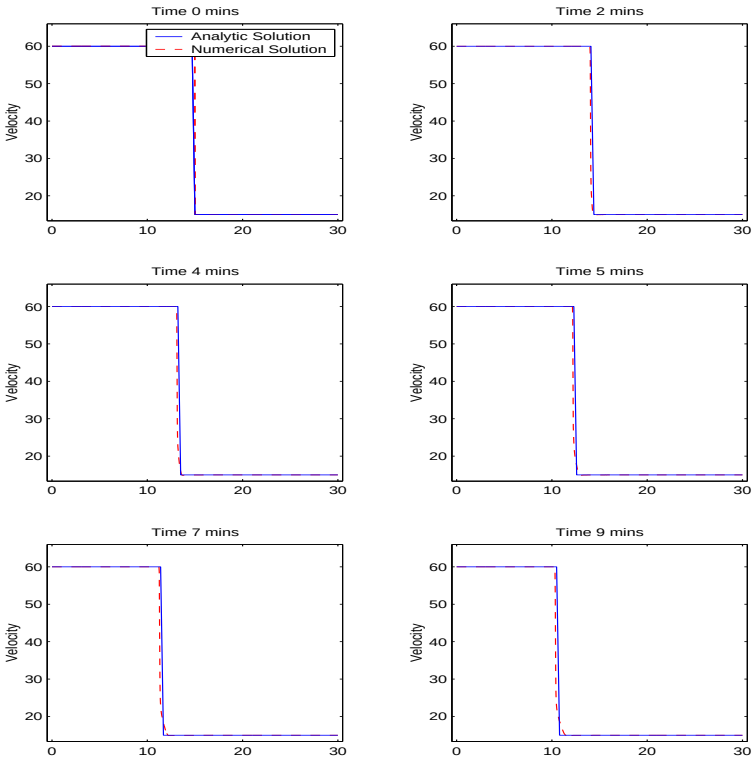

Figure 7.10: Riemann test problem for the Zhang model. The progression of velocity through time.

and Zhang papers, [1] and [40] respectively. Corresponding expressions were derived for the BMW model but unfortunately due to the complexity of these expressions it was not feasible to encode them for graphical representation.

It is worth noting that the PW and BMW Riemann solutions both consist of combinations of shocks and fans, whereas AR and Zhang are always of the form of either a shock or fan followed by a contact discontinuity.

As can be seen from Figures 7.5 to 7.10, the numerical scheme is able to capture the behaviour and movement of the features for all three models with reasonable accuracy.

We have now described the schemes and the boundary procedure and verified the schemes against the Riemann test problem. These are then used in the next Chapter where the models are applied to real data.

Chapter 8

Application to Real Data

8.1 One-Equation Model

After considering the behaviour of the schemes on the test problem with artificial initial conditions in Chapter 4, we now see how the LWR model with the different flux functions copes with reality, and how it compares to the PW, BMW, AR and Zhang models. The real data we are using was collected, courtesy of the Highways Agency through TRL, from a section of the M25 motorway during July 1999, between junctions 10 and 15. For further discussion see Chapter 3. Here we concentrate on the data between junctions 10 and 11 as it is the longest stretch available with no on/off ramps, as the models in their current form do not allow for these.

For the boundary data, when required, the real data averages were used and interpolated between the one minute intervals using a cubic spline interpolant to give the data needed for intermediate time steps.

The Second Order upwind scheme with the Minmod flux limiter was chosen, because it worked best on the one equation test problems, using the five different flux functions ($f_1 - f_5$), of Section 4.1, and the results are plotted in Figure 8.1 and Figure 8.2 against the real averaged data after 5 minutes. The functions f_1 and f_3 are unable to capture the movement of any of the waves, either peaks or troughs, with any kind of accuracy. f_2 captures the troughs to a reasonable degree, but the position of the peaks are captured most accurately by f_4 and f_5 with f_5 capturing the spread a little more. Figure 8.3 shows the progression from the initial conditions through to the five minute

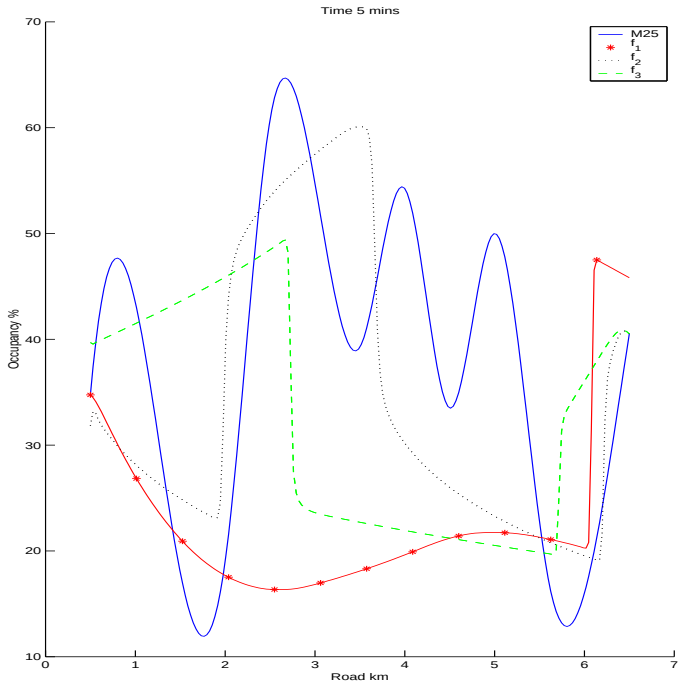

Figure 8.1: LWR Model. Comparison of flux functions f_1 to f_3 at a given time, using real data from the M25 08:30 on the 15/07/99. Simulation was run using Second Order scheme with Minmod, and snapshots were taken after 5 mins.

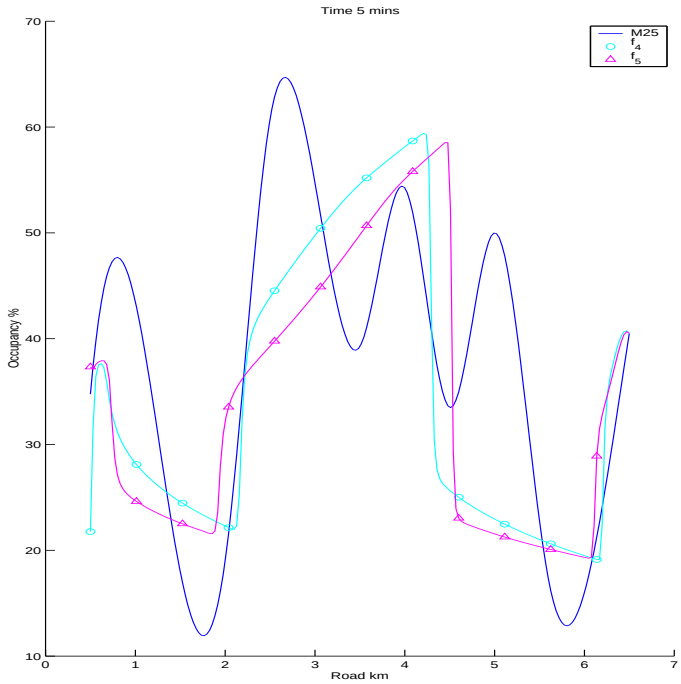

Figure 8.2: LWR Model. Comparison of flux functions f_4 and f_5 at a given time, using real data from the M25 08:30 on the 15/07/99. Simulation was run using Second Order scheme with Minmod, and snapshots were taken after 5 mins.

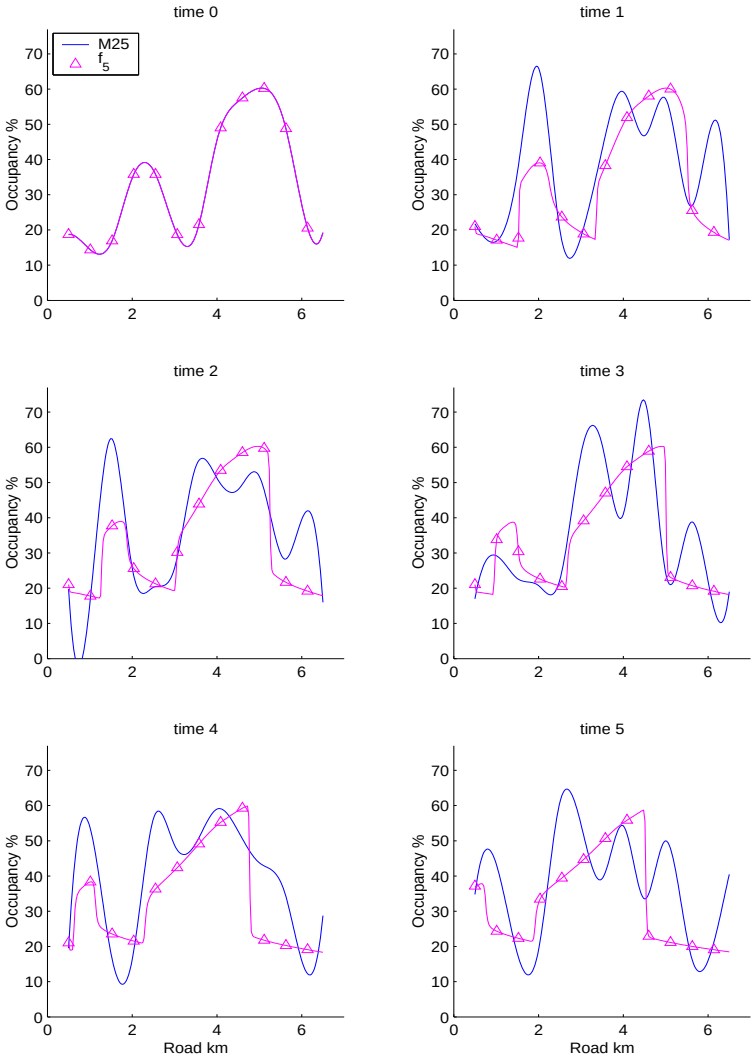

Figure 8.3: LWR Model. Second Order scheme with Minmod using f_5 with M25 data from 08:30 15/07/99 for 5 mins.

plots of Figures 8.1 and 8.2. The shapes of the density profile are not sufficiently similar to the real density profiles, however. It is possible therefore that a system of equations, i.e. a two equation model may be required to model the interactions of vehicles more accurately.

It is a good idea to take a step back and look at the bigger picture. The LWR model with a suitable choice of flux function f is able to capture the movement of peaks and troughs along the road with some success. Figure 8.4 shows a view of the movement of waves both with and against the flow in the real data. There are high density waves moving slowly backwards and low density troughs moving with the traffic with similar velocity. These are perhaps more visible in the contour plot in Figure 8.5. If we now compare the corresponding 3D and contour plots of the LWR model using f_5, Figures 8.6 and 8.7, we can see that f_5 is able to capture slow backward moving waves of high density, fast forward moving troughs of low density, but where it breaks down and fails to model accurately is when these waves interact. The real data suggests that these two types of waves exist and when they cross they have some effect on each other during interaction, but then move off as two separate waves again. This type of interaction can only be modelled by a system. The one equation LWR model only predicts one type of wave for a given density. High density gives slow backward waves, low density gives fast forward waves and when they cross they then move off as one wave with speed determined by the combined density, rather than interacting but separate waves.

8.2 Two-Equation Models

We therefore move onto the PW, BMW, AR and Zhang models in the hope that they capture the two types of waves, and also their interaction. Again the Second Order upwind scheme is chosen. Figures 8.8 and 8.9 are the 3D and contour plots for the PW model. They demonstrate that with a suitable choice of C_o, here taken to be 57, the model captures the speeds of the low density troughs and high density peaks. It has even captured the later peaks that have interacted with the troughs that the LWR model was unable to reproduce. It fails, however, to model the deterioration of the

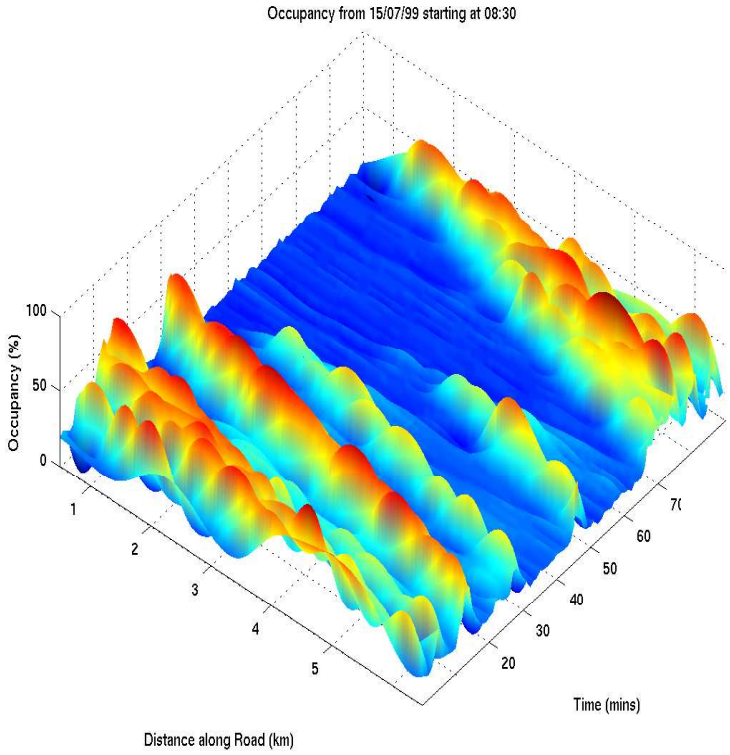

Figure 8.4: 3D plot of occupancy for a period of 90 mins from 08:30 15/07/99.

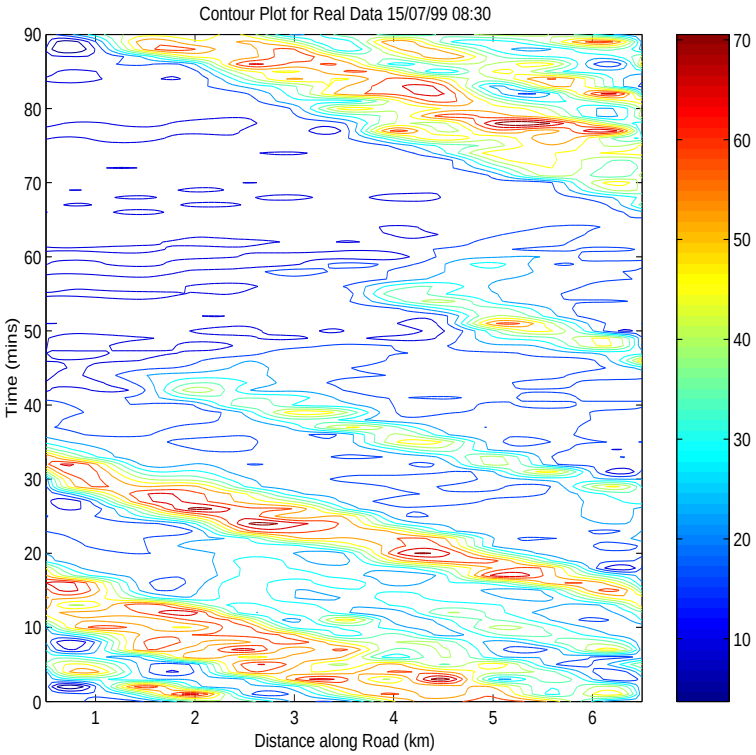

Figure 8.5: Contour plot of occupancy for a period of 90 mins from 08:30 15/07/99

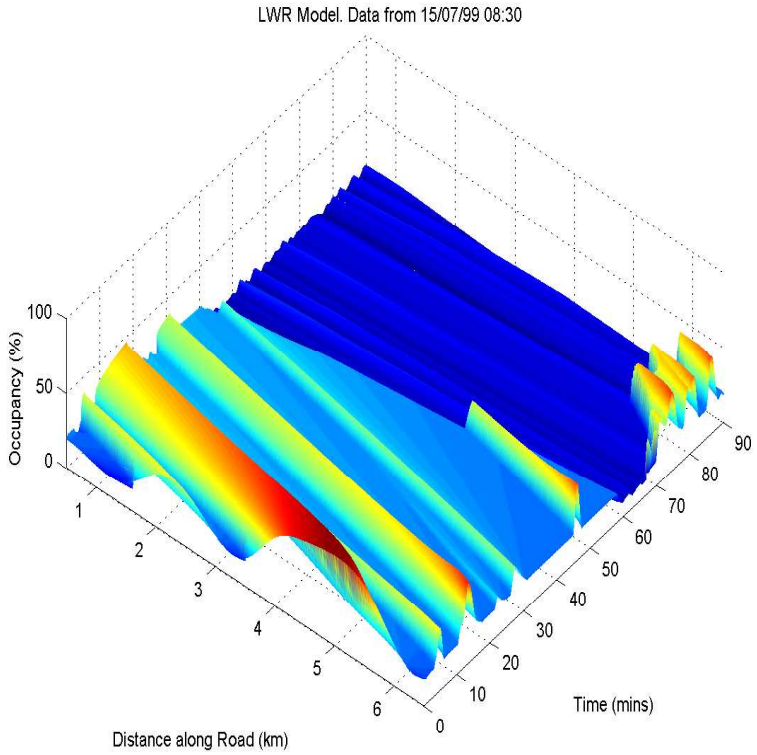

Figure 8.6: 3D plot of occupancy for a period of 90 mins from 08:30 15/07/99 for Lighthill-Whitham-Richards Model. f_5 is the flux function used.

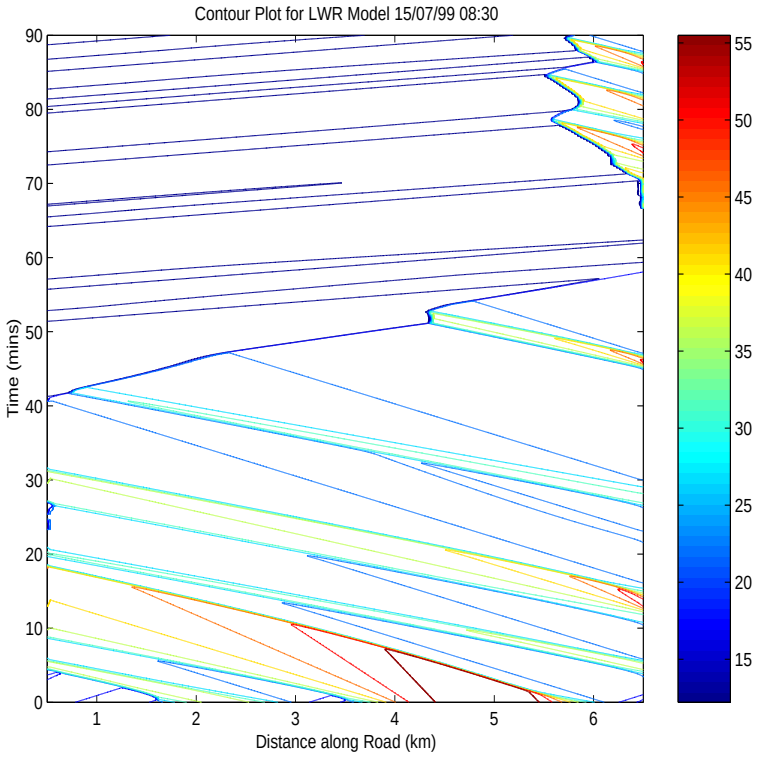

Figure 8.7: 3D plot of occupancy for a period of 90 mins from 08:30 15/07/99 for Lighthill-Whitham-Richards Model. f_5 is the flux function used.

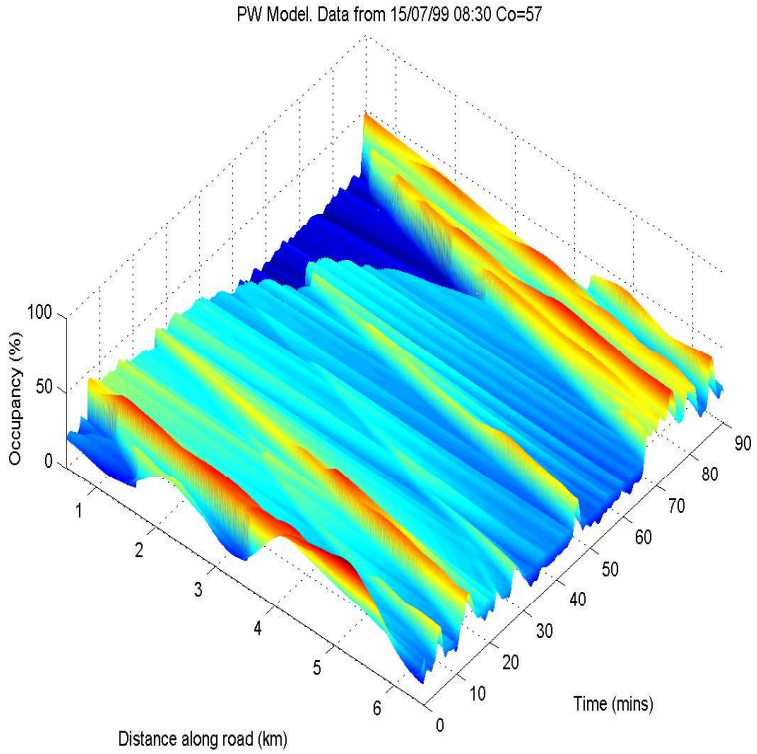

Figure 8.8: 3D plot of occupancy for a period of 90 mins from 08:30 15/07/99 for Payne-Whitham. Co=57.

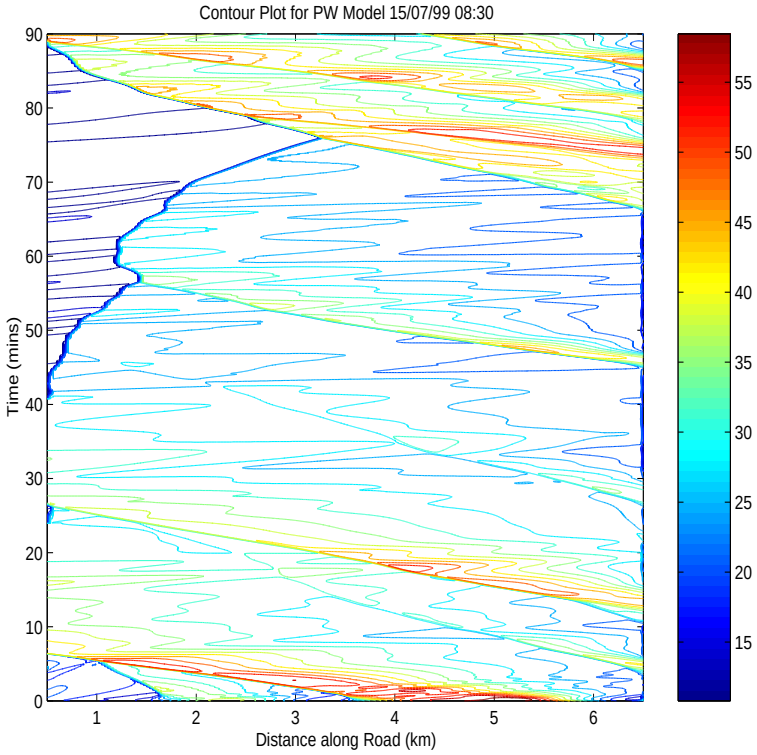

Figure 8.9: 3D plot of occupancy for a period of 90 mins from 08:30 15/07/99 for Payne-Whitham. Co=57.

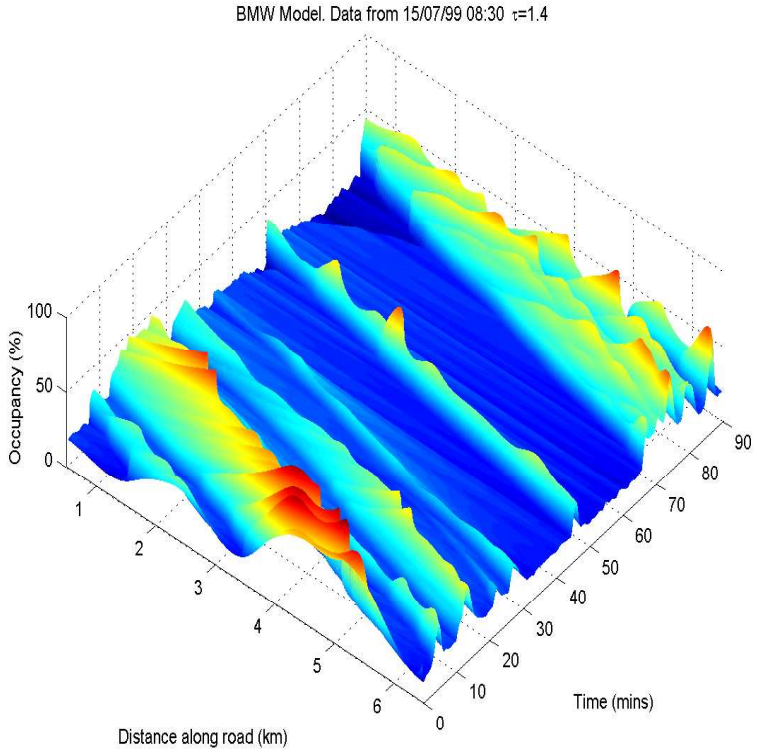

Figure 8.10: 3D plot of occupancy for a period of 90 mins from 08:30 15/07/99 for BMW Model, $\tau = 1.4$ seconds.

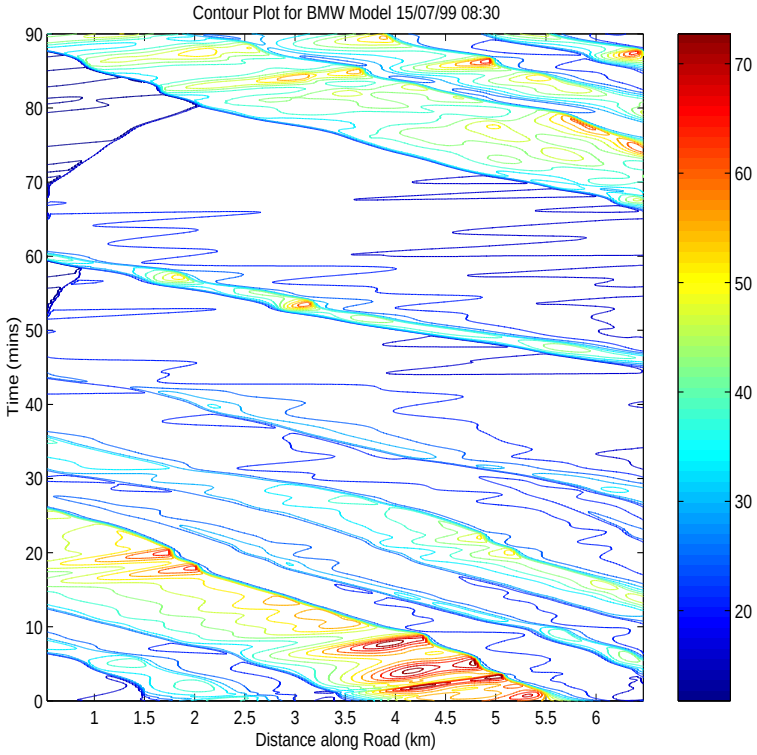

Figure 8.11: 3D plot of occupancy for a period of 90 mins from 08:30 15/07/99 for BMW Model, $\tau = 1.4$ seconds.

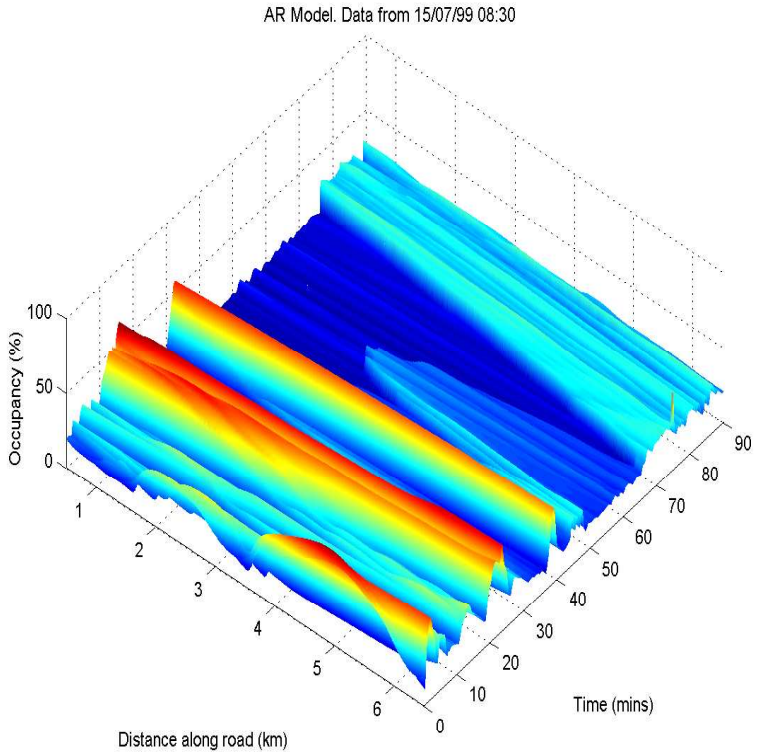

Figure 8.12: 3D plot of occupancy for a period of 90 mins from 08:30 15/07/99 for Aw-Rascle Model. $\gamma = 1.4$.

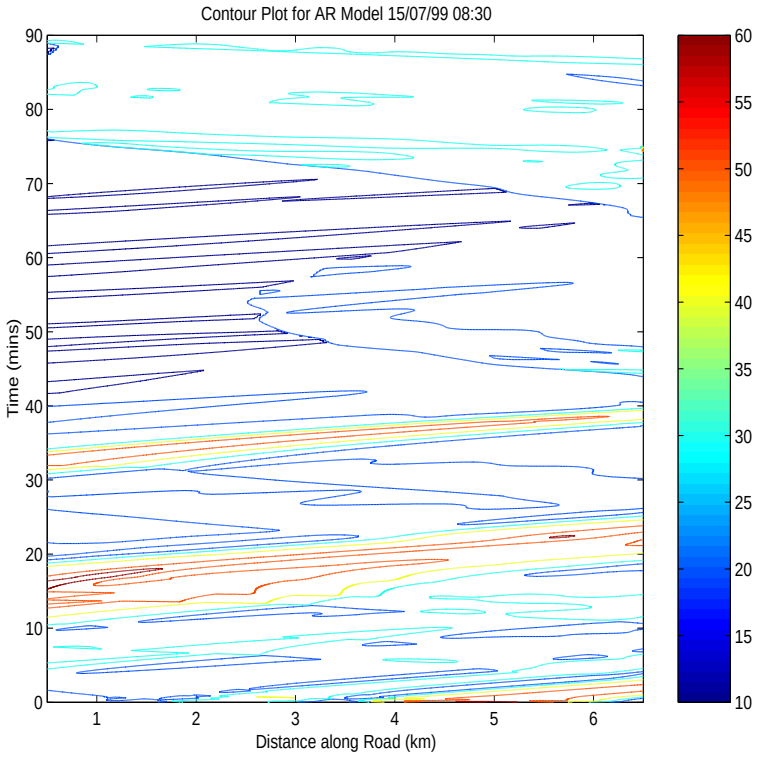

Figure 8.13: 3D plot of occupancy for a period of 90 mins from 08:30 15/07/99 for Aw-Rascle Model. $\gamma = 1.4$.

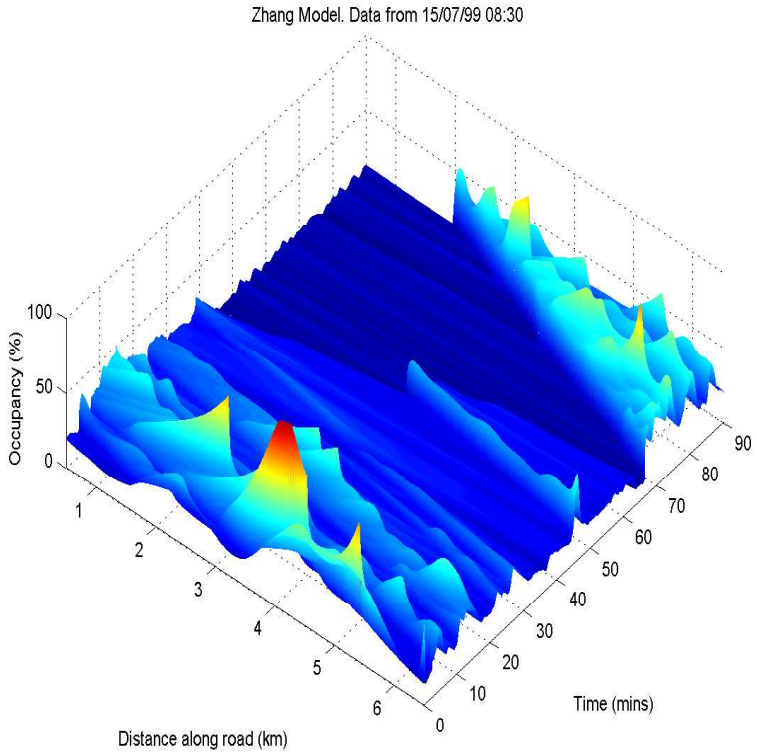

Figure 8.14: 3D plot of occupancy for a period of 90 mins from 08:30 15/07/99 for Zhang Model.

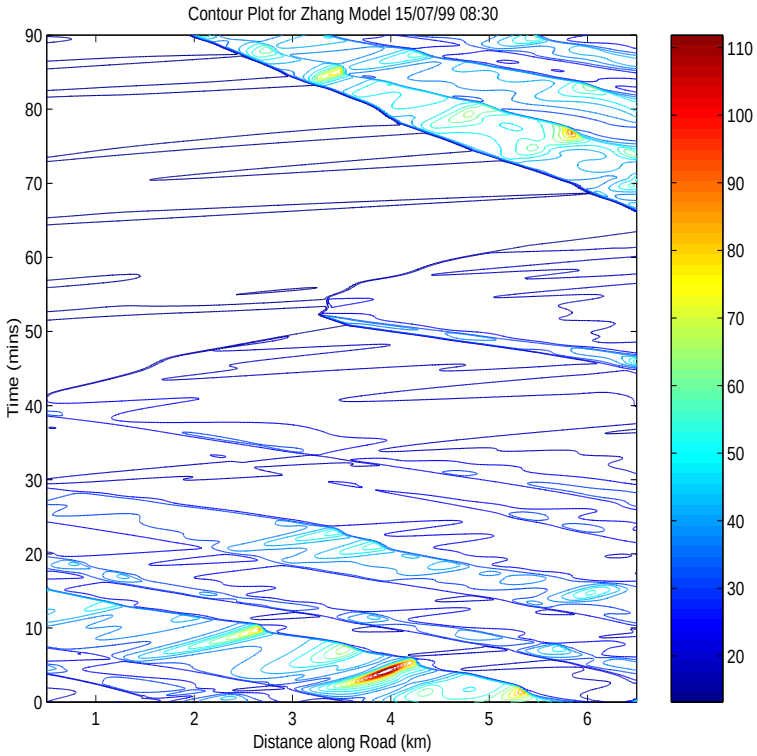

Figure 8.15: 3D plot of occupancy for a period of 90 mins from 08:30 15/07/99 for Zhang Model (note the scale).

high density ridge that starts at the right hand side of the region at approximately $t = 50$ minutes. Also the contrast between peaks and troughs is not as distinct as in the real data, or as modelled by the LWR model. The model also allows negative velocities of the vehicles, i.e. against the flow of traffic. The greatest negative velocity in this simulation was $v = -1.69km/h$. This is one major drawback of the model.

The BMW model, Figures 8.10 and 8.11, being a variation to PW but with variable coefficient of the ρ_x term in the flux function produces similar results, but with better definition. The peaks and troughs are more clearly defined with the variations in the ridges of high density showing the interactions between waves, as seen in the real data. Having the variable coefficient does improve the model. As with the PW model however, the ridge that starts after approximately 50 minutes on the right hand side doesn't deteriorate as in the real data. This suggests that the two models, PW and BMW, haven't quite captured the interactions between different types of waves correctly. This model didn't have any negative velocities in this simulation however, which is another improvement to the PW model.

The AR model with $\gamma = 1.4$ does appear to allow for the deterioration of the high density wave when low density waves move into it, but it has the major drawback of modelling very high density waves incorrectly, Figures 8.12 and 8.13. For these waves their speeds are predicted to travel with high positive velocity, i.e. with the flow of traffic. This contradicts the real data. It fares much more favourably with much lower densities. Low density troughs appear to move with the flow at the correct speed and medium density waves travel against the flow correctly (see wave at x=6.5 km at time 50 mins), but at slightly too fast a speed (see wave at t=70 mins x=6.5 km). It also allowed negative velocities of the vehicles, the most negative being $v = -2.24km/h$ in this simulation.

Moving on to the Zhang model the results are much more encouraging, Figures 8.14 and 8.15. It appears to capture the correct movement of waves at approximately the correct speeds given high, medium or low densities. It models the interaction of the medium and low density waves (e.g the wave starting at x=6.5 km time=50 mins) and its deterioration. It also models the high density waves and their interactions with low density troughs starting from x=6.5 km time=70 mins. The backward moving

peaks are travelling at too slow a speed however, and it is not clear if this is due to the speed of high density waves being predicted incorrectly, if it is allowing too much interaction between the peaks and troughs, or a combination of both. Looking at the finer detail of the density distribution, the method tends to smooth out the density in some regions and clump together in others. In places where the density has clumped, at times the values exceed the maximum allowed, reaching a peak of $\sim 16\%$ over the maximum. This could be partly due to the second order scheme since for systems the limiter is not guaranteed to maintain the TVD property at peaks. Overall, however, it captures most of the features better than any of the other models discussed here and no negative velocities were observed in this simulation. Chapter 9 includes the addition of a viscosity term to the model that overcomes the problem of allowing greater than maximal densities.

Figures 8.16 and 8.17 are included for completeness, and to compare how the models capture individual features of the wave movements in the real data. At this stage however, as discussed, this is perhaps a little premature and efforts should be concentrated on capturing the overall movement and interactions of waves rather than the fine detail, although to capture both would be the ultimate aim.

A second set of results were obtained in order to see if the above observations were typical of the type of behaviour exhibited by these models. The same parameter values were used and the initial data was taken from 06/07/99 starting from 07:00 for a period of 90 minutes. Figures 8.18 and 8.19 are the real data. In this example there are many high density ridges running almost parallel moving slowly backwards against the flow of traffic. This is after an initial period of relatively low density with only one smaller ridge.

As before the LWR model is able to capture individual wave movements accurately, but is unable to capture interactions between waves, Figures 8.20 and 8.21. This results in the deterioration of the high density peak at the start of the run by the model that should persist. The ridges are also very smooth compared to the real data.

The PW model is less able to capture the speeds of the backward moving ridges of high density, Figures 8.22 and 8.23. The model predicts a slower velocity. It also incorrectly predicts the deterioration of many of the ridges due to interactions with low

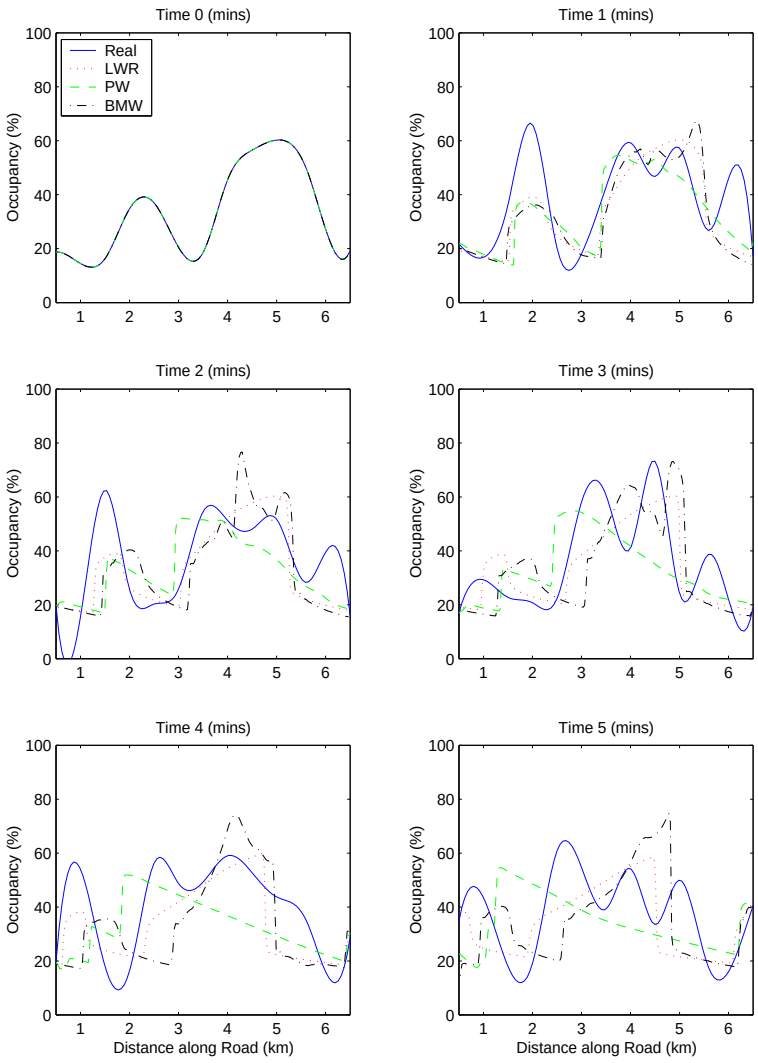

Figure 8.16: Comparison of the LWR, PW and BMW models to the real data. Second order with flux limiter. LWR with flux function f_5, PW model with $Co = 57$, BMW model with $\tau = 1.4$. Time is in minutes.

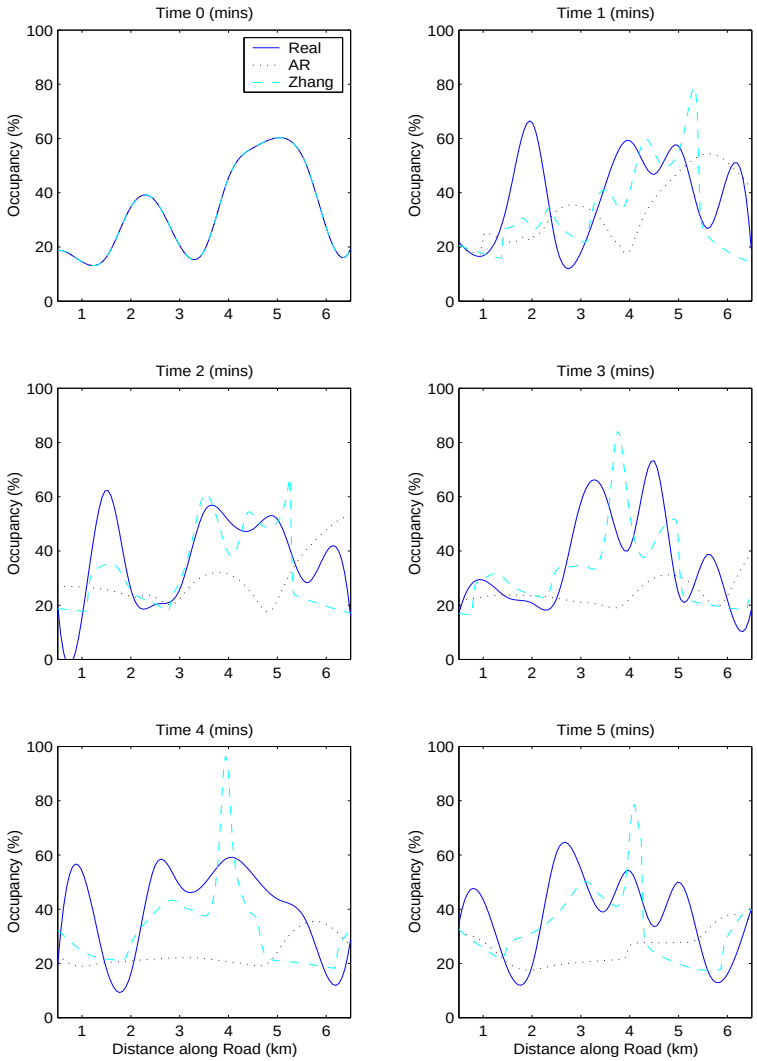

Figure 8.17: Comparison of the AR and Zhang models to the real data, using Second order with flux limiter. $\gamma = 1.4$ for the AR model. Time is in minutes.

density high speed troughs moving into them. Again it also allows unphysical backward moving vehicles, with a greatest maximum negative velocity of $v = -0.92km/h$.

The BMW model also fares less well with this example, with it also predicting the deterioration of some of the earlier ridges. It does, however, give a better prediction of wave speeds and better definition of the ridges and the troughs as before, Figures 8.24 and 8.25.

The AR model again fails in modelling the flow. It allows negative velocities of vehicles up to a maximum of $v = -7.94km/h$ as well as predicting the wrong direction of flow fo the high density ridges, Figures 8.26 and 8.27.

The best results were obtained from the Zhang model, Figures 8.28 and 8.29. This model predicted the correct wave speeds, it allowed the higher density ridges to persist and showed interactions in the ridges with low density fast forward moving waves. Again it allowed densities greater than the maximal, reaching values of up to $\rho = 124.6\%$ but again with the introduction of a viscosity these peaks were smoothed out and only physical values remained. Some of the densities of the ridges were a little lower than observed in the real data and the first ridge was allowed to deteriorate whereas in reality it persisted. Overall however, this model gave the best results in this particular example, with LWR a close second.

So far we have only considered the homogeneous systems. However, PW and BMW have relaxation and viscosity terms on the right hand side, AR recommends the addition of a relaxation term to overcome the deficiency of the maximal speed reached by vehicles on an empty road being dependent on the initial data, and the Zhang model has a viscosity term by taking a different approach in the derivation of the model. In the next Chapter we consider the effects of these terms on all four of these models.

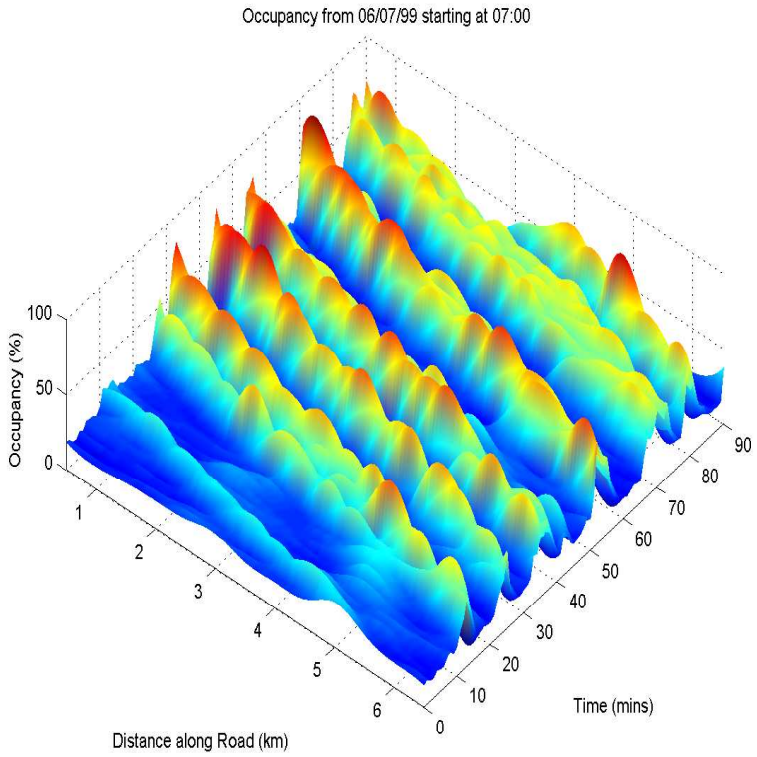

Figure 8.18: 3D plot of occupancy for a period of 90 mins from 07:00 06/07/99.

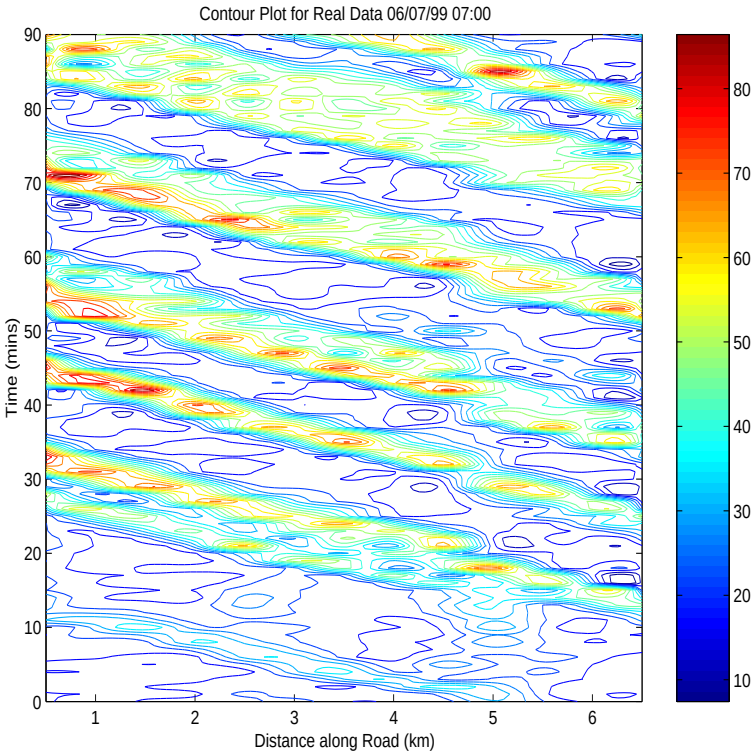

Figure 8.19: Contour plot of occupancy for a period of 90 mins from 07:00 06/07/99

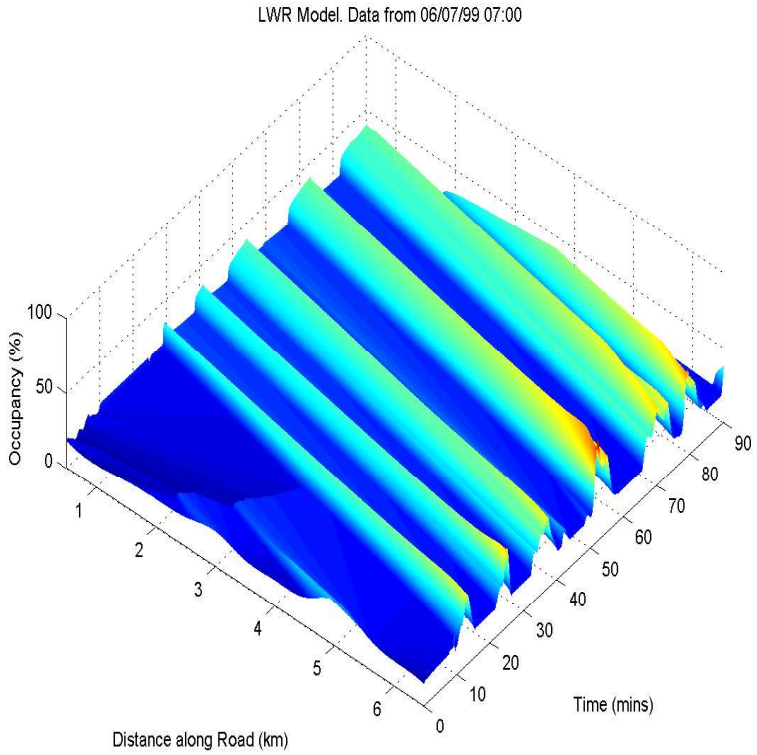

Figure 8.20: 3D plot of occupancy for a period of 90 mins from 07:00 06/07/99 for Lighthill-Whitham-Richards Model. f_5 is the flux function used.

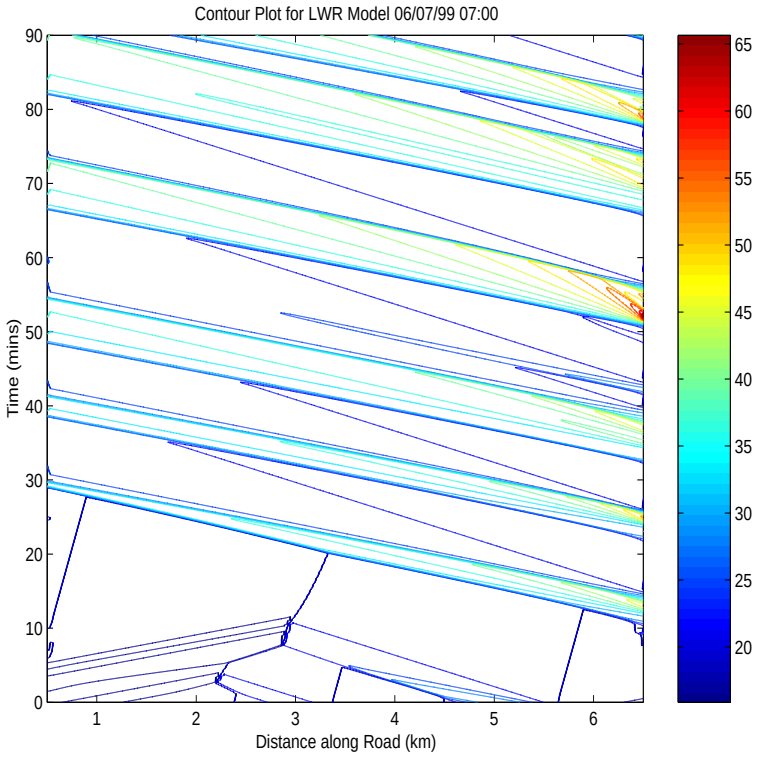

Figure 8.21: 3D plot of occupancy for a period of 90 mins from 07:00 06/07/99 for Lighthill-Whitham-Richards Model. f_5 is the flux function used.

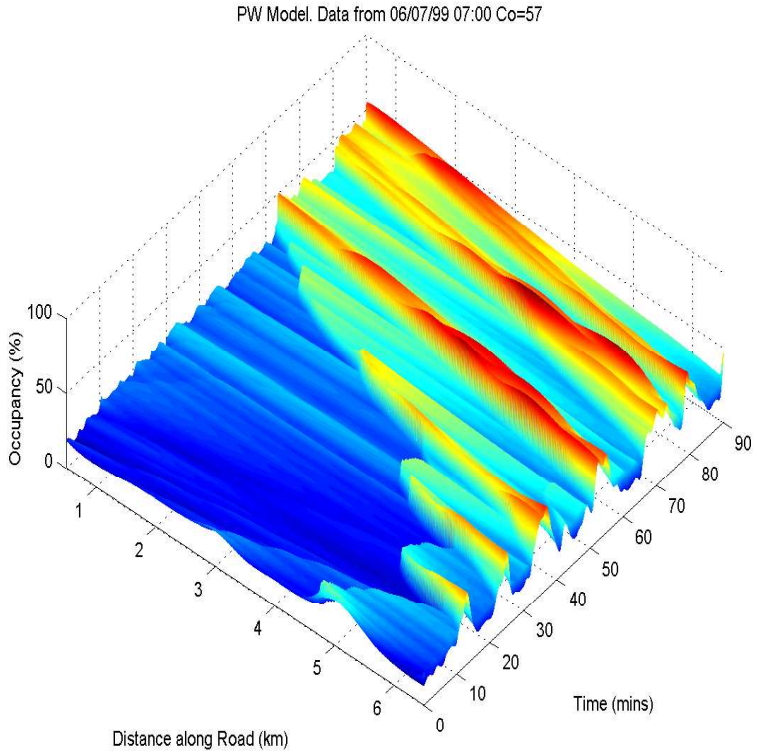

Figure 8.22: 3D plot of occupancy for a period of 90 mins from 07:00 06/07/99 for Payne-Whitham. Co=57.

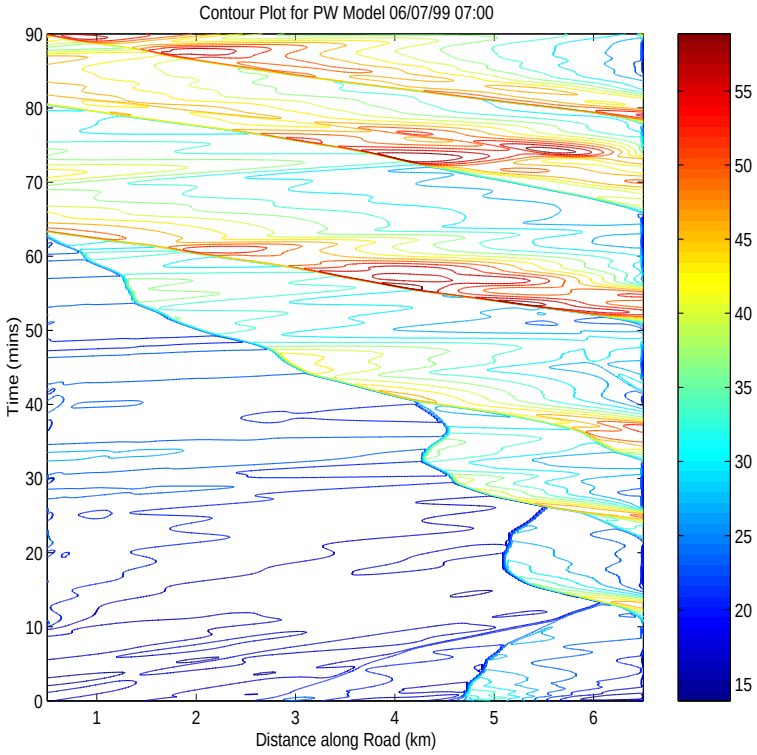

Figure 8.23: 3D plot of occupancy for a period of 90 mins from 07:00 06/07/99 for Payne-Whitham. Co=57.

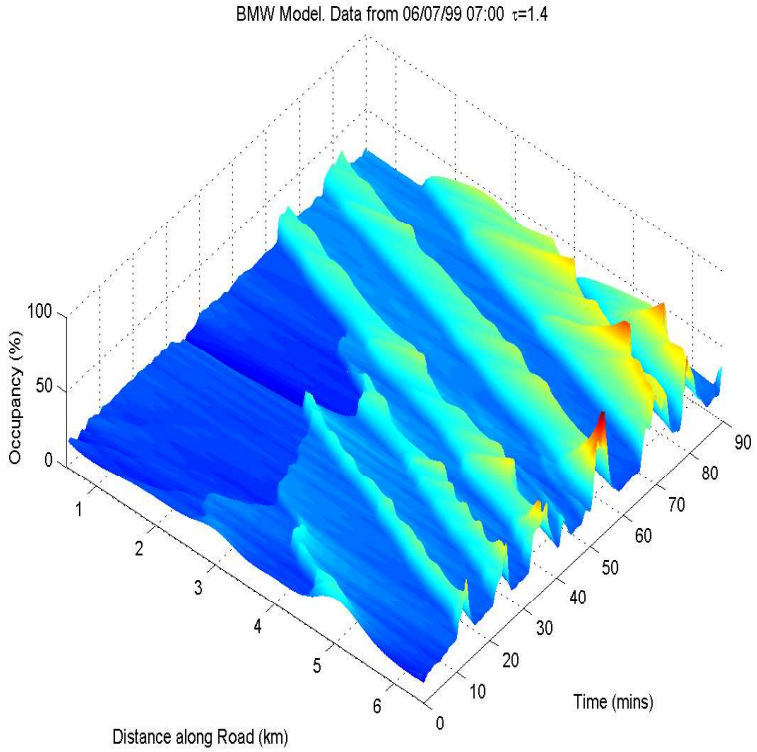

Figure 8.24: 3D plot of occupancy for a period of 90 mins from 07:00 06/07/99 for BMW Model, $\tau = 1.4$ seconds.

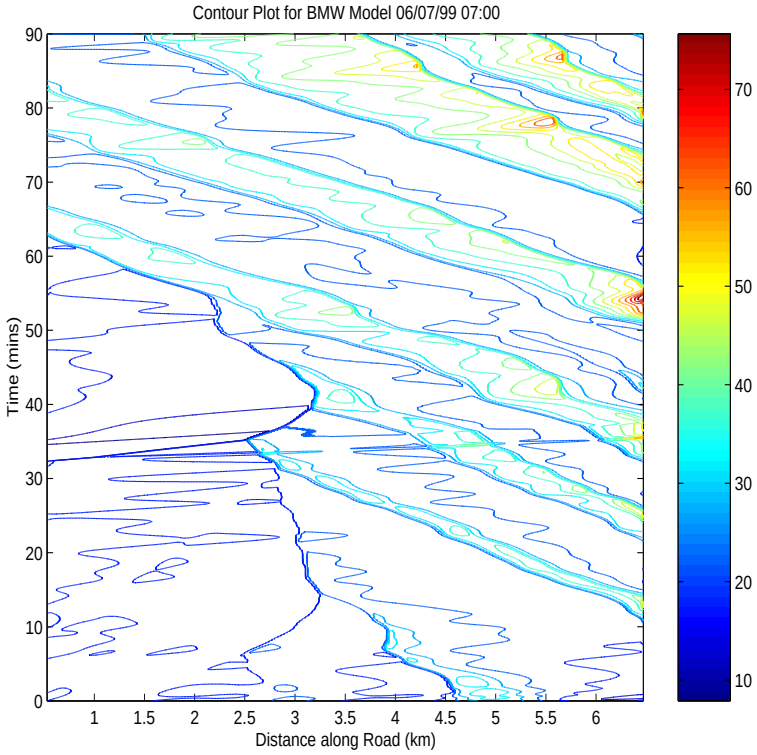

Figure 8.25: 3D plot of occupancy for a period of 90 mins from 07:00 06/07/99 for BMW Model, $\tau = 1.4$ seconds.

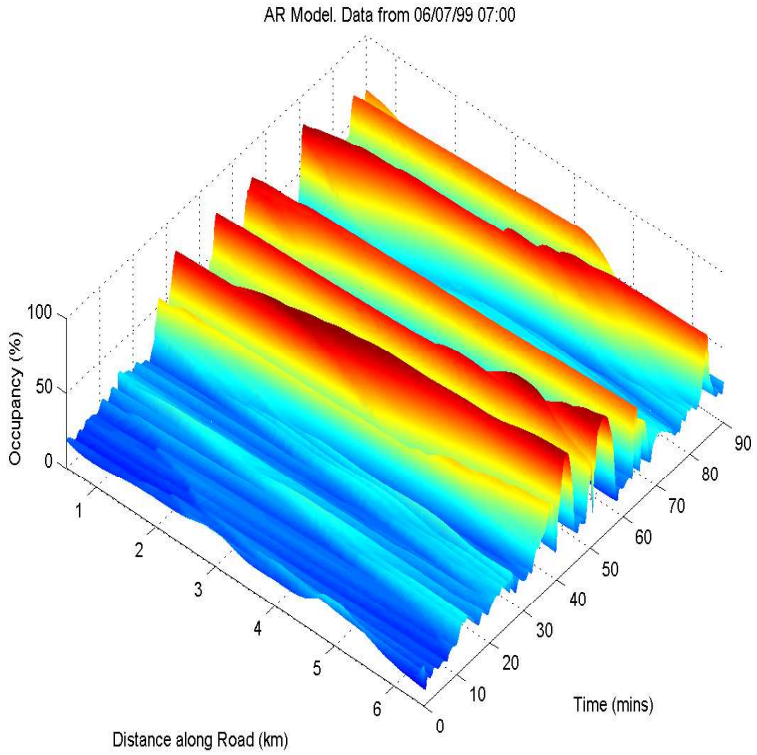

Figure 8.26: 3D plot of occupancy for a period of 90 mins from 07:00 06/07/99 for Aw-Rascle Model. $\gamma = 1.4$.

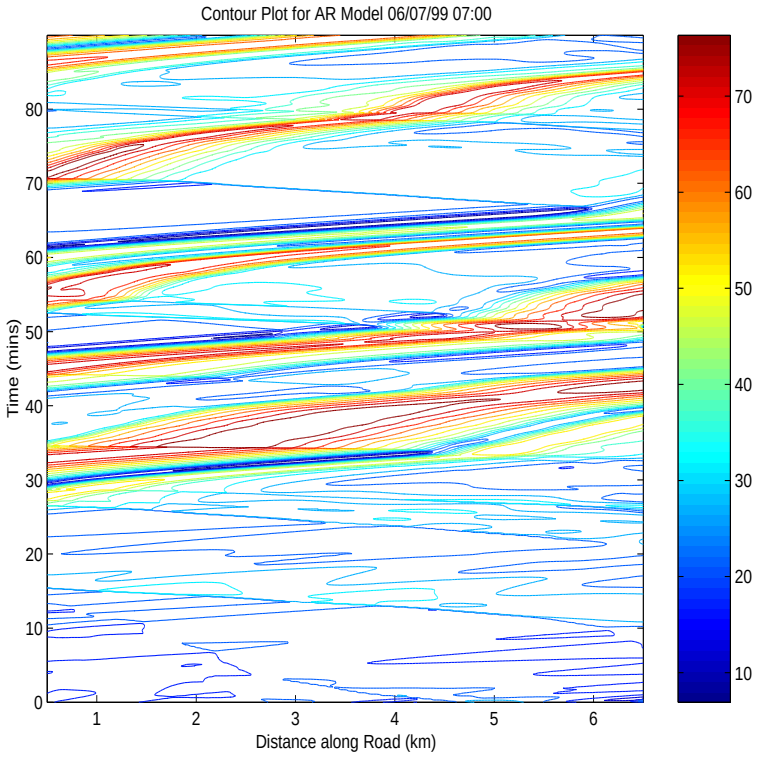

Figure 8.27: 3D plot of occupancy for a period of 90 mins from 07:00 06/07/99 for Aw-Rascle Model. $\gamma = 1.4$.

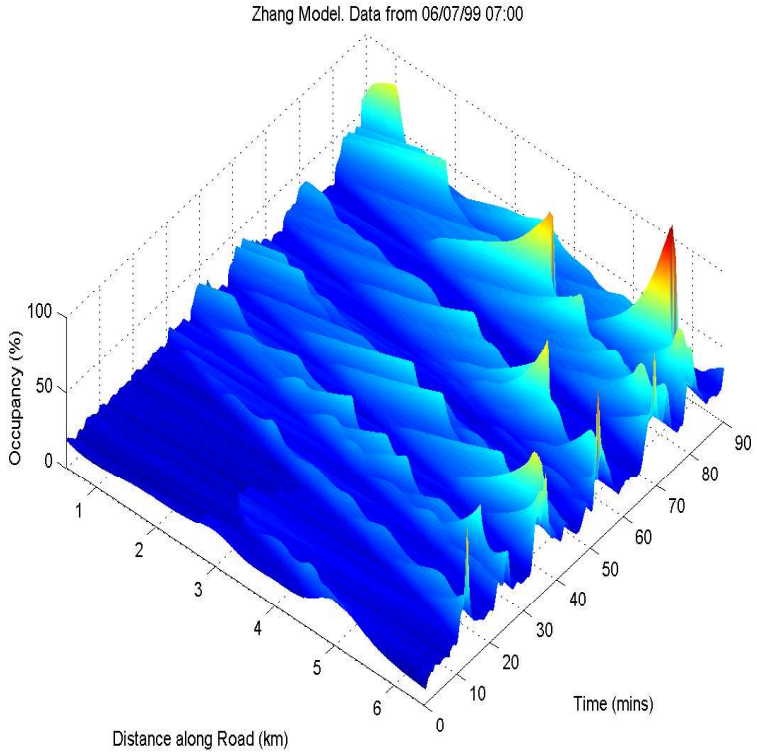

Figure 8.28: 3D plot of occupancy for a period of 90 mins from 07:00 06/07/99 for Zhang Model.

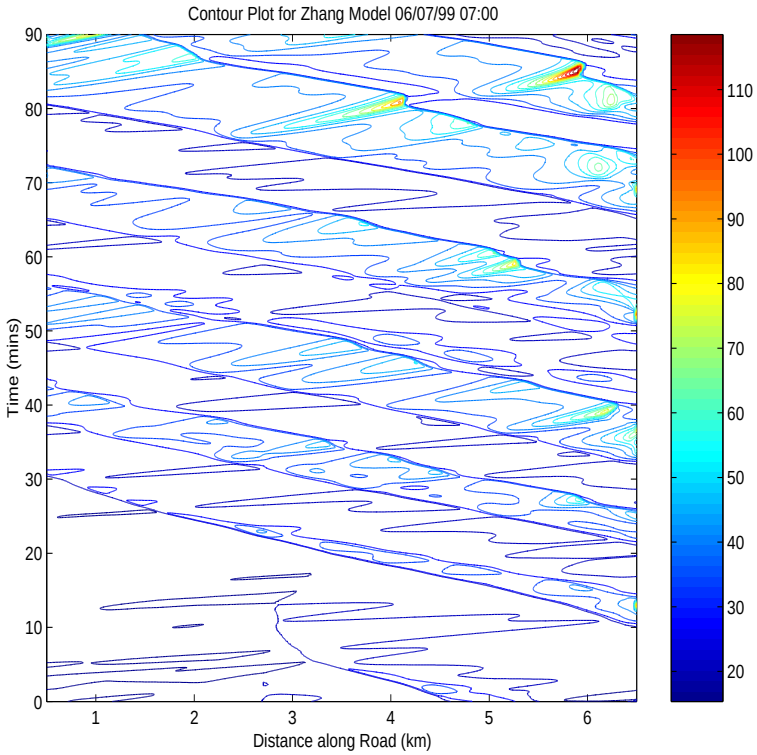

Figure 8.29: 3D plot of occupancy for a period of 90 mins from 07:00 06/07/99 for Zhang Model.

Chapter 9

Relaxation and Viscosity

9.1 Relaxation

As discussed in Chapters 2 and 5, the original PW model contains a relaxation term that is designed to make the model more *traffic like*. This term, given by $\frac{V(\rho)-v}{\tau}$, contains the velocity function $V(\rho)$ (see Chapter 4) which represents the ideal driving speed of vehicles for a given density. If a vehicle's speed is greater than this optimal velocity then the relaxation term has the effect of slowing the vehicle down. Conversely if the vehicle has velocity less than this optimal velocity then the relaxation term has the effect of speeding the vehicle up. Unlike the LWR model this change is not instantaneous, therefore a *relaxation time*, or the time it takes the vehicle to adjust its speed, is introduced by τ. Helbing and Treiber [14] take this time τ to be 32 seconds, Payne suggested a relaxation time of 10 seconds [27], whereas follow-the-leader models use values of between 1 and 2 seconds. The value of τ is therefore still under debate.

If the relaxation term is added to the right hand side of the second equation of the PW model (5.2), then in the form of the system using conservative variables this term becomes

$$\rho\frac{V(\rho)-v}{\tau}. \tag{9.1}$$

In fact, the relaxation term can be added to the second equation of each of the models PW, BMW, AR and Zhang and takes the form (9.1) in each of the systems using conservative variables.

The relaxation term on the right hand side makes the system non-homogeneous

and is more generally referred to as a source term. The right hand side for each system in each case is therefore given by

$$R = \begin{pmatrix} 0 \\ \rho\frac{V(\rho)-v}{\tau} \end{pmatrix}. \tag{9.2}$$

9.2 Projection onto the Eigenvalues

In order to implement this updated model using our second order upwind flux limited scheme we project the source term onto the eigenvalues of the system and update each wave component accordingly. This is a *splitting* approach and superimposes the source term on to the original implementation of the scheme on the homogeneous system,([31]).

Firstly we find values β_1 and β_2 such that

$$\sum_{i=1}^{2} \beta_i \tilde{\mathbf{e}}_i = \begin{pmatrix} 0 \\ \tilde{\rho}\frac{V(\tilde{\rho})-\tilde{v}}{\tau} \end{pmatrix} \tag{9.3}$$

where the variables in the relaxation term and the eigenvectors $\mathbf{e}_i$ are evaluated using the averages (Roe or alternative) for each cell. Then we update componentwise, i.e. if $\lambda_{i,j+1/2} > 0$ then

$$\mathbf{u}_{j+1}^{n+1} = \mathbf{u}_{j+1}^{(n+1)*} + \Delta t \beta_i \tilde{\mathbf{e}}_i, \tag{9.4}$$

otherwise

$$\mathbf{u}_{j}^{n+1} = \mathbf{u}_{j}^{(n+1)*} + \Delta t \beta_i \tilde{\mathbf{e}}_i, \tag{9.5}$$

for each component $i = 1, 2$ where $\mathbf{u}_j^{(n+1)*}$ is $\mathbf{u}$ evaluated for the homogeneous system as before at the jth node and $(n+1)th$ time step.

The values of β for the PW Model are found to be

$$\beta_1 = \frac{\tilde{\rho}\,(V(\tilde{\rho}) - \tilde{v})}{2C_o\tau}, \quad \beta_2 = -\frac{\tilde{\rho}\,(V(\tilde{\rho}) - \tilde{v})}{2C_o\tau}. \tag{9.6}$$

Similarly, for the BMW model, β are found to be

$$\beta_1 = \frac{\tilde{\rho}\,(V(\tilde{\rho}) - \tilde{v})}{\sqrt{-2\tau V'(\rho)}}, \quad \beta_2 = -\frac{-\tilde{\rho}\,(V(\tilde{\rho}) - \tilde{v})}{\sqrt{-2\tau V'(\rho)}}. \tag{9.7}$$

Again, using the same method the values of β for the AR Model are found to be

$$\beta_1 = \frac{\tilde{\rho}\,(V(\tilde{\rho}) - \tilde{v})}{\gamma\tilde{P}\tau}, \quad \beta_2 = -\frac{\tilde{\rho}\,(V(\tilde{\rho}) - \tilde{v})}{\gamma\tilde{P}\tau}. \tag{9.8}$$

And finally for Zhang, the values of β are found to be

$$\beta_1 = \frac{\tilde{w}}{\widetilde{\rho V'(\rho)}\tau}, \quad \beta_2 = -\frac{\tilde{w}}{\widetilde{\rho V'(\rho)}\tau}. \tag{9.9}$$

9.3 Boundaries

The question also arises as to how to implement the addition of the relaxation term at the boundaries (except for the BMW model-see Section 7.4.1). For the homogeneous system we have determined the strengths and origins of the two Characteristic Variables r and s with cell average wavespeeds. With the addition of the source term however these variables still move with speed given by the eigenvalues λ_i but are no longer constant along the characteristics. This is due to the equation now being

$$\frac{\partial r}{\partial t} + \lambda_1 \frac{\partial r}{\partial x} = \{X^{-1}R\}_1, \tag{9.10}$$

where $\{X^{-1}R\}_i$ is the ith element of $X^{-1}R$. This equation is rewritten using the chain rule as

$$\frac{dr}{dt} + \frac{\partial r}{\partial x}\left(\lambda_1 - \frac{dx}{dt}\right) = \{X^{-1}R\}_1, \tag{9.11}$$

where X is the matrix of eigenvectors (see (7.47, 7.50, 7.60, 7.65)), and R is the vector of source terms (9.2). Therefore along the characteristic given by $\frac{dx}{dt} = \lambda_1$, now $\frac{dr}{dt} = \{X^{-1}R\}_1$, i.e. r is no longer contant along the characteristic.

To approximate the change in r along the characteristic in a time step Δt we use a forward difference. r^{n+1} is therefore given by

$$r^{n+1} = r^n + \Delta t\{X^{-1}R\}_1. \tag{9.12}$$

Similarly for the second characteristic variable s. Along the characteristic given by $\frac{dx}{dt} = \lambda_2$, now $\frac{ds}{dt} = \{X^{-1}R\}_2$, i.e. s is also no longer contant. The change in s is therefore given by

$$s^{n+1} = s^n + \Delta t\{X^{-1}R\}_2, \tag{9.13}$$

where $X^{-1}R$ is evaluated using Roe averages (or alternative averages) for the cell.

The boundary cell wavespeeds (using the average from the real boundary node and the adjacent internal node) determine the origins of r and s as previously. The changes in r and s are then calculated from (9.12) and (9.13). These new characteristic

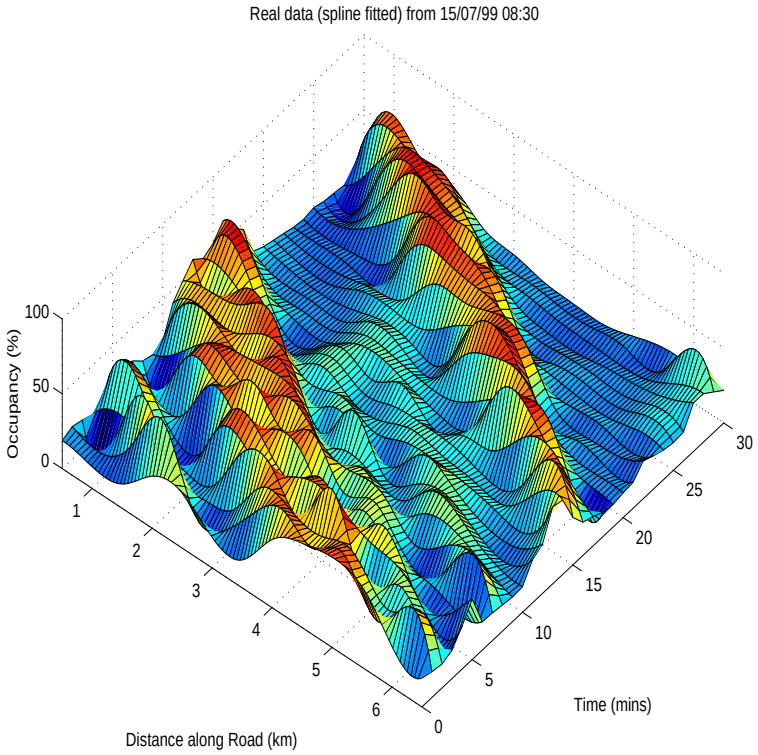

Figure 9.1: 3D plot of occupancy for a period of 30 mins from 08:30 15/07/99 from the real data.

variables are then recombined to determine $\mathbf{u}^{n+1}$ at the boundary node as required (see Chapter 7.3).

The right hand sides of the characteristic variable equations (9.12, and 9.13) are found to be

$$X^{-1}R = \begin{pmatrix} \frac{\tilde{\rho}(V(\tilde{\rho})-\tilde{v})}{2C_o\tau} \\ -\frac{\tilde{\rho}(V(\tilde{\rho})-\tilde{v})}{2C_o\tau} \end{pmatrix}, \tag{9.14}$$

$$X^{-1}R = \begin{pmatrix} \frac{\tilde{\rho}(V(\tilde{\rho})-\tilde{v})}{\gamma\tilde{P}\tau} \\ -\frac{\tilde{\rho}(V(\tilde{\rho})-\tilde{v})}{\gamma\tilde{P}\tau} \end{pmatrix}, \tag{9.15}$$

$$X^{-1}R = \begin{pmatrix} -\frac{(V(\tilde{\rho})-\tilde{v})}{V'(\tilde{\rho})\tau} \\ \frac{(V(\tilde{\rho})-\tilde{v})}{V'(\tilde{\rho})\tau} \end{pmatrix}, \tag{9.16}$$

for the PW, AR and Zhang models respectively.

9.3.1 Comparison of Models with Relaxation

Figure 9.1 is a plot of the real occupancy data from 08:30 15/07/99 for 30 mins. The features we would like to capture are the backward moving high density peaks,

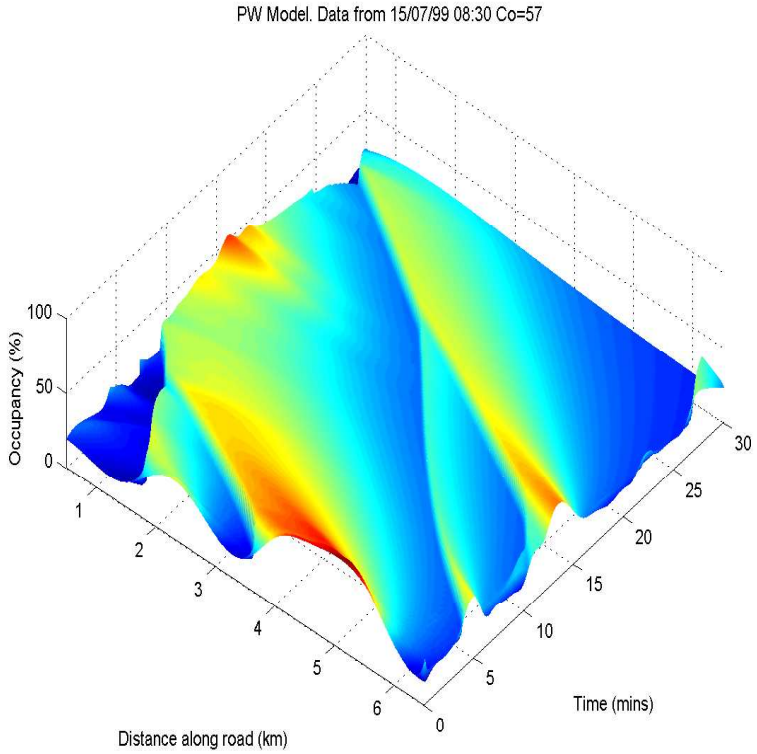

Figure 9.2: 3D plot of occupancy for a period of 30 mins from 08:30 15/07/99. PW model with $\tau = 32$ seconds.

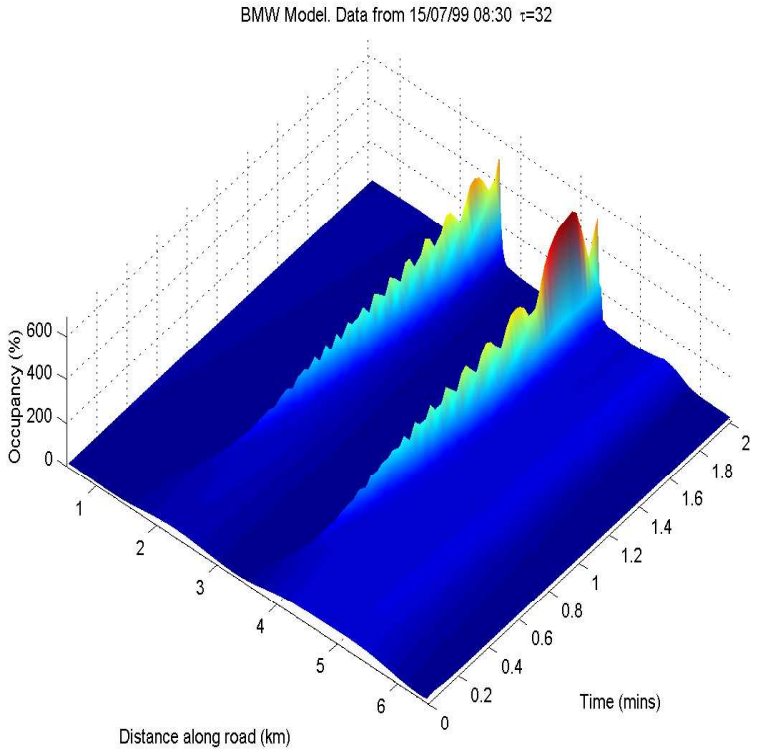

Figure 9.3: 3D plot of occupancy for a period of 2 mins from 08:30 15/07/99. BMW model with $\tau = 32$ seconds.

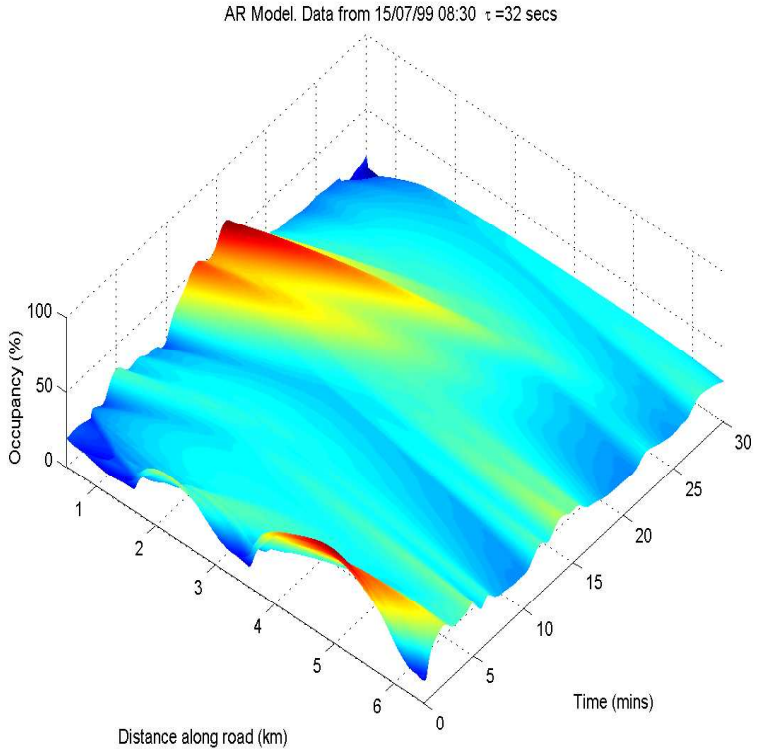

Figure 9.4: 3D plot of occupancy for a period of 30 mins from 08:30 15/07/99. AR model with $\tau = 32$ seconds.

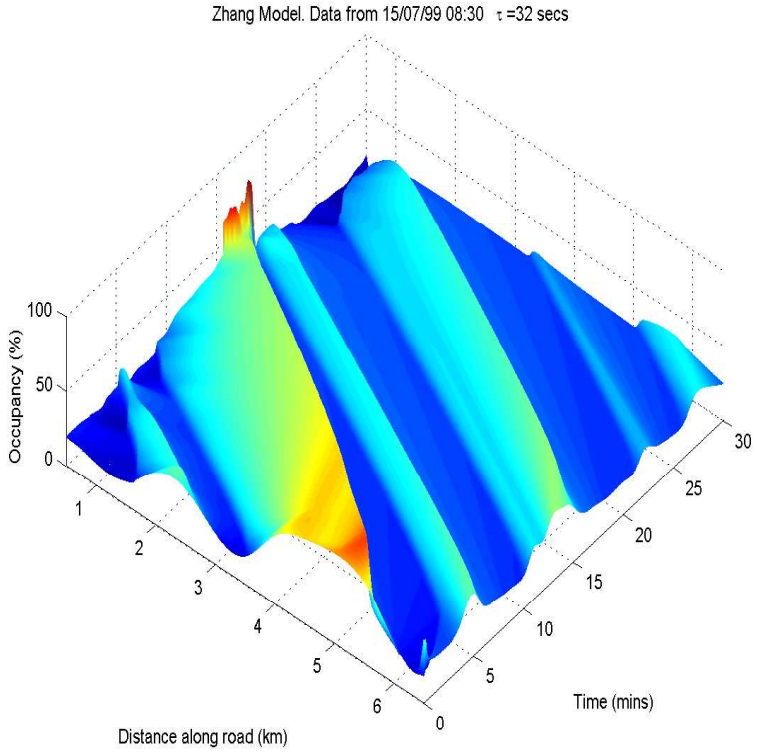

Figure 9.5: 3D plot of occupancy for a period of 30 mins from 08:30 15/07/99. Zhang model with $\tau = 32$ seconds.

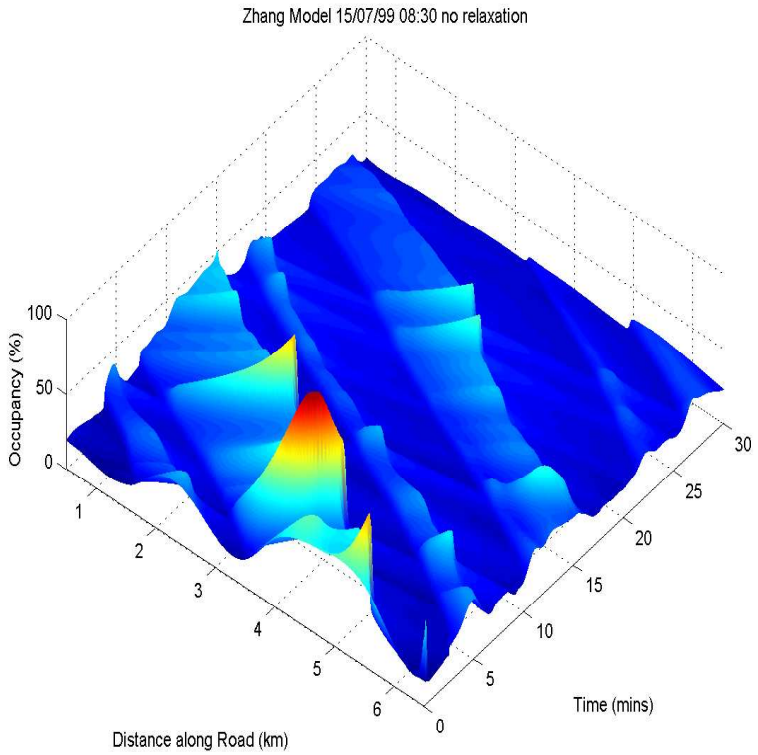

Figure 9.6: 3D plot of occupancy for a period of 30 mins from 08:30 15/07/99. Zhang model with no relaxation term ($\tau \to \infty$)

the forward moving low density troughs and the interactions between the two. For example in the high density backward moving waves they are not a solid block as they move backwards, but frequently they dip briefly before resuming at a similar height and speed. Without relaxation, as discussed in Chapter 8, the Zhang models captures most of the desired features most accurately.

Figure 9.2 is a plot of the PW model with relaxation, where τ is 32 seconds. the effect of adding the relaxation term is it appears to smooth out the features. Particularly with the later high density waves (e.g. ones that start at the right hand side, $x = 6.5$, after time=20 seconds) the speeds and hence positions of the waves seem to be improved and die away as in the real data.

Figure 9.3 is a plot of the BMW model with $\tau = 32$ seconds. The results obtained are unstable and peaks form that grow to values way above the maximal density of 100%. These peaks are not removed by refining the grid. This demonstrates that for the BMW model $\tau = 32$ is a completely unrealistic value. It is not surprising that increasing τ to this value in this model has such a dramatic effect as τ also appears in

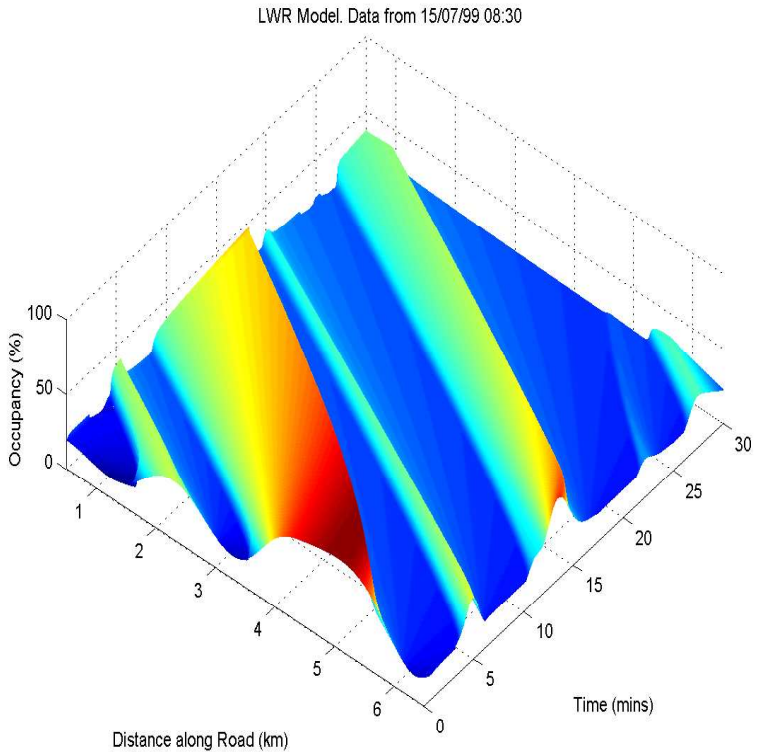

Figure 9.7: 3D plot of occupancy for a period of 30 mins from 08:30 15/07/99. LWR model.

the flux function. In Section 8 we saw that $\tau \approx 1.4$ gave the best results for the wave speeds. We will see later what effect adding relaxation has for $\tau = 1.4$ (Figure 9.9).

Figure 9.4 is an equivalent plot for the AR model, again with $\tau = 32$ seconds. The smoothing effects of adding the relaxation term are also observed, but the waves observed using the AR model are significantly different from those observed in the real data, hence adding the relaxation term alone with $\tau = 32$ is not a sufficient addition to give satisfactory results.

The Zhang model with no relaxation displays desirable features as discussed above such as the high density peaks that dip frequently due to the interactions between peaks and troughs, Figure 9.6. By adding the relaxation term these interactions appear to have been smoothed out completely, Figure 9.5. One positive effect is the removal of the greater than maximal density values reached at times in some of the larger peaks without relaxation. This does not outweigh the undesirable effects of removing the peaks completely however. Relaxation therefore appears to be an undesirable term to add to models if you want to capture this feature. (In any case V appears in the flux term for this model).

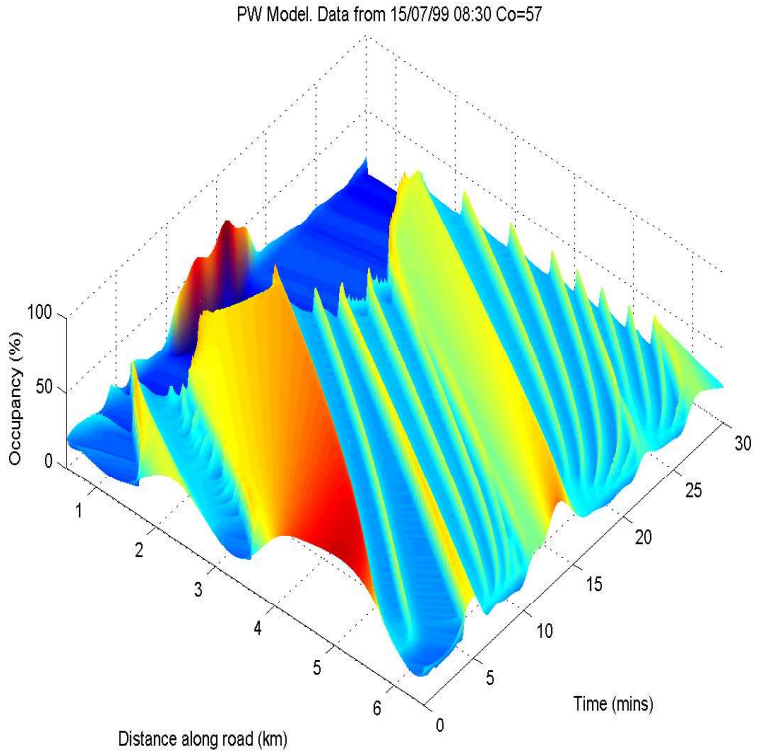

Figure 9.8: 3D plot of occupancy for a period of 30 mins from 08:30 15/07/99. PW model with $\tau = 1.4$ seconds.

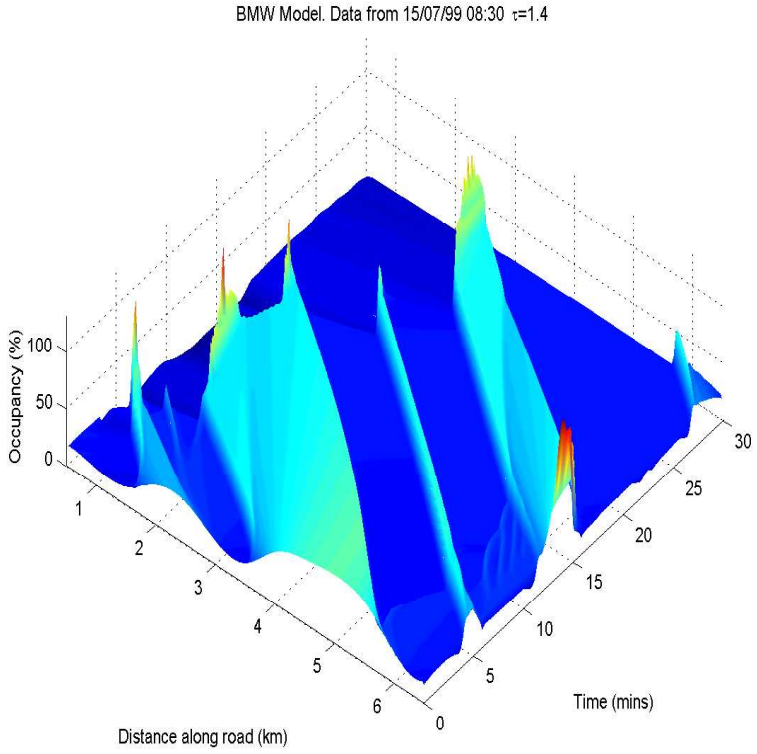

Figure 9.9: 3D plot of occupancy for a period of 30 mins from 08:30 15/07/99. Berg model with $\tau = 1.4$ seconds.

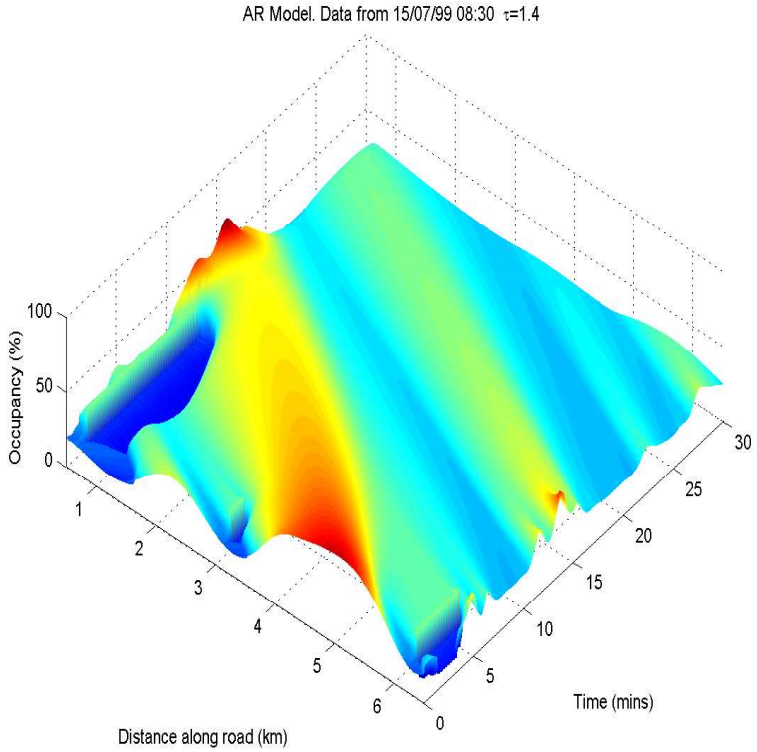

Figure 9.10: 3D plot of occupancy for a period of 30 mins from 08:30 15/07/99. AR model with $\tau = 1.4$ seconds.

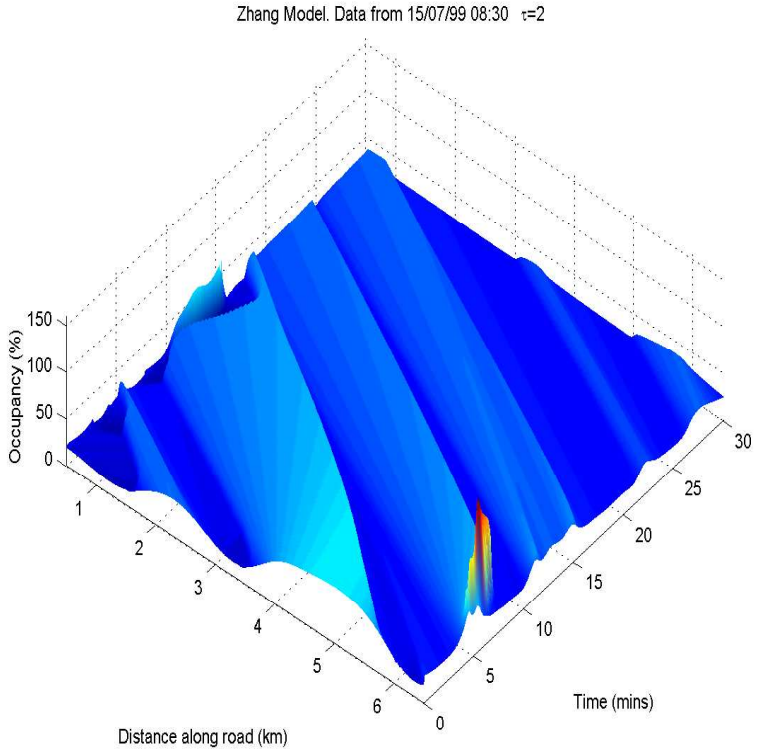

Figure 9.11: 3D plot of occupancy for a period of 30 mins from 08:30 15/07/99. Zhang model with $\tau = 2$ seconds.

Aw and Rascle, [1] suggested that by lowering the τ the relaxation term would dominate the system in their model. This argument could be applied to each of the models. By doing this the results from each model would become more and more alike until τ is sufficiently small that the results tend towards those obtained from the LWR model. This is reasoned as the limit as $\tau \to 0$, $v = V(\rho)$ which can then be substituted into the conservation equation, thereby reducing the system to the LWR model. Figure 9.7 is the equivalent LWR model plot for comparison with the other models to test this theory.

Figure 9.8 is the PW model plot with $\tau = 1.4$. The waves do indeed appear to be more like the LWR model as predicted. However there are also peaks that have spontaneously appeared in the lower density regions. These are not present in the real data. The reason for their appearance has not been investigated here, but they resemble the spontaneous jams discussed by Kerner and Konhäuser [16].

For the BMW model using the value of $\tau = 1.4$ that previously gave the best wave speeds, by now adding relaxation as with the Zhang model for $\tau = 32$, all desirable features of peaks interacting with troughs are completely smoothed out. There also appears to be large *spikes* at the boundaries when peaks are entering and leaving the region. This could be due to the crude method of using ghost cells of fixed boundary data, but should be investigated further.

When $\tau = 1.4$ in the AR model the waves now have completely changed direction and are moving with speeds comparable to the LWR model as expected, Figure 9.10.

Finally the Zhang model, as expected, resembles the LWR model with much smoothing of features, Figure 9.11. Here however $\tau = 2$ as adding this term seems to make the model unstable for lower values of τ. Again, refining the grid does not eliminate this problem, hence it is a feature of the model. The reason for the appearance of a spike at the right hand boundary is unknown at this time. The question arises if adding relaxation to the Zhang model is a suitable step at all since the model is derived from forming the wavespeeds using the optimal velocity finction $V(\rho)$ in the first place. The model certainly produces better results without relaxation.

9.4 Viscosity

In this section we look at the effects of adding viscosity terms, in this case second derivatives of velocity or density. These are also source terms that appear on the right hand side of the equations. They generally have the effect of smoothing out discontinuities and extreme values. Berg et al [3] claim the diffusion terms are crucial in correctly predicting the flow.

Figure 9.12 is an example of the smoothing effect of adding the viscosity term μv_{xx} to the Zhang model, where μ is taken to be 27 (the effects of smaller values were not clearly visible). The viscosity was applied by discretising the second derivative term v_{xx} using a central difference then adding

$$\mu \frac{\Delta t}{\Delta x^2}(v_{j+1} - 2v_j + v_{j-1})$$

to the second conserved variable at each node. As expected the addition of the second derivative term smooths out sharp changes in density. The full plots for each model have been omitted as they produce similar results, but with smoothing effects. Even with the BMW model, the difference observed when adding all the terms suggested by their model (5.17), merely produces a smoothing effect. This is however beneficial as the peaks observed that were greater than the maximal bumper to bumper density were eliminated! For this reason adding viscosity source terms to BMW, and indeed Zhang are advantageous. The viscosity terms for BMW are

$$\frac{V'(\rho)}{\tau}\left(\frac{\rho_{xx}}{6\rho} - \frac{(\rho_x)^2}{2\rho^2}\right),$$

and were applied by adding

$$\frac{V'(\rho_j)\Delta t}{\tau \Delta x^2}\left(\frac{\rho_{j+1} - 2\rho_j + \rho_{j-1}}{6\rho_j} - \frac{(\rho_{j+1} - \rho_j)(\rho_j - \rho_{j-1})}{2\rho_j^2}\right),$$

to each node.

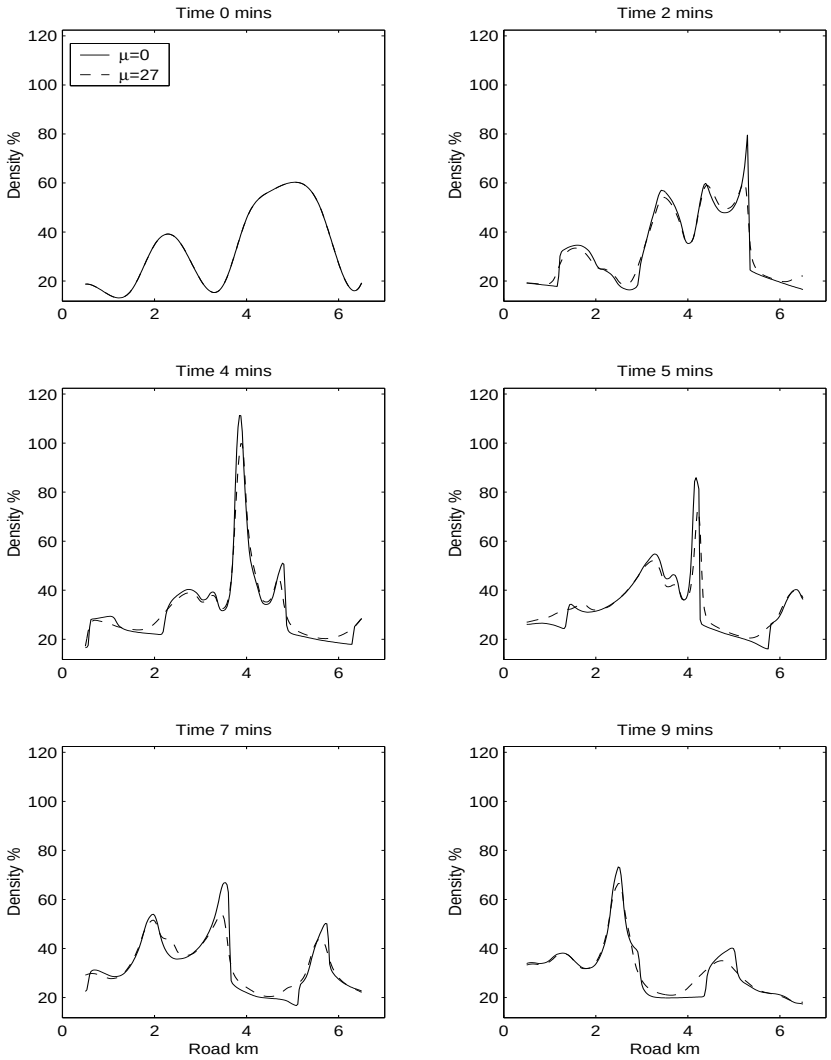

Figure 9.12: Comparison of Zhang model with and without viscosity. Data from 15/07/99 08:30 over a period of 10 minutes and $\mu = 27$.

Chapter 10

Conclusions

First we summarise the main points of the thesis. We have averaged the real data from a stretch of the M25 motorway and fitted a suitable flux function to the fundamental diagram. This flux function was then used with the LWR model and analytic solutions found to two test cases. Due to the non-convex nature of the flux function the development of the simple initial conditions gave several complicated features such as discontinuities splitting into combinations of shocks and fans. Four numerical schemes were described and compared against the exact solutions and the best one selected. This was the second order scheme with flux limiter, where a sonic entropy fix was required to ensure the correct expansion of fans.

Next we considered systems of equations. We described numerical schemes, concentrating on the construction and implementation of a Roe decomposition for each model and then applying the second order scheme with a flux limiter. Again a sonic entropy fix was required. The treatment of boundaries was described in detail in order to ensure the correct movement of waves into and out of the domain. This was implemented using Characteristic Variables for the PW, AR and Zhang models but an alternative approach was suggested for BMW due to the complicated nature of its Characteristic Variables.

We tested all five models against two different sets of real data to see how realistic they are. For the LWR model the best choice of flux function was f_5, which was also the best fit to the fundamental diagram. LWR was able to model individual types of waves with reasonable accuracy but, not surprisingly, failed to model the flow when

waves interacted and gave very smooth results, unlike the real data.

Solutions of systems of two equations consist of superimposing two waves and so are able to model waves interactions. In the PW model, although it was able to capture the speed of the waves successfully in the first simulation, the definition of the waves and interactions were poor. It also allowed negative velocities of the traffic. The AR model was least able to predict the flow. The two best two-equation models were BMW and Zhang. They both had better definition of the high density ridges but Zhang allowed densities greater than the maximum bumper to bumper density. Both models didn't capture the correct balance of interactions between the waves. In the first simulation Zhang allowed too much interaction between the peaks and troughs whereas BMW didn't always allow enough interaction. In the second simulation BMW allowed too much deterioration of the high density ridges and Zhang, although didn't allow as much deterioration, did predict lower densities for the slow backward moving waves. LWR, although produced very smooth results, was still comparable at predicting wave speeds to BMW and Zhang.

The addition of a relaxation term removed desirable features of the high density ridges, whereas viscosity terms improved the Zhang model by smoothing out the higher unphysical densities.

In summary, LWR is a robust model with a suitable choice of flux function. To capture the complex interactions between different types of waves observed in reality however, a system is required. From the simulations presented here AR was least able to capture the movement of the waves, PW gave the correct directions and speeds at times but Zhang with a relaxation term produced the best results with BMW a close second, although there is room for improvement.

As a possible extension to this work, the addition of source terms to include on/off ramps might be considered to make the models more applicable to real situations.

There is also the issue that we are using data from a multilane carriageway and averaging. There is a justification for this in that we take the mean density and fluxes over the lanes and the transfer functions between adjacent lanes cancel out. This doesn't however take into account the changes in drivers' behaviour before and after

changing lanes. Neither do the models account for changes in behaviour entering and leaving the carriageway and there isn't a stretch of road sufficiently long enough that these effects are completely removed in the simulations. The best models seem to have been derived from microscopic principles, so perhaps a set of rules to describe changes in behaviour in a multilane situation and approaching junctions could be investigated.

Bibliography

[1] A.Aw and M.Rascle. *Resurrection of 'second order' models of traffic flow?* SIAM J. Appl. Math., 60, pp 916-938 (2000).

[2] M.Bando et al. *Dynamical model of traffic congestion and numerical simulation.* Phy Rev E, 51, pp 1035-1042 (1995).

[3] P.Berg, A.Mason and A.Woods. *Continuum approach to car-following models.* Phys Rev E, 61, pp 1056-1066 (2000).

[4] R.E.Chandler, R.Herman and E.W.Montroll. *Traffic dynamics; studies in car following.* Operations Research, 6, pp 165-184 (1958).

[5] C.Daganzo. *Requiem for second-order fluid approximations of traffic flow.* Transpn. Res.-B 29B, pp 277-286 (1995).

[6] C.M.Dafermos. *Polygonal approximations of solutions of the initial-value problem for a conservation law.* J. Math. Anal. Appl., 38, pp 33-41 (1972).

[7] H.T.Fritsche. *A model for traffic simulation.* Traffic Engineering and Control, 35 vol. 5, pp 317-321 (1994).

[8] P.Glaister. *Difference Schemes For The Shallow Water Equations.* Numerical Analysis Report 9/87, Dept. of Mathematics, University of Reading (1987).

[9] J.M.Greenberg. *Extensions and Amplifications of a Traffic Model of Aw and Rascle.* SIAM J. Appl. Math., 62, pp 729-745 (2001).

[10] R.Haberman. *Mathematical Models. Mechanical Vibrations, Population Dynamics, and Traffic Flow.* SIAM (1998) A republication of the work first published by Prentice-Hall, Inc., Engelwood Cliffs, New Jersey (1977).

[11] A.Harten, P.D.Lax and B.van Leer. *On upstream diffrenecing and Godunov-type schemes for hyperbolic conservation laws.* SIAM Review, 25, pp35-61, (1983).

[12] D.Helbing. *Improved fluid-dynamic model for vehicular traffic.* Phys Rev E, 51, pp 3164-3169 (1995).

[13] D.Helbing. *Gas-kinetic derivation of Navier-Stokes-like traffic equations.* Phys Rev E, 53, pp 2366-2381 (1996).

[14] D.Helbing and M.Treiber. *Numerical Simulation of Macroscopic Traffic Equations.* Computing in Science and Engineering, 1, pp89-99 (1999)

[15] E.N.Holland. *A Generalised Stability Criterion for Motorway Traffic.* Tranpn. Res. -B 32B, pp 141-154 (1998).

[16] B.S.Kerner and P.Konhäuser. *Cluster effects in initially homogeneous traffic flow.* Phys Rev E, 48, pp R2335-R2338 (1993).

[17] B.S.Kerner and P.Konhäuser. *Structure and parameters of clusters in traffic flow.* Phys Rev E, 50, pp 54-83 (1994).

[18] B.S.Kerner, P.Konhäuser, and M.Schilke. *Deterministic spontaneous appearance of traffic jams in slightly inhomogeneous traffic flow.* Phys Rev E, 51, pp 6243-6246 (1995).

[19] J.Krug and H.Spohn. *Universality classes for deterministic surface growth.* Phys. Rev. A, 38, pp 4271-4283 (1988).

[20] R.D.Kühne. *Freeway Control Using a Dynamic Traffic Flow Model and Vehicle Reidentification Techniques.* Transpn. Res. Rec., 1320, pp 251-259 (1991).

[21] R.J.LeVeque. *Numerical Methods for Conservation Laws.* Birkhäuser (1992).

[22] R.J.LeVeque. *Some Traffic Flow Models Illustrating Interesting Hyperbolic Behavior.* Notes prepared for a minisymposium on traffic flow at the SIAM Annual Meeting, July 10, 2001.

[23] M.J.Lighthill and G.B.Whitham. *On kinematic waves. I:Flow movement in long rivers. II:A Theory of traffic flow on long crowded roads.* Proc. Royal Soc., A229, pp 281-345 (1955).

[24] K.Nagel and M.Paczuski. *Emergent Traffic Jams.* Phys. Rev. E, 51, pp 2909-2918 (1995).

[25] K.Nagel. *Particle hopping models and traffic flow theory.* Phys Rev E, 53, pp 4655-4672 (1996).

[26] G.F.Newell. *Nonlinear effects in the dynamics of car following.* Operations Research, 9, pp 209-229 (1961).

[27] H.J.Payne. *Models of freeway traffic and control.* Math.Models Publ. Sys.Simul. Council Proc.,28, pp 51-61 (1971).

[28] I.Prigogine and R.Herman. *Kinetic Theory of Vehicular Traffic.* Elsevier, New York, (1971).

[29] P.I.Richards. *Shockwaves on the highway.* Operations Research, 4, pp 42-51 (1956).

[30] P.L.Roe *Approximate Riemann Solvers, parameter vectors, and difference schemes.* Journal of Computational Physics vol.43 pp 357-372, (1981).

[31] P.L.Roe *Upwind Differencing Schemes, Hyperbolic Conservation Laws With Source Terms.* Proc. 1st Int. Congress on Hyperbolic Problems, St. Etienne (eds. C.Carassa and D.Serre 1986).

[32] G.Strang *Introduction to Applied Mathematics.* Wellesley Cambridge Press, (1986).

[33] P.K.Sweby. *Shock Capturing Schemes.* PhD Thesis, University of Reading (1982).

[34] P.K.Sweby. *High Resolution Schemes Using Flux Limiters For Hyperbolic Conservation Laws.* SIAM J. Numer. Anal. 21, pp 995-1011 (1984).

[35] P.K.Sweby. *Private communication.* (2002).

[36] G.B.Whitham. *Linear and Nonlinear Waves.* John Wiley, New York, (1974).

[37] R.E.Wilson and P.Berg. *Existence and Classification of Travelling Wave Solutions to Second Order Highway Traffic Models.* Traffic and Granular Flow. Awaiting publication.

[38] H.M.Zhang. *A theory of non-equilibrium traffic flow.* Transpn. Res.-B 32B, pp485-498, (1998).

[39] H.M.Zhang. *Driver memory, traffic viscosity and a general viscous traffic model.* ITS Working Paper. University of California at Davis (2000).

[40] H.M.Zhang. *A non-equilibrium traffic model deviod of gas-like behaviour.* Transpn. Res.-B 36B, pp275-290, (2002).